A NOVEL POSTBUCKLING-BASED MECHANICAL ENERGY TRANSDUCER AND ITS APPLICATIONS FOR STRUCTURAL HEALTH MONITORING

By

Pengcheng Jiao

A DISSERTATION

Submitted to
Michigan State University
in partial fulfillment of the requirements
for the degree of

Civil Engineering – Doctor of Philosophy

2017

ABSTRACT

A NOVEL POSTBUCKLING-BASED MECHANICAL ENERGY TRANSDUCER AND ITS APPLICATIONS FOR STRUCTURAL HEALTH MONITORING

By

Pengcheng Jiao

In recent years, significant research efforts have been dedicated to developing self-powered wireless sensors without the limit of battery lifetime, such that they can be used to continuously monitor critical limit states and detect structural potential failures for structural health monitoring (SHM). As one of the most promising techniques, vibration-based energy harvester using piezoelectric transducer has been extensively used, given the advantages in size limitation and flexibility of embedding beneath construction surfaces. However, the low frequency of civil infrastructures' fundamental vibration modes (< 5 Hz) severely impedes the application of the energy harvester, since piezoelectric transducer only exhibits optimal outputs under a narrow range of natural frequency inputs (50-300 Hz).

Recently, a mechanism has been developed to harvest energy at very low frequencies (< 1 Hz) using mechanical energy concentrators and triggers. This technique is based on the snap-through between different buckling mode transitions of a bilaterally constrained beam subjected to quasi-static axial loads. Attaching piezoelectric transducer to the buckled beam, electrical power can be generated by converting the quasi-static excitations into localized dynamic motions. The proposed mechanism can be implemented as an indicator for critical limit states, given the electrical power indicates the corresponding strain/deformation that a structure undergoes. However, the efficiency of the mechanism significantly depends on the post-buckling behavior of the deflected beam element. Inadequate controlling over the system's mechanical response critically impedes the application of the mechanism. Therefore, it is of research and

practice interests to effectively control the mechanical response such that to maximize the electrical power and control the electrical signal.

This study presents a technique for energy harvesting and damage sensing under quasi-static excitations. In order to optimize the harvesting efficiency and sensing accuracy of the proposed technique, which cannot be achieved by using uniform cross-section beams, non-prismatic beams are theoretically and experimentally studied. The mechanical response of the structural instability-induced systems are efficiently predicted and controlled. In particular, a theoretical model is developed using small deformation assumptions. Non-uniform beams are investigated with respect to the effects of beam shape configuration and geometry property. Piezoelectric scavengers with different natural frequencies are then used to convert the high-rate motions of the deflected beams at buckling transitions into electrical power. In addition, a large deformation model is developed to capture the buckling snap-through of the bilaterally constrained systems under large deformation assumptions. The model investigates the static and dynamic instabilities of bilaterally constrained beams subjected to gradually increasing loads. The model takes into account the impact of constraints gap under different constraint scenarios.

ACKNOWLEDGEMENTS

I would like to express my deepest gratitude to my advisor, Dr. Nizar Lajnef, for his excellent guidance, invaluable knowledge, and precious advices. Without his support, assistance and patience this work would have been impossible.

I must extend my sincere appreciation to the rest of my committee members, Dr. Venkatesh Kodur, Dr. Weiyi Lu, and Dr. Sara Roccabianca, for the time, consideration and evaluation put on this work.

My special appreciation should go to Dr. Wassim Borchani, a postdoctoral research associate, for his friendship, support and encouragement. I am thankful and indebted to him for providing insight and expertise that greatly assisted me in accomplishing this work, especially during the last two years of my Ph.D. study. I also need to show my gratitude to my Ph.D. fellows in EB1528, Hassen Hasni and Dr. Amir H. Alavi, for sharing valuable advice and guidance with me. The former M.S. students in EB1528, Adam Al-Ansari, Fei Teng, and Moses Pacheco, are also appreciated.

I would also like to thank the instructors of CE221 Statics, Dr. Gilbert Baladi, Dr. Roozbeh Dargazany, and Dr. Mohammad Haq, and the current and previous graduate teaching assistants, Hadi Salehi, Leila Khalili, Puneet Kumar, Dr. Nan Hu, Ankit Agarwal, Dr. Pegah Rajaei, etc., for their guidance, help and cooperation when I was a teaching assistant in the class.

The friends I met during the long PhD journey at Michigan State University, Hulong Zeng, Xiaorui Wang, Sepehr Soleimani, Ali Imani Azad, etc., are greatly thankful. I would like to thank Laura Post, Margaret Connor, Laura Taylor, and Bailey Weber as well, for their help in the matter of processing paperwork.

Finally, I must express my very profound gratitude to my parents, Hongqi Jiao and Ying Zhang, as well as my uncle, Ming Zhang, for their understanding, continuous love and unfailing support throughout my years of study in the U.S. This accomplishment would not have been possible without them.

TABLE OF CONTENTS

LIST OF TABLES

LIST OF FIGURES

CHAPTER 1

INTRODUCTION

1.1. Motivation and Vision

In recent years, significant research efforts have been dedicated to developing and applying smart mechanisms and techniques to monitor critical limit states and detect structural potential failures. Different types of wireless sensors have been developed to particularly monitor the critical events that structures in civil infrastructures might be subjected, e.g., displacement, pressure, temperature, vibration, etc. In order to effectively detect structural health status, different types of monitoring systems have been particularly conducted to monitor the changes of structure response. However, those monitoring systems require a reliable, continuous source of power to charge the wireless sensors, rather than using traditional batteries due to their limited lifetimes. Since huge amounts of wireless sensors that monitoring systems are typically implemented, it is of great research and practice interests to develop a type of self-powered wireless sensor without the power limit.

To develop self-powered wireless sensors, many energy harvesting mechanisms have been proposed based on different potential sources of energies, e.g., radio frequency, solar, strain, thermal gradient, vibration energy, etc. Vibration-based energy harvesters using piezoelectric transducers are one of the most promising techniques, given the advantages in size limitation and the possibility of embedding beneath construction surfaces. Even though vibration-based harvesters using piezoelectric materials have been extensively implemented due to the relatively high energy conversion efficiency and mechanical-to-electrical coupling properties, the technique only exhibits optimal outputs under a narrow range of natural frequency inputs. A vibration-based scavenger, for example, with an overall volume limited to $< 5\ \text{cm}^3$ will exhibit a resonant frequency in the range 50-300 Hz (Najafi et al. 2011). In the contrast, civil structures typically have fundamental vibration modes at frequencies < 5 Hz, e.g., the daily temperature- or pressure variation-induced stress/strain response (< 1 mHz). Therefore, it is of significance to effectively increase, or convert, the quasi-static motions to high frequency vibrations, such that piezoelectric-based energy harvesters can be triggered. Many techniques have been proposed to harvest energy from extreme low frequency response, e.g., improvement of piezoelectric materials, optimal design of electrode patterns and system configuration, utility of matching networks, controlling of resonant frequency, etc. However, energy harvesting based on the inputs, e.g., load, deformation or motion, within quasi-static frequency range is still elusive, since the up-to-date energy harvesters are still inefficient and not suitable for low frequency vibration sources (Green et al. 2013).

Recently, a technique has been developed to harvest energy at very low frequencies (< 1 Hz) using mechanical energy concentrators and triggers (Borchani et al., 2015). This mechanical system is based on the snap-through between different buckling mode transitions of a bilaterally constrained beam subjected to axial loads. As the axial loads are increased, the strain energy stored in the buckled element is released as kinetic energy mode transitions. Relying on the high-rate motions generated from the post-buckling response, the system is effectively activated under quasi-static strain/deformation. The snap-through behavior of bilaterally constrained beams is used to transform low-frequency and low-rate excitations into high-rate motions. Using a piezoelectric transducer, these motions are converted into electrical power. Post-buckling response of elastic beams has been widely used in many systems to develop efficient energy harvesting and damage sensing mechanisms under quasi-static excitations (Lajnef et al. 2014; Borchani, et al. 2015; 2016; 2017).

However, the efficiency of the energy harvester significantly depends on the post-buckling behavior of the deflected beam element. Inadequate controlling over the beam's mechanical response critically impedes the application of the mechanism and, hence, it is of research and practice interests to effectively control the post-buckling response, i.e., buckling mode transitions, such that to improve the energy conversion efficiency and maximize the generated electrical power. In this study, the challenging prospect is to design a mechanism such that wireless sensors can be self-powered by directly harvesting energy from the quasi-static response of civil infrastructures.

1.2. Literature Review

One of the most severe challenges of deploying Structural Health Monitoring (SHM) systems in civil infrastructures is the limited lifespan of batteries that are typically used to power the monitoring sensors. This issue is particularly significant due to the enormous number of sensors that are required in SHM (Lynch and Loh, 2008). In order to overcome the power limitation, a new self-powered sensor, whose concept is presented in Figure 1-1, has been developed (Lajnef et al., 2012; 2014). This sensor has accomplished competitive performance in different applications of SHM and damage detection (Alavi et al., 2015; 2016; 2017). The sensor is composed of two parts, namely, power harvesting unit and sensing unit. The energy harvesting unit is of great importance as it provides the required electric power to the wireless sensor without the limitation of battery lifetime or wiring harness (Lajenf et al., 2015; Rafiee et al., 2015; Erturk and Inman, 2008). In addition, the electric signal from the harvester can be controlled to correspond to a specific strain/deformation. Therefore, the primary objectives of the energy harvesting device in this study are: 1) transforming strain energy into electric energy to power wireless sensors; and 2) presenting a potential solution to sense damage based on the electric signals generated by the device. This work aims to control the strain that triggers the energy harvesting cell's electric signal to accurately sense damage and optimize the output energy to efficiently power wireless sensors. Thanks to its mechanical-to-electrical energy conversion capability and its possibility to be embedded within construction materials, piezoelectric materials can be used as the energy-harvester oscillator in the energy harvesting cell presented in the figure (Blarigan et al., 2015; Cook-Chennault et al., 2008; Green et al., 2013; Harne and Wang, 2013). Yet vibration-based piezoelectric harvesters deliver optimal performance only when excited near their resonance frequency. In order to widen the input requirement and extend the application range, many research efforts have been conducted to enlarge the operating bandwidth of vibration-based piezoelectric generators (Dong et al., 2015; Hajati and Kim, 2011; Marinkovic and Koser, 2009; Tang et al., 2010; Najafi et al., 2011; Quinn et al., 2011; Yang et al., 2016). However, these approaches are still inefficient for low frequency applications, particularly within the quasi-static domain (< 1 Hz).

On the other hand, buckling and post-buckling elastic instabilities have been extensively studied with multiple functional purposes (Chen et al., 2013; Chen et al., 2011; Jiao et al., 2012; Safa and Hocker, 2015; Hu and Burgueno, 2015). In a number of applications, including actuation, sensing, and energy harvesting, buckled elements have shown great efficiency in developing monostable, bistable and multi-stable mechanisms (Lajnef et al., 2014; Lajnef et al., 2015; Aladwani et al., 2015; Park et al., 2008; Zhao et al., 2008). Recently, the post-buckling instabilities of axially-loaded bilaterally-constrained beams have been exploited to develop mechanical triggering mechanisms (Lajnef et al., 2012; 2014). These mechanisms release the strain energy stored in the loaded beams through snap-through buckling-mode-transitions. The slender beam in the energy harvesting cell buckles into different buckling modes depending on the levels of excitations, as shown in Figure 1-1.The transitions between the buckling configurations are accompanied by a sudden release of a part of the strain energy stored in the deformed beam (Lajnef et al., 2014). The snap-through buckling transitions of the beam transform the global low frequency excitations into localized high acceleration motions that are captured by the piezoelectric transducer. Hence the kinetic energy is converted into electric power. The energy conversion mechanism has been integrated with Piezo-Floating-Gate sensors to allow for self-powered sensing and logging of quasi-static events (Lajenf et al., 2015). When the capacitor voltage meets a preset threshold, the converted electric power is transferred to the objective wireless sensors. Through the process, part of the converted energy is used to bias the electronic circuit. Electric power generation occurs by exciting the power harvesters during snap-through transitions. To maximize the levels of the harvested energy, the snap-through locations (i.e. points along the beam travelling the largest distance during transitions) have to coincide with the base of the harvester. Also the snap-through events and the spacing between them have to be controlled such that they can be related to specific axial strains or deformations. When the system is subjected to such displacement or strain, the snap-through of the beam is triggered generating, then, an electric signal that can be used to sense the change in the structural response due to potential damage.

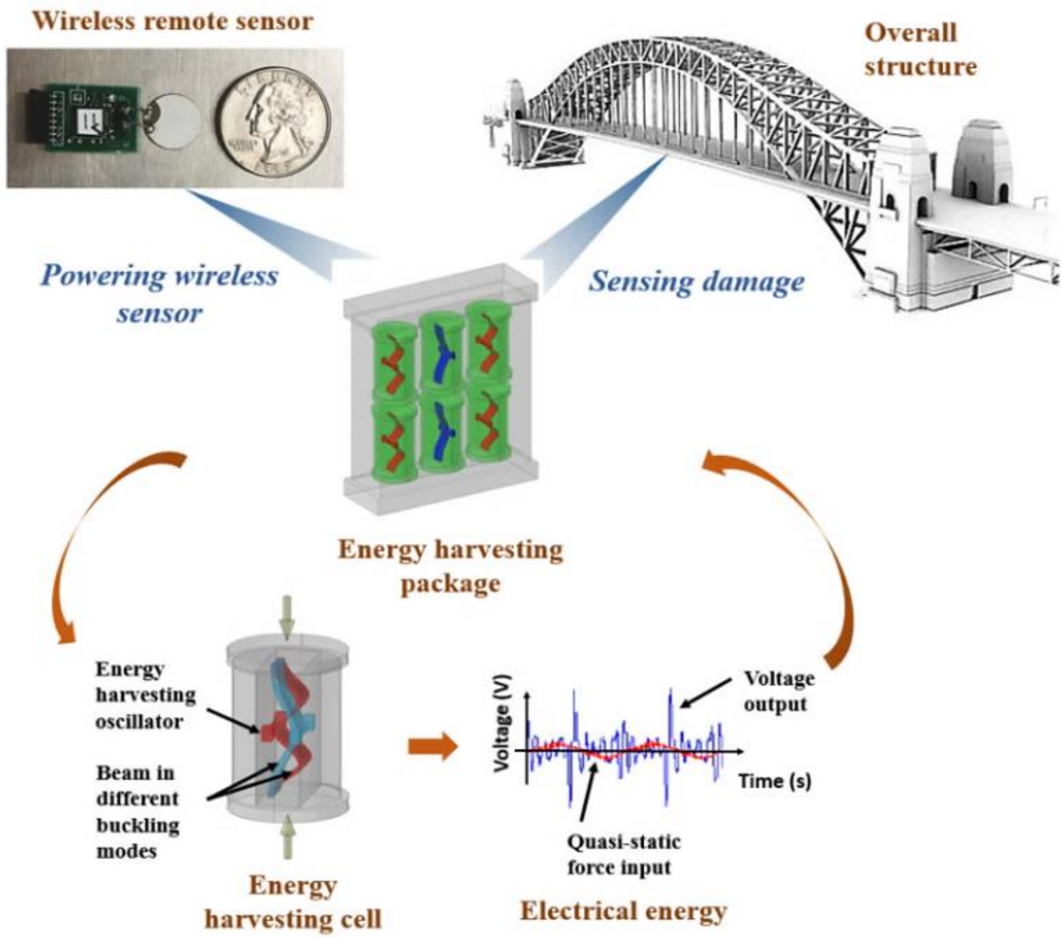

Figure 1-1. Concept of the post-buckling-based energy harvesting device for powering wireless sensor.

1.3. Research Hypotheses and Objectives

1.3.1. Hypotheses

The hypotheses in this study are given as

Electrical power can be generated under quasi-static excitations based on the post-buckling response of bilaterally constrained beams between different equilibrium positions.

According to this hypothesis, the instabilities of the post-buckled elements can be exploited to transform low-amplitude and low-rate motions and ambient deformations into amplified, dynamic inputs, such that the attached piezoelectric transducers can be activated to generate electrical energy.

> *The generated electrical power can be maximized by accurately controlling the post-buckling response of the bilaterally confined beam systems*.

According to this hypothesis, the post-buckling response can be controlled by tuning the geometry properties of the bilaterally constrained systems, such that the electrical output can be optimized.

1.3.2. Objectives

The main research objectives of this study are

1) Developing a postbuckling-based technique for energy harvesting and damage sensing under quasi-static excitations; and
2) Optimizing the harvesting efficiency and sensing accuracy of the technique by controlling the mechanical response of the structural instability-induced system.

In order to achieve the objectives, theoretical models are developed in this work to predict the post-buckling response of bilaterally constrained beams based on small and large deformation theories. In particular, a model is developed to theoretically predict and control the post-buckling response of bilaterally confined, non-uniform beams under small deformation assumptions. As uniform prismatic beams do not allow for such control, non-prismatic cross-section beams are herein investigated regarding the effects of different shapes and geometries on the post-buckling response. Satisfactory agreements are obtained between the theoretical prediction and experimental validation. Piezoelectric scavengers with different natural frequencies are then used to convert the high-rate motions of the deflected beams at buckling transitions into electrical power. Moreover, a large deformation model is developed capture the buckling snap-through of the bilaterally constrained systems under large deformation assumptions. The developed model investigates the static and dynamic instabilities of bilaterally constrained beams subjected to gradually increasing loading using large deformation theory. The model takes into account the impact of constraints gap under different constraint scenarios. In particular, if the gap is relatively small comparing to beam length, the system buckles and snaps into higher modes under compression.

1.4. Outline

This work is deployed as following,

- Chapter 2 summarizes a background review of buckling and post-buckling analysis in multiscale, i.e., micro/nanoscale and macroscale buckling analyses.
- Chapter 3 presents an energy harvesting and damage detecting mechanism based on non-prismatic beams. A small deformation model is developed to investigate the post-buckling response of the non-uniform system. The model is then used to optimize the geometry properties of the proposed mechanism, such that to control the generated electrical power/signal for efficient energy conversion and accurate damage detection. The theoretical results are validated with experimental predictions.
- Chapter 4 proposes a theoretical model based on large deformation assumptions. The large deformation model is developed with respect to clamped-clamped and simply supported

boundary conditions. Experimental validation is carried out to demonstrate the accuracy of the proposed model.

- Chapter 5 investigates the effect of the shape configuration of bilateral constraints on the post-buckling response of the beam systems. Linear and sinusoidal shapes are particularly studied. In addition, parametric studies are conducted to examine the similarity and difference between the small and large deformation models.
- Chapter 6 summarized the main findings of this study, as well as the recommendations for future study.

CHAPTER 2

RESEARCH BACKGROUND

2.1. Overview

Buckling has been expensively considered as a critical failure limit state and, therefore, many research efforts have been dedicating to characterizing its instable response and preventing it from happening (Pircher and Birdge, 2001; Xia et al., 2010; Jiao et al., 2012; Chen et al., 2013). In recent years, research interests have shifted to the potential of exploiting these elastic instabilities into “smart applications” (Hu and Burgueno, 2015; Safa and Hocker, 2015; Lajnef et al., 2015). Buckled elements have been implemented to develop monostable, bistable and multi-stable mechanisms that displayed great efficiency in a number of applications, including actuation, sensing, and energy harvesting (Erturk et al., 2010; Liu et al., 2008; Soliman et al., 2008; Kim et al., 2011). For example, buckling-based energy harvesting mechanisms are developed to transform ambient energies, i.e., strain, vibration, into electrical energy such that remote wireless sensors can be powered without the limitations of battery lifetime or wiring harness (Lajnef et al., 2014; Lajnef et al., 2012). Thanks to the energy harvesters, the wireless sensors have been deployed in civil infrastructures for the utilities of health monitoring and damage sensing (Park et al., 2008; Salehi and Burgueno, 2016; Salehi et al., 2015; Alavi et al., 2017; Hasni et al., 2017 Alavi et al., 2016; Alavi et al., 2015). In order to investigate the buckling and post-buckling response of slender/thin elements such that the performance of these mechanisms can be sufficiently improve, many analyses have been conducted in micro/nanoscale and macroscale with respect to different types of applications (Xu et al., 2015; Xu et al., 2012).

Eltaher et al. (2016) have reviewed nonlocal elastic models with respect to the applications of nanoscale beams in bending, buckling, vibration and wave propagation. However, a topical review regarding buckling and post-buckling analysis in different scales have not been conducted.

2.2. Multiscale Buckling and Post-Buckling Analysis

In micro/nanoscale buckling analysis, a variety of theories have been developed (Yang et al., 2002; Lam et al., 2003; Wang, 2005; Reddy, 2007; Park and Gao, 2006). Classical continuum theory has been conducted to examine the behavior of microbeams (Mehner et al., 2000; Abdel-Rahman et al., 2002). Since a significant size dependency is observed in small length scale, however, it is of necessity to take into account size dependent factors in theoretical studies. Conventional theories of mechanics are insufficient in determining the size dependence of deformed materials in microscale and, hence, different theories have also been developed to study the size effect of the slender beams in microscales such as nonlocal elasticity theory, non-classical couple stress elasticity theory, and strain gradient elasticity theory.

The nonlocal elasticity theory has been firstly presented by Erigen using global balance laws and the second law of thermodynamics to investigate the deformation behavior of materials in microscale by measuring the size dependence (Erigen and Edelen, 1972; Eringen, 1983). Different higher-order elasticity theories have been used to develop microstructure beam models. Peddieson et al. (2003) and Wang (2005) have presented a nonlocal continuum model to study the wave propagation in carbon nanotubes using both Euler-Bernoulli and Timoshenko beam theories. Based on the constitutive equations developed by Erigen (1972), many studies have been proposed (Lei et al., 2013; Thai, 2012; Thai and Vo, 2012; Wang et al., 2006; Aydogdu, 2009; Simsek and Yurtcu, 2013). Reddy (2007) has developed nonlocal theories for bending, buckling and vibration of Bernoulli-Euler, Timoshenko, Reddy and Levinson beams using Hamilton's principle. According to the stress-strain relationship of a composite beam, governing equations of anisotropic beams have been obtained using an energy method in this study. Xia et al. (2010) have investigated the static bending, post-buckling and free vibration of nonlinear non-classical microscale beams. Both studies investigated the size effect by introducing the material length scale factor in the context of non-classical continuum mechanics. Nonlinear equations of motion have been derived in a variational formulation by using a combination of the modified couple stress theory and Hamilton's principle. Ghannadpour et al. (2013) examined the buckling behavior of nonlocal Euler-Bernoulli beams using Ritz method. Based on the nonlocal beam/plate theory, Pradhan and Murmu (2009; 2010), Murmu and Pradhan (2009; 2009), and Malekzadeh and Shojaee (2013) have investigated the buckling performance of composite laminated micro/nanobeams using differential quadrature method (DQM).

The classical couple stress elasticity theory was developed by Koiter (1969). Later on, the non-classical couple stress theory was developed. Couple stress theories have been developed and extensively studied to narrow the research gap and identify the size dependence. Yang et al. (2002) has developed a modified/non-classical couple stress theory that has simplified the size effect into an internal material length scale factor in the governing equations. Park and Gao (2006) have developed a modified couple stress theory to investigate the bending of microscale Euler-Bernoulli beams. In their study, the authors captured the size effect by taking into account the internal material length scale parameter. Anthoine (2000) expended the theory to the case of pure bending of circular cylinder. Thai et al. (2015) have examined static bending, buckling and free vibration responses of size-dependent functionally graded sandwich microbeams using modified couple stress theory and Timoshenko beam theory. Using the modified couple stress theory, the size dependent behavior of functionally graded sandwich microbeams and the three-dimensional motion characteristics of temperature-dependent Timoshenko microbeams have been studied (Farokhi and Ghayesh, 2015). Kahrobaiyan et al. (2011) studied the nonlinear forced vibrational behaviors of Euler-Bernoulli beams based on the modified couple stress theory. This non-classical couple stress theory has been later extended in many studies. Abadi and Daneshmehr (2014) have extended the nonlocal couple stress theory to composite laminated materials for both Euler-Bernoulli and Timoshenko beams. Al-Basyouni et al. (2015) used a modified couple stress theory to investigate the bending and dynamic behaviors of functionally graded microbeams. Simsek and Reddy (2013) and Simsek et al. (2013) used a higher order beam theory to study buckled functionally graded microbeams.

The strain gradient elasticity theory was carried out to study the bending and stability of elastic Euler-Bernoulli beams and investigate the size dependence of microbeams (Fleck et al., 1994; Lam et al., 2003; Papargyri-Beskou et al., 2003; Giannakopoulos and Stamoulis, 2007; Kong et al., 2009; Wang, 2010; Akgoz and Civalek, 2012; 2013; Gao and Park, 2007). Using the theory, higher-order Bernoulli-Euler beam models were developed by Lam et al. (2003) and Papargyri-Beskou et al. (2003). Lam et al. (2003) used higher-order metrics in a gradient elasticity-based model to capture the strain gradient response of cantilevered beams. Following this work, Giannakopoulos and Stamoulis (2007) have theoretically studied the bending and cracked bar tension of a cantilever beam within the gradient elasticity framework. Kong et al. (2009) have studied the static and dynamic responses of Euler-Bernoulli microbeams using the gradient elasticity theory. Wang (2010) developed a theoretical model to examine the wave propagation of fluid-conveying single-walled carbon nanotubes by taking into account both inertia and strain gradients. Akgoz and Civalek (2012; 2013) have presented a higher-order shear deformation beam model based on the modified strain gradient theory. Gao and Park (2007) proposed a variational formulation based on simplified strain elasticity theory. In macroscale buckling analysis, many studies have been conducted on buckling performance of beams and plates without lateral constraints in the longitudinal direction. According to deformation of the buckled elements, small and large deformation theories are developed, especially with respect to slenderness ratio or the ratio of deflection and element length R. In particular, if the ratio is small, i.e., $R \ll 1$, the end-shortening/longitudinal displacement of the system is negligible and the small deformation theory is applicable. However, if the element is critical deformed while the ratio is relatively large, namely $R \sim 1$, large deformation theory needs to take into account. In order to effectively capture and predict the post-buckling response of deflected systems, a variety of theoretical models are developed.

Based on small deformation assumptions, many studies have been conducted. Zenkour (2005) has studied the buckling response of functionally graded sandwich. Zhao et al. (2008) have developed a theoretical model to determine the response of a polynomial curved beam under gradually increased external forces. A theoretical model is developed by Jiao et al. (2012; 2012) and Chen et al. (2013) to measure the local buckling behavior of composite I-beams with sinusoidal web geometry. Lajnef et al. (2014) and Borchani et al. (2015) developed a theoretical model to measure a slender beam under both fixed, bilateral constraints under small deformation assumptions. The model has accurately predicted the post-buckling response of uniform cross-section beams subjected to a gradually increasing axial force. The model has been used to examine the effect of geometry properties on the post-buckling response of elastic beams. Jiao et al. (2016; 2017) expended the theoretical model to non-uniform beam configurations such that the post-buckling response can be effectively controlled and tuned. Due to the orthogonality of the general solution, the superposition method is used to achieve a mode function that linearly combines different buckling modes. In order to investigate the buckling response of different types of functionally graded materials (FGMs), many studies have been developed based on first- or higher-order shear deformation theory (Thai and Vo, 2013; Meiche et al., 2011; Najafizadeh and Heydari, 2008; Librescu et al., 1989; Shariat and Eslami, 2007; Bodaghi and Saidi, 2010; Zhao et al., 2009; Wu et al., 2007; Ma and Wang, 2004; Neves et al., 2013; Saidi and Baferani, 2010; Najafizadeh and Heydari, 2004; Matsunaga, 2009; Najafizadeh and Eslami, 2002; Shariat et al., 2005; Hosseini-Hashemi et al., 2011; Ma and Wang, 2003; Li et al., 2007; Naderi and Saidi, 2010; Dung and Hoa, 2013; Giannakopoulos, and Stamoulis, 2007). Post-buckling analysis has been used in many applications to investigate structural instability. The delamination of composite elements due to buckling and post-buckling has been studied by (Nilsson et al., 2001; Davidson, 1991; Sciuva, 1986; Nilsson et al., 1993; Thai and Kim, 2011; Gaudezi et al., 2001). Subsea pipeline buckling is studied by Croll (1997), Karampour et al. (2013), Taylor and Tran (1996), Wang et al. (2011), Shi et al. (2013). Thin-membrane buckling behavior is examined by Sahhaee-Pour (2009), Jiang et al. (2008), Jiang et al. (2008), Amirbayat and Hearle (1986). In order to efficiently control the post-buckling response of bilaterally constrained slender beams, many studies have been conducted on varying the geometry properties of the system (Li et al., 1994; Li, 2001; Huang and Li, 2010). Elishakoff and Candan (2001) have presented a theoretical solution for freely vibrating functionally graded beams. More recently, Malekzadeh and Shojaee (2013) have examined the surface and nonlocal effects of freely vibrating non-uniform cross-section beams in nanoscale. Jiao et al. (2016; 2017) have developed an energy method-based model to investigate the post-buckling response of a beam with non-uniform cross-sections.

In order to theoretically identify the post-buckling response of largely deformed beams, many theories have been developed (Howell and Midha, 1995; Chen et al., 2011; Byklum and Amdahl, 2002; Wang et al., 2008; Song et al., 2008; Santos and Gao, 2012; Banerjee et al., 2008; Shen, 1999; Shvartsman, 2007; Lee, 2002; Chai, 1991 and 1998; Srivastava and Hui, 2013 A&B; Chen et al., 1996; Solano-Carrillo, 2009; Sofiyev, 2014; Bigoni, 2012; Bosi et al., 2015; Wang, 2009; Katz and Givli, 2015; Chang and Sawamiphakdi, 1982; Doraiswamy et al., 2012; Ram, 2016). Howell and Midha (1995) numerically solved the buckling instability of a tip loaded cantilever beam under large deformation assumptions. Shvartsman (2007) and Lee (2002) presented theoretical models to study the large deflection behavior of non-uniform cantilever beam under tip load. A finite-deformation theory was developed by Song et al. (2008) to investigate the behavior of thin buckled films on compliant substrates. Solano-Carrillo (2009) theoretically solved the large-deformed buckling response of cantilever beams under both tip and uniformly distributed loads. Santos and Gao (2012) presented a canonical dual mixed numerical method for post-buckling analysis of elastic beams under large deformation assumptions. Sofiyev (2014) studied the large deformation performance of truncated conical shells under time dependent axial loads using superposition principle and Galerkin procedure. Bigoni (2012) and Bosi et al. (2015) theoretically and numerically examined the injection of an elastic rod with gradually increased length. Buckling analysis is carried out based on the total potential energy of the system. Geometric equilibrium equations are used to solve for the critical buckling load. Chai (1998) presented a theoretical model to study large rotations that occur to a bilaterally constrained beam subjected to an axial force. Geometric equilibrium is applied to the model to achieve large end-shortening that caused by buckling deformation. The model accurately predicts different buckling statuses, i.e. point touching that deformed beam touches the lateral constraints, and flattening that the touching point increases to a flattening line contact. Under the assumption that the gap between the bilateral constraints is not smaller than a certain value, however, the large deformation model is limited to only the first buckling mode, which does not take into account buckling mode transition. A variety of constraints along beam length are added to achieve higher buckling modes beyond the bistable configurations. Due to the control in the transverse direction, the slender beam buckles to the first mode until it touches the constraints. Increasing the external force, the system jumps through a suddenly unstable status to reach the steady third buckling mode, and thereby regaining stiffness for greater loading. Many geometric assumptions have taken into account in the previous theoretical studies to measure such post-buckling response. Srivastava and Hui (2013 A&B) theoretically studied both the adhesionless and adhesive contacts of a pressurized neo-Hookean plane-strain membrane against a rigid substrate under large deformation assumptions. Katz and Givil (2015) theoretically studied the post-buckling response of a beam subjected to bilateral constraints, i.e. one fixed wall and one springy wall that moves laterally against a spring. Geometric compatibility is used to solve the governing equations under both small and large deformation assumptions. Chang and Sawamiphakdi (1982) have presented a numerical model to measure the post-buckling response of shell structures. Doraiswamy et al. (2012) have developed an approach to find the minimum energy of a largely deformed system using Viterbi algorithm. Ram (2016) studied the large deformation of flexible rods and double pendulum systems using Rayleigh-Ritz-based finite difference approach. Figure 2-1 presents the distributions of the research efforts on buckling and post-buckling in recent years with respect to the nonlocal, couple stress, and strain gradient

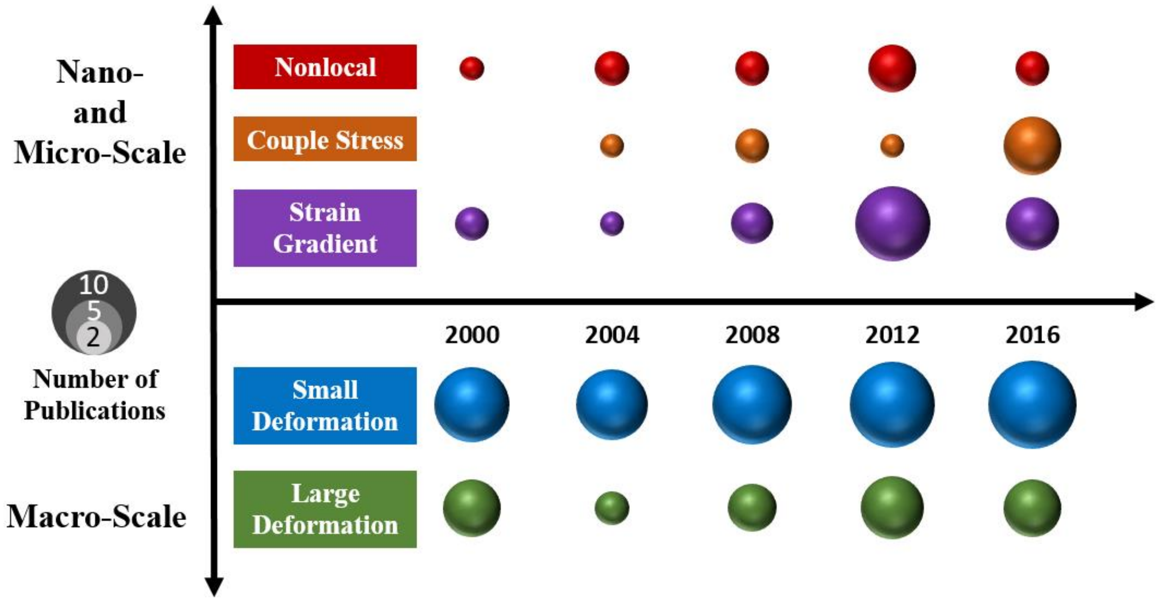

Figure 2-1. Number of publications on buckling and post-buckling analysis in multiscale.

theories in micro/nanoscale, and the small and large deformation theories in macroscale, respectively.

2.3. Micro/Nanoscale Buckling Analysis

2.3.1. Nonlocal Elasticity Theory

Using the nonlocal differential constitutive relations by Eringen (1972; 1983), Reddy (2007) has reformulated different beam theories, i.e., Euler-Bernoulli, Timoshenko, Reddy, and Levinson. The nonlocal constitutive relations for those beam theories are given as,

$$\begin{cases} \sigma_{xx} - \mu \dfrac{\partial^2 \sigma_{xx}}{\partial x^2} = E\varepsilon_{xz} \\ \sigma_{xz} - \mu \dfrac{\partial^2 \sigma_{xz}}{\partial x^2} = 2G\varepsilon_{xz} \end{cases} \tag{2-1}$$

where E, G and μ are Young's modulus, shear modulus, and nonlocal parameter given as $\mu = {e_0}^2 l^2$, respectively. e_0 is a material constant and l refers to internal microscale length factor of the material. Note that a force-strain relationship held in all the beam theories is given as,

Table 2-1. Constitutive relations and Euler-Lagrange equations for Euler-Bernoulli, Timoshenko, Reddy, and Levinson beam theories.

	Euler-Bernoulli	**Timoshenko**
Euler-Lagrange Equations	$\begin{cases} \frac{\partial}{\partial x}\left(N\frac{\partial w}{\partial x}\right) - \frac{\partial^2 M}{\partial x^2} = q \\ \frac{\partial N}{\partial x} + f = 0 \end{cases}$	$\begin{cases} \frac{\partial}{\partial x}\left(N\frac{\partial w}{\partial x}\right) - \frac{\partial Q}{\partial x} = q \\ \frac{\partial M}{\partial x} - Q = 0 \end{cases}$
Constitutive Relations	$M - \mu\frac{\partial^2 M}{\partial x^2} = EI\kappa$	$\begin{cases} M - \mu\frac{\partial^2 M}{\partial x^2} = EI\kappa \\ Q - \mu\frac{\partial^2 Q}{\partial x^2} = GAK_s\gamma \end{cases}$
	Reddy	**Levinson**
Euler-Lagrange Equations	$\begin{cases} \frac{\partial}{\partial x}\left(N\frac{\partial w}{\partial x}\right) - \frac{\partial \hat{Q}}{\partial x} - c_1\frac{\partial^2 P}{\partial x^2} = q \\ \frac{\partial \widehat{M}}{\partial x} - \hat{Q} = 0 \end{cases}$	$\begin{cases} \frac{\partial}{\partial x}\left(N\frac{\partial w}{\partial x}\right) - \frac{\partial Q}{\partial x} = q \\ \frac{\partial M}{\partial x} - Q = 0 \end{cases}$
Constitutive Relations	$\begin{cases} M - \mu\frac{\partial^2 M}{\partial x^2} = EI\kappa + EJ\rho \\ P - \mu\frac{\partial^2 P}{\partial x^2} = EJ\kappa + EK\rho \\ Q - \mu\frac{\partial^2 Q}{\partial x^2} = GA\gamma + GI\beta \\ R - \mu\frac{\partial^2 R}{\partial x^2} = GI\gamma + GJ\beta \end{cases}$	$\begin{cases} M - \mu\frac{\partial^2 M}{\partial x^2} = EI\kappa + EJ\rho \\ Q - \mu\frac{\partial^2 Q}{\partial x^2} = GA\gamma + GI\beta \end{cases}$

$$N - \mu \frac{\partial^2 N}{\partial x^2} = EA\varepsilon_{xx}^0 \tag{2-2}$$

where K_s, f, q and N are the shear correction factor, axial force, and transverse force in the axial and transverse directions, respectively. h is the beam height, P and R are the stress resultants exist only in the higher-order theories. $(A, I, J, K) = \int_A (1, z^2, z^4, z^6) dA$, $\widehat{M} = M - \frac{4}{3h^2} P$ and $\hat{Q} = Q - \frac{4}{h^2} R$. The constitutive relations and time-independent Euler-Lagrange equations for different beam theories are summarized in Table 2-1.

Substituting the Euler-Lagrange equations into the constitutive relations in Table 2-1, the governing equations based on the (a) Euler-Bernoulli, (b)Timoshenko, (c) Reddy, and (d) Levinson beam theories are obtained, respectively, as,

$$\frac{\partial^2}{\partial x^2}\left(-EI\frac{\partial^2 w}{\partial x^2}\right) + \mu \frac{\partial^2}{\partial x^2}\left[\frac{\partial}{\partial x}\left(N\frac{\partial w}{\partial x}\right) - q\right] + q - \frac{\partial}{\partial x}\left(N\frac{\partial w}{\partial x}\right) = 0 \tag{2-3a}$$

$$\begin{cases} \dfrac{\partial}{\partial x}\left[-GAK_s\left(\phi + \dfrac{\partial w}{\partial x}\right)\right] + q - \dfrac{\partial}{\partial x}\left(N\dfrac{\partial w}{\partial x}\right) - \mu\dfrac{\partial^2}{\partial x^2}\left[q - \dfrac{\partial}{\partial x}\left(N\dfrac{\partial w}{\partial x}\right)\right] = 0 \\ \dfrac{\partial}{\partial x}\left(EI\dfrac{\partial \phi}{\partial x}\right) - GAK_s\left(\phi + \dfrac{\partial w}{\partial x}\right) = 0 \end{cases} \tag{2-3b}$$

$$\begin{cases} G\tilde{A}\left(\dfrac{\partial \phi}{\partial x} + \dfrac{\partial^2 w}{\partial x^2}\right) - \dfrac{\partial}{\partial x}\left(N\dfrac{\partial w}{\partial x}\right) + q + \mu\dfrac{\partial^2}{\partial x^2}\left[\dfrac{\partial}{\partial x}\left(N\dfrac{\partial w}{\partial x}\right) - q\right] + \\ \qquad \dfrac{4}{3h^2}\left[EJ\dfrac{\partial^3 \phi}{\partial x^3} - \dfrac{4}{3h^2}EK\left(\dfrac{\partial^3 \phi}{\partial x^3} + \dfrac{\partial^4 w}{\partial x^4}\right)\right] = 0 \\ E\hat{I}\dfrac{\partial^2 \phi}{\partial x^2} - \dfrac{4}{3h^2}E\hat{J}\left(\dfrac{\partial^2 \phi}{\partial x^2} + \dfrac{\partial^3 w}{\partial x^3}\right) - G\tilde{A}\left(\phi + \dfrac{\partial w}{\partial x}\right) = 0 \end{cases} \tag{2-3c}$$

$$\begin{cases} \frac{\partial}{\partial x} G\overline{A}\left(\phi + \frac{\partial w}{\partial x}\right) + q - \frac{\partial}{\partial x}\left(N\frac{\partial w}{\partial x}\right) + \mu\frac{\partial^2}{\partial x^2}\left[\frac{\partial}{\partial x}\left(N\frac{\partial w}{\partial x}\right) - q\right] = 0 \\ \frac{\partial}{\partial x}\left(EI\frac{\partial \phi}{\partial x}\right) - \frac{4}{3h^2}EJ\left(\frac{\partial^2 \phi}{\partial x^2} + \frac{\partial^3 w}{\partial x^3}\right) - G\overline{A}\left(\phi + \frac{\partial w}{\partial x}\right) = 0 \end{cases} \tag{2-3d}$$

where the variables are defined as,

$$\hat{I} = I - \frac{4}{3h^2}J, \qquad \hat{J} = J - \frac{4}{3h^2}K, \qquad \overline{A} = A - \frac{4}{h^2}I, \qquad \overline{I} = I - \frac{4}{h^2}J,$$
$$\text{and } \tilde{A} = \overline{A} - \frac{4}{h^2}\overline{I} \tag{2-4}$$

The influence of nonlocal parameter, $\mu = e_0^2 a^2$, on deflection and critical buckling load capacity are presented with respect to Euler-Bernoulli, Timoshenko, Reddy, and Levinson beam theories, when the ratio of beam length and thickness is $\frac{L}{h} = 10$, as shown in Figure 2-2 (Reddy, 2007). In addition, Euler-Bernoulli theory is used to investigate the effect of $\frac{L}{h}$ ratio. It can be seen that with the increasing of nonlocal parameter, the transverse deflections of the microbeams are enlarged, while the buckling loads and natural frequencies are reduced. In particular, Figure 2-2(b) presents that nonlocal parameter affects natural frequencies more significantly than buckling loads.

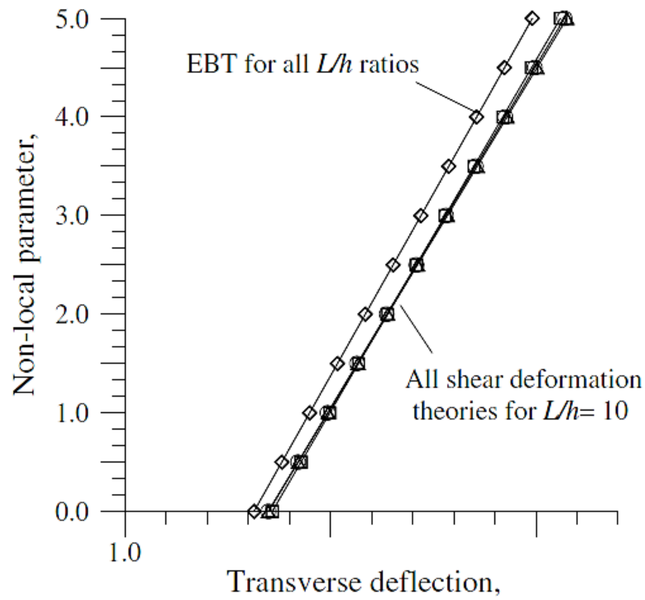

(a)

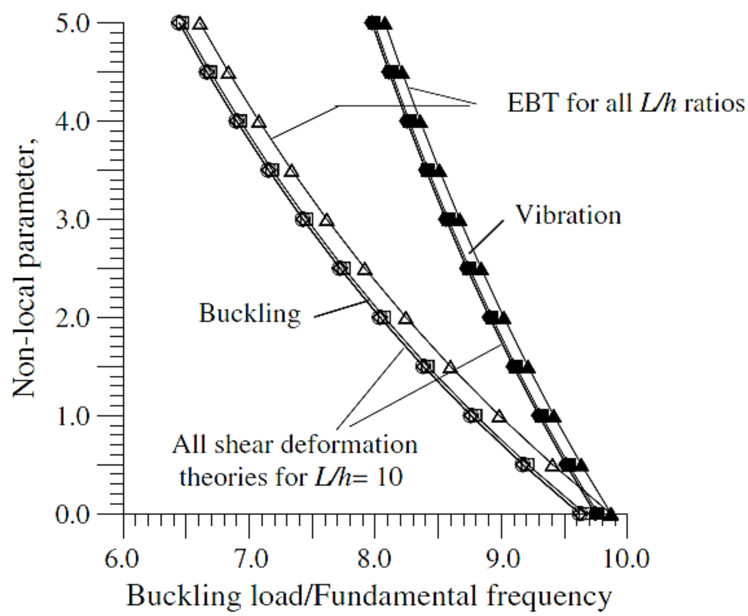

(b)

Figure 2-2. Influence of nonlocal parameter, μ, on (a) beam deflection, (b) buckling load and natural frequency (Reddy, 2007).

2.3.2. Non-Classical Couple Stress Elasticity Theory

In order to determine the microscale model, it is of desire to simplify the formulation to one material length scale factor in the couple stress elasticity theory (Park and Gao, 2006). Considering the deformed beam segment in Figure 2-3, the strain energy density consists of strain and curvature. Therefore, the work done by external forces can be written as,

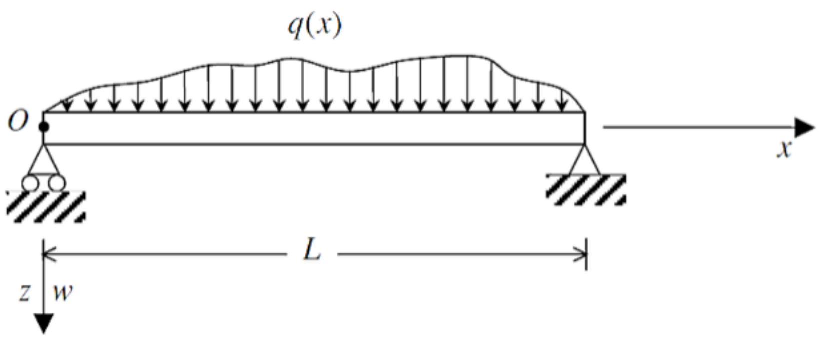

(a)

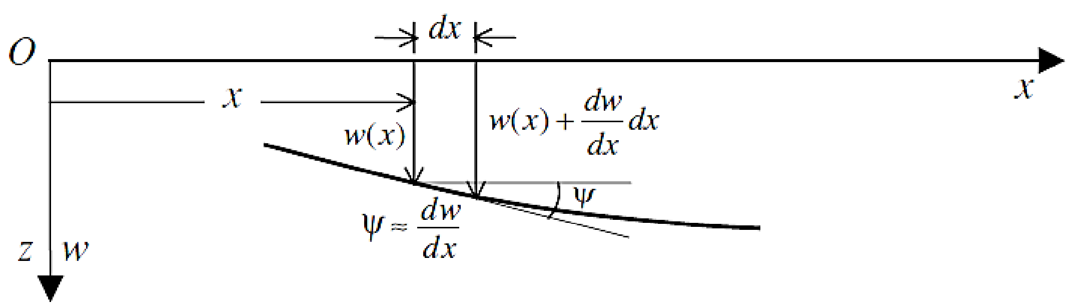

(b)

Figure 2-3**.** (a) Beam configuration and (b) diagram of a deflected segment (Park and Gao, 2006)

$$\begin{cases} W = \iiint\limits_{\Omega} (f \cdot u + c \cdot \theta) dv + \iint\limits_{\partial\Omega} (t \cdot u + s \cdot \theta) da \\ U = \dfrac{1}{2} \iiint\limits_{\Omega} (\sigma : \varepsilon + m : \chi) dv \end{cases} \tag{2-5}$$

where *f*, *c*, *t*, *s*, and **Ω** refer to the body force, body couple, traction, surface couple, and a region in the deformed linear elastic beam, respectively. σ, ε, m, χ indicate the stress tensor, strain tensor, deviatoric part of the couple stress tensor, symmetric curvature tensor, respectively.

Based on the Euler-Bernoulli beam theory, the total potential energy, Π, of the deflected beam is given as,

$$\Pi = U - W = -\frac{1}{2}\int_0^L \left(M_x + Y_{xy}\right)\frac{d^2 w}{dx^2}\,dx - \int_0^L q(x)w(x)dx \tag{2-6}$$

where $q(x)$, $w(x)$, M_x, and Y_{xy} indicate the external force, displacement in the transverse direction, resultant moment, and couple moment, respectively. The principle of minimum potential energy is applied to obtain the governing equation as $\delta\Pi = \delta U - \delta W = 0$.

Leading through the principle of minimum total potential energy, i.e., $\delta\Pi = 0$, for the stable equilibrium, a governing equation of isotropic Euler-Bernoulli beam is obtained as,

$$\frac{d^2 M_x}{dx^2} + \frac{d^2 Y_{xy}}{dx^2} + q(x) = 0 \tag{2-7}$$

The resultant, M_x, and couple moments, Y_{xy}, are given as,

$$
\begin{cases} M_x = \int_A \sigma_{xx} z \, dA = -EI \dfrac{d^2 w(x)}{dx^2} \\ Y_{xy} = \int_A m_{xy} \, dA = -\mu_L A l^2 \dfrac{d^2 w(x)}{dx^2} \end{cases} \tag{2-8}
$$

Substituting Eq. (2-8) into Eq. (2-7), the governing equation yields,

$$
-(EI + \mu_L A l^2) \frac{d^4 w(x)}{dx^4} = q(x) \tag{2-9}
$$

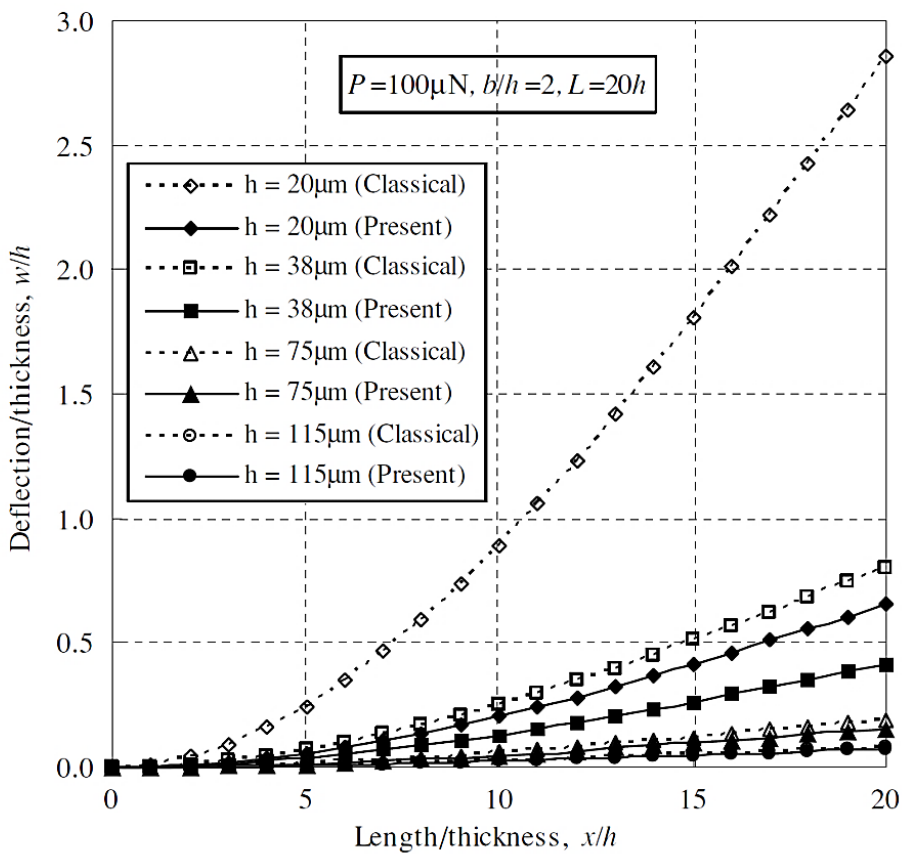

Figure 2-4. Comparison of beam deflection vs. length/thickness between classical and non-classical couple stress theories (Park and Gao, 2006)

where the bending rigidity of the beam, $EI + \mu_L A l^2$, is defined with respect to the microscale length factor l. μ_L is Lame's constant of the material. Note that the consideration of microstructure in the model can be eliminated by $l = 0$, which leads to the classical Euler-Bernoulli beam model. Figure 2-4 presents the deflection of a cantilevered beam with respect to length/thickness $\frac{x}{h}$ (Park and Gao, 2006). The length factor is given as $l = 17.6\,\mu$m. It can be seen that the deflection predicted by classical theories is overall larger. A severe overestimation is observed when beam thickness is $h = 20\,\mu$m, while the difference become negligible when beam thickness is approximately $h = 100\,\mu$m. Therefore, it indicates that size effect is only of significance in microscale.

The modified couple stress theory was later expended to composite laminated materials by Abadi and Daneshmehr (2014). In particular, the curvature tensor, χ, defined in Eq. (2-5) was modified to capture anisotropic materials. According to the stress-strain relationship of the composite beam, the principle of minimum potential energy in Eq. (2-6) is expended as,

$$\underbrace{\int_0^L b\left[\sum_{k=1}^{n}\int_{z_k}^{z_{k+1}} \sigma^k : \delta\varepsilon dz\right] dx - \frac{1}{2}\int_0^L P\delta\left(\frac{\partial w}{\partial x}\right)^2 dx}_{\delta U}$$
$$-\underbrace{\int_0^L \left[f_u\delta u + f_w\delta w + f_c\delta\theta_y\right] dx + \left[\overline{N}\delta u + \overline{V}\delta w + \overline{M}\delta\phi + \overline{Y}\delta\left(\frac{\partial w}{\partial x}\right)\right]\Bigg|_{x=0}^{x=L}}_{\delta W} = 0 \tag{2-10}$$

where f_u, f_w, f_c, $\overline{N}$, $\overline{V}$, $\overline{M}$, and $\overline{Y}$ are x component of the body force, z component of the body force, resultant of the y component of the body force, axial force, transverse shear force, bending moment due to normal stress, and bending moment due to couple stress tensor, respectively. P refer to the external force.

Based on the stable equilibrium, the governing equations of anisotropic Euler-Bernoulli beams are obtained as,

$$\begin{cases} \bar{Q}_{11}\dfrac{\partial^2 u}{\partial x^2} - \bar{J}_{11}\dfrac{\partial^3 w}{\partial x^3} + f_u = 0 \\ \bar{J}_{11}\dfrac{\partial^3 u}{\partial x^3} - \left(\bar{I}_{11} + \bar{\bar{Q}}_{44}\right)\dfrac{\partial^4 w}{\partial x^4} - P\dfrac{\partial^2 w}{\partial x^2} + f_w + \dfrac{\partial f_c}{\partial x} = 0 \end{cases} \tag{2-11}$$

and the governing equations of anisotropic Timoshenko beam are obtained as,

$$\begin{cases} \bar{Q}_{11}\dfrac{\partial^2 u}{\partial x^2} - \bar{J}_{11}\dfrac{\partial^3 w}{\partial x^3} + f_u = 0 \\ -\bar{J}_{11}\dfrac{\partial^2 u}{\partial x^2} - \bar{I}_{11}\dfrac{\partial^2 \Phi}{\partial x^2} + k_s\bar{Q}_{44}\left(-\Phi + \dfrac{\partial w}{\partial x}\right) + \dfrac{1}{4}\bar{Q}_{44}\left(\dfrac{\partial^2 \Phi}{\partial x^2} + \dfrac{\partial^3 w}{\partial x^3}\right) - \dfrac{1}{2}f_c = 0 \\ k_s\bar{Q}_{44}\left(\dfrac{\partial^2 w}{\partial x^2} - \dfrac{\partial \Phi}{\partial x}\right) - \dfrac{1}{4}\bar{Q}_{44}\left(\dfrac{\partial^3 \Phi}{\partial x^3} + \dfrac{\partial^4 w}{\partial x^4}\right) - P\dfrac{\partial^2 w}{\partial x^2} + f_w + \dfrac{1}{2}\dfrac{\partial f_c}{\partial x} = 0 \end{cases} \tag{2-12}$$

where $\bar{Q}_{11}$, $\bar{J}_{11}$, $\bar{I}_{11}$, $\bar{Q}_{44}$, and $\bar{\bar{Q}}_{44}$ are material properties of the laminated beam. In this theory, conventional equilibrium relation of force and its corresponding moment is used to formulate a governing equation. In addition, an equilibrium equation is developed to govern the response of the couple force-moment.

2.3.3. Strain Gradient Elasticity Theory

Papargyri-Beskou et al. (2003) have conducted a bending and stability analysis of Euler-Bernoulli beams by using a linear theory of gradient elasticity with surface energy. According to the constitutive relations, the Cauchy, double, and total stresses are given as,

$$\begin{cases} \tau_x = Ee_x + lEe'_x \\ \mu_x = lEe_x + g^2Ee'_x \\ \sigma_x = \tau_x - \dfrac{d\mu_x}{dx} = E\left(e_x - g^2\dfrac{d^2e_x}{dx^2}\right) = E(e_x - g^2e''_x) \end{cases} \tag{2-13}$$

where e_x, l and g^2 represent the axial strain of the beam in bending, material length factors of the surface and volumetric elastic strain energies, respectively. According to the variational principle, it is obtained,

$$\begin{aligned} \delta(U-W) &= \int_0^L \left[EI\left(w'''' - g^2w^{(6)}\right) + Pw''\right]\delta w dx \\ &+ \left[\left(V - \left(Pw' + EI\left(w''' - g^2w^{(5)}\right)\right)\right)\delta w\right]_0^L \\ &- \left[\left(M - EI(w'' - g^2w'''')\right)\delta\psi'\right]_0^L \\ &- \left[\left(m - EI(lw'' + g^2w''')\right)\delta w''\right]_0^L = 0 \end{aligned} \tag{2-14}$$

where *P*, *V*, *M* and *m* represents the external force, boundary shear force, and boundary classical and non-classical moments, respectively. Therefore, the governing equation of the deflected beam in bending can be expressed as,

$$EI\left(w'''' + g^2w^{(6)}\right) + Pw'' = 0 \tag{2-15}$$

Figure 2-5 shows the influence of gradient coefficient product, $c \cdot d = \frac{g}{D} \cdot \frac{D}{L}$, on the deflection of cantilevered microbeams (Papargyri-Beskou et al., 2003). *D* represents characteristic diameter of microbeams. Note that the model can be reducted to classical elastic when $c \cdot d = 0$. Figure 2-

5(a) displays that the deflection of gradient microbeams is reduced when increase the gradient coefficient product. Figure 2-5(b) and (c) indicates that influence of surface energy parameter, $\lambda = \frac{l}{g}$, on beam deflection, with respect to $c \cdot d = 0.05$ and $c \cdot d = 0.1$, respectively. It can be seen that the effect surface energy parameter λ on beam deflection can be neglible when $c \cdot d \leq 0.05$. However, the deflection is increased as enlarges λ when $c \cdot d > 0.05$.

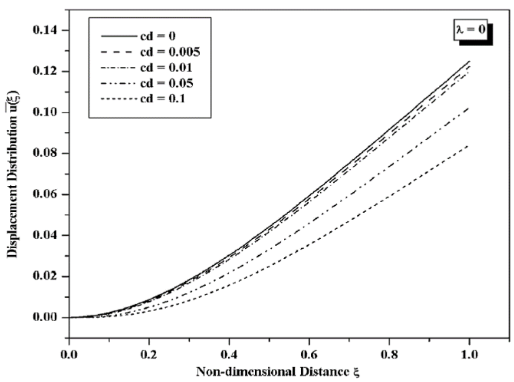

(a)

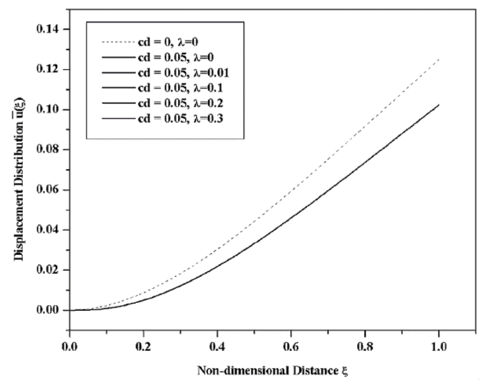

(b)

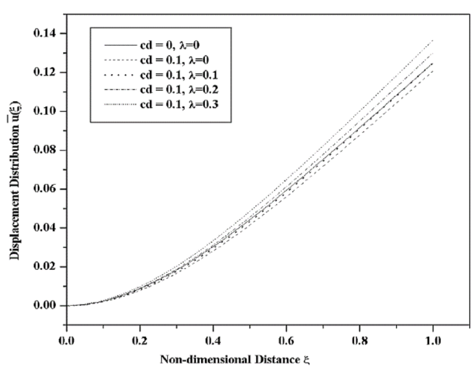

(c)

Figure 2-5. Influence of (a) gradient coefficient product $\boldsymbol{c \cdot d}$, (b) surface energy parameter ($\boldsymbol{c \cdot d = 0.05}$), and (c) surface energy parameter ($\boldsymbol{c \cdot d = 0.1}$) on beam deflection (Papargyri-Beskou et al., 2003).

2.4. Macroscale Buckling and Post-Buckling Analysis

2.4.1. Small Deformation Theory

2.4.1.1. Buckling Analysis

Many studies have been conducted based on small deformation assumptions. Since the deflection of a slender element is adequately small in small deformation theory, i.e., $w(x) \ll L$ and $\theta = \frac{dw}{dx}$, the displacement in the longitudinal direction is negligible, as shown in Figure 2-6. It can be seen that an initial point in the initially straight beam φ is vertically deflected to φ', and, therefore, only the transverse deflection, $w(x)$, is taken into account in the small deformation-based model. The buckling problem of clamped-clamped beams subjected to axial load in macroscale was studied by Nayfeh and Emam (2008). The governing equation is given by,

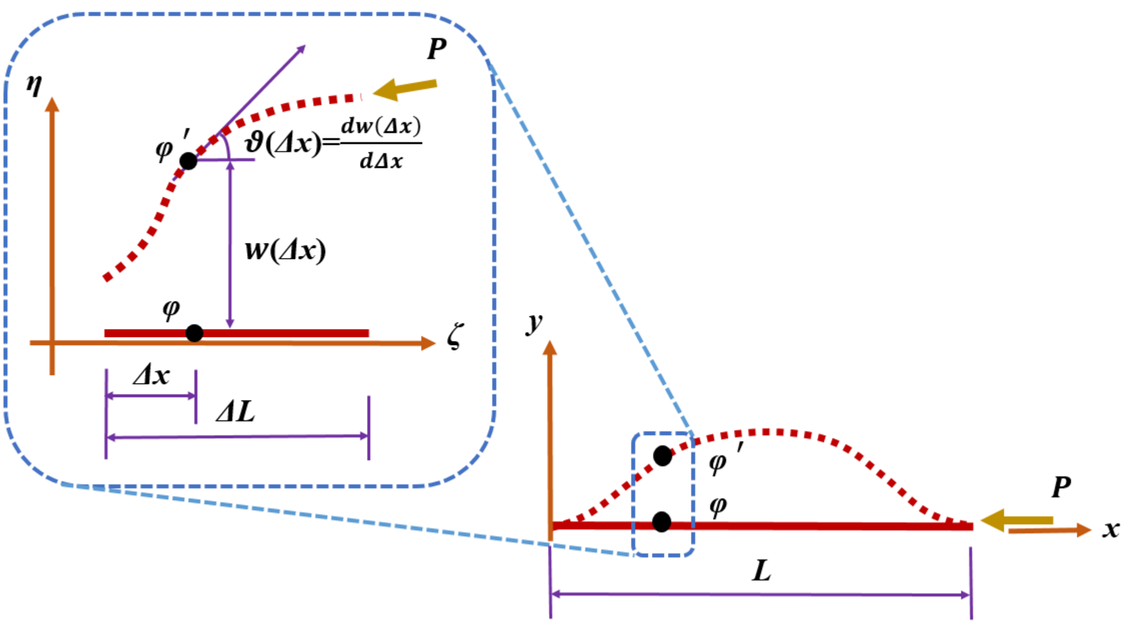

Figure 2-6. Schematic diagram of a deformed beam segment in the small deformation theory.

$$w'''' + \lambda^2 w'' = 0 \tag{2-16}$$

where $\lambda^2 = P - 1/2 \int_0^1 w'^2 dx$ is a constant that represents the critical buckling load.

The general solution for Eq. (2-16) is given as,

$$w(x) = c_1 + c_2 x + c_3 \cos(\lambda x) + c_4 \sin(\lambda x) \tag{2-17}$$

where the c_i are constants. Applying the fixed-fixed boundary conditions of the system, four algebraic equations can be obtained and, hence, an eigenvalue problem for λ is gained. Computing the determinant of the coefficient matrix and equating it to zero, the characteristic equation for λ is given by,

$$2 - 2\cos(\lambda) - \lambda \sin(\lambda) = 0 \tag{2-18}$$

Solving the characteristic equation in Eq. (2-18) results in two kinds of buckling modes: symmetric and antisymmetric. The shape function of the buckled beam is the summation of the two buckling mode types, i.e., $w(x) = w_s(x) + w_a(x)$, as,

$$w(x) = \underbrace{\sum_{s=1}^{n} \beta_s \big(1 - \cos(\lambda_s x)\big)}_{\text{Symmetric}} + \underbrace{\sum_{a=2}^{n+1} \beta_a \left(1 - 2x - \cos(\lambda_a x) + \frac{2}{\lambda_a} \sin(\lambda_a x)\right)}_{\text{Antisymmetric}} \tag{2-19}$$

where $\lambda_s = 2m\pi,\ m = 1,2, \dots$ and $\lambda_a = 2.86\pi, 4.92\pi, 6.94\pi, 8.95\pi, \dots$, and β are the weight coefficients that determine the contribution of each buckling mode to the general shape function.

2.4.1.2. *Post-Buckling Analysis Based on Equilibrium and Geometric Compatibility*

In order to investigate post-buckling performance, different types of lateral constraints have been placed on the system (Chai, 1998; Katz and Givli, 2015; Liu and Burgueno, 2016). The post-buckling response of a straight prismatic bilaterally constrained beam has been theoretically studied by Chai (1998) using small deformation assumptions. The beam is placed between two flat rigid walls separated by a distance h_0 such that it lies along the surface of one of the walls. Both of its ends are clamped. The net gap between the strip and the lateral constraints is denoted as $h = h_0 - t$. Under axial end shortening Δ, the beam buckles. The fourth-order linearized differential equation for an Euler beam under axial compression is the same as Eq. (2-16).

Figure 2-7 shows a beam subjected to a gradually compressive force P is adjacently placed between the bilaterally rigid constraints. Figure 2-7(a) demonstrates a schematic diagram of the deformed beam. Figure 2-7(b) indicates different buckling phases that the beam undergoes. The initially straight beam (stage (a)) will be buckled to the first mode (stage (b)) under compression. Point contact will be obtained when the deflected beam touches the constraints (stage (c)). The point contact between the deformed beam and walls grows to a line contact (stage (d)). Increasing the external force, the line contact reaches the critical condition and then snaps into the third buckling mode (stage (e)). Table 2-2 summarizes the shape functions and corresponding boundary conditions the beam undergoes in different buckling phases.

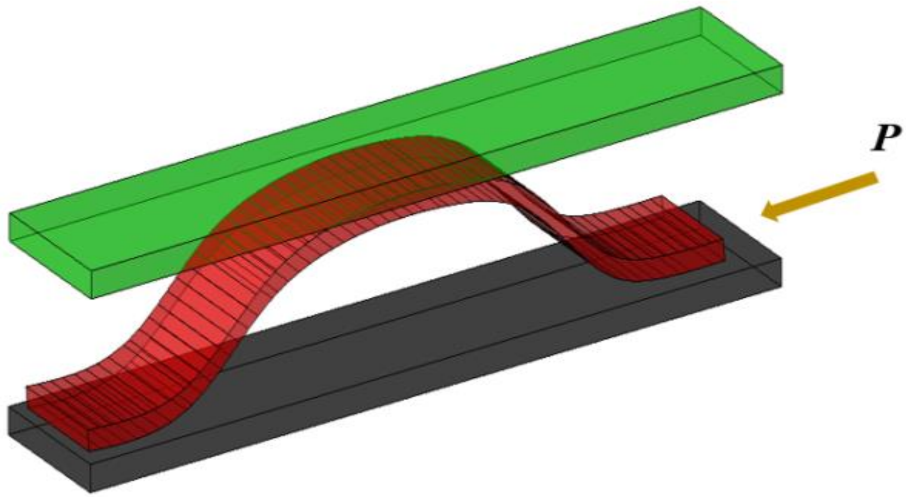

(a)

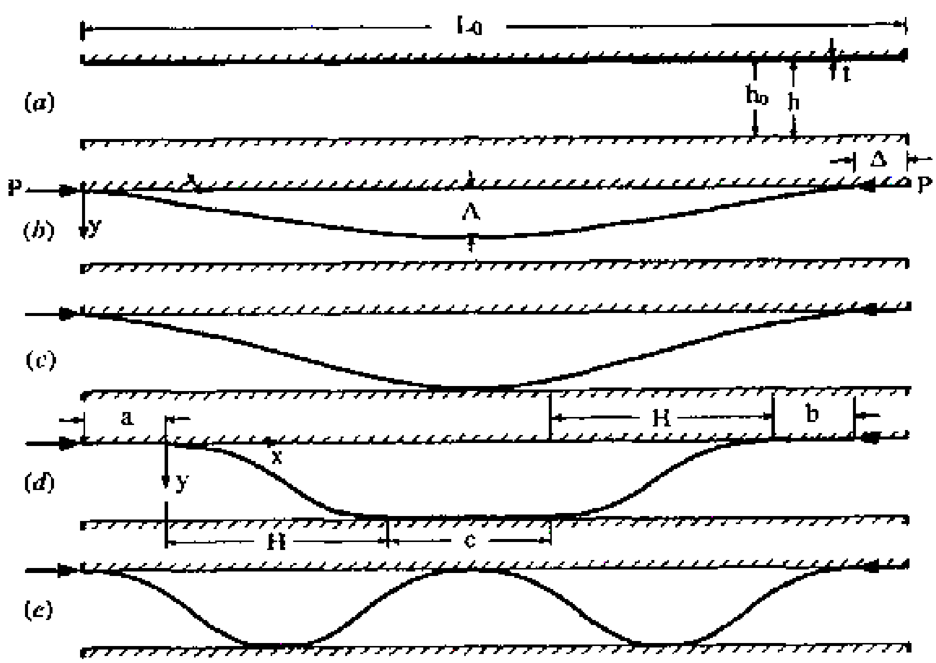

(b)

Figure 2-7. (a) Schematic diagram of a bilaterally constrained beam in the small deformation theory, and (b) different buckling phases of the beam (Chai, 1998).

Table 2-2. Shape functions and corresponding boundary conditions in different buckling phases.

Buckling Phase	**Shape Function**	**Boundary Conditions**
Stage (b): Pre-Contact	$w = \frac{A}{2}\left(1 - \cos\left(\frac{2\pi x}{L_0}\right)\right)$	$\left.\begin{matrix} w(0) \\ w'(0) \\ w(L_0) \\ w'(L_0) \end{matrix}\right\} = 0$
Stage (c): Point Contact	$w = h\frac{\sin\left(\frac{\pi\zeta\bar{x}}{n}\right) - \frac{\pi\zeta\bar{x}}{n} + \left(1 - \cos\left(\frac{\pi\zeta\bar{x}}{n}\right)\right)\tan\left(\frac{\pi\zeta}{2n}\right)}{2\left(\tan\left(\frac{\pi\zeta}{2n}\right) - \frac{\pi\zeta}{2n}\right)}$	$\left.\begin{matrix} w(0) \\ w'(0) \\ w'\left(\frac{L_0}{2}\right) \end{matrix}\right\} = 0$ $w\left(\frac{L_0}{2}\right) = h$
Stage (d): Line Contact	$w = h\frac{2\pi\bar{x} - \sin(2\pi\bar{x})}{2\pi}$ $\quad 0 \le \bar{x} \le 1$	$\left.\begin{matrix} w(0) \\ w'(0) \\ w''(0) \\ w'(H) \end{matrix}\right\} = 0$ $w(H) = h$
Stage (e): Mode Transition	$\begin{cases} \frac{kc}{2\pi} = \zeta - 2 & \text{Lower} \\ \frac{kc}{2\pi} = \frac{\zeta - 2}{3} & \text{Higher} \\ \frac{kc}{2\pi} = \frac{\zeta - 2}{2} & \text{Symmetry } 2a = 2b = c \end{cases}$	$a + b + c + 2H = L_0$

where $k^2 = \frac{P}{EI}$, $H = \frac{L_0}{2}$, $\bar{x} = \frac{x}{H}$, $\zeta = \frac{k\,L_0}{2\pi}$, and n represents buckling mode of the deformed beam.

2.4.1.3. Post-Buckling Analysis Based on Energy Method

Since the lateral constraints in Figure 2-8 allow the beam to buckle into higher modes rather than only deforms in the first mode, many studies have been conducted to determine the deformed beam shape configurations using energy method (Borchani et al., 2015; Jiao et al., 2016; Doraiswamy et al., 2012). The constraints are modeled as limits to the transverse deflection and, thus, the beam deformation is always bounded by the distance between the walls. Snap-through buckling from one mode into a higher mode configuration is induced when the total energy transits through an unstable path to a lower value represented by a different stable geometric configuration. Borchani et al. (2015) have investigated the post-buckling response of bilaterally constrained beams by mathematically modeling the system as a constrained minimization problem of the total energy,

$$\begin{cases} \mathrm{Min}[\Pi(\beta)] \\ 0 \leq w(x) \leq \mathrm{Gap} \end{cases} \tag{2-20}$$

where the weight coefficients β are defined in Eq. (2-19).

The total energy of the system consists of two components, e.g., total potential energy and kinetic energy. The potential energy is the summation of the bending and axial compression strain energies stored in the deformed elastic element and the potential energy due to external force. The potential energies u_b, u_c and $u_p$due to bending, compression and external applied force, respectively, are given by,

$$\begin{cases} u_b = \dfrac{1}{2} EI \displaystyle\int_0^L \left(\dfrac{d^2 w(x)}{dx^2}\right)^2 dx \\ u_c = \dfrac{1}{2} P \underbrace{\dfrac{P}{E} \displaystyle\int_0^L \dfrac{1}{bt} dx}_{\text{Length shortening due to comporession}} \\ u_p = \dfrac{1}{2} P \underbrace{\left(\dfrac{P}{E} \displaystyle\int_0^L \dfrac{1}{bt} dx + \overbrace{\dfrac{1}{2} \displaystyle\int_0^L \left(\dfrac{d^2 w(x)}{dx^2}\right)^2 dx}^{\text{Length shortening due to rotaiton}}\right)}_{\text{Total length shortening}} \end{cases} \tag{2-21}$$

Since the axial loading is quasi-static, the kinetic energy in the axial direction can be neglected. Therefore the kinetic energy u_k can be expressed by,

$$u_k = \frac{1}{2} \int_0^L m(x) \left(\frac{dw(x,t)}{dt}\right)^2 dx \tag{2-22}$$

where $m(x)$ represents mass per unit length. The expression $w(x,t)$ in the time and space coordinates can be separated using the Galerkin discretization method as,

$$\widehat{w}(x,t) = \sum_{r=1}^{\infty} C_r(t)\, w_r(x) \tag{2-23}$$

where $C_r(t)$ are the generalized temporal coordinate. The energy of the system can be expressed as,

$$\Pi = u_b + u_c + u_k - u_p$$

$$= \frac{1}{2} EI \int_0^L \left(\frac{d^2 w(x)}{dx^2}\right)^2 dx + \frac{1}{2} \int_0^L m(x) \left(\frac{\sum_{r=1}^{\infty} C_r(t)\, w_r(x)}{dt}\right)^2 dx - \tag{2-24}$$

$$\frac{1}{4}P\int_0^L\left(\frac{dw(x)}{dx}\right)^2 dx$$

Taking Eqs. (2-19) and (2-24) into Eq. (2-20), the weight coefficients β can be determined and, therefore, the shape function $w(x)$ of the deflected beam can be obtained.

2.4.1.4. Buckling Analysis under Different Conditions

Soong and Choi (1986) presented a theoretical formulation of the friction force generated by the dry contact between the buckled beam and the lateral rigid walls. The beam is modeled using Euler-Bernoulli beam theory and Coulomb model is used for the friction. Later on, Liu and Chen (2013) has investigated the effect of Coulomb friction on the contact behaviors between slender beams and straight channel with clearance.

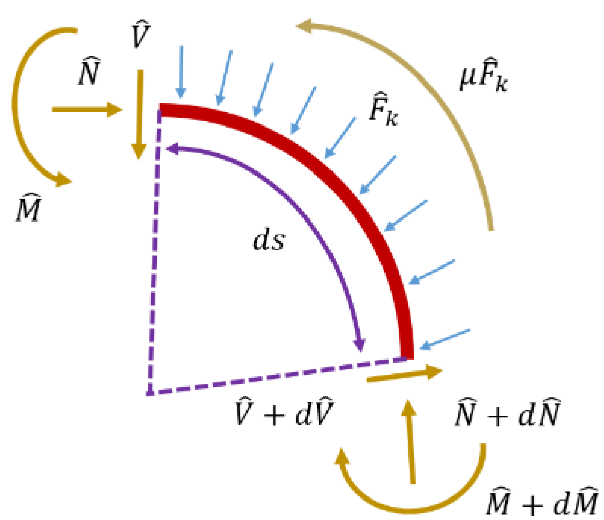

Figure 2-8. Equilibrium of a beam segment subjected to lateral pressure with friction (Redrawn based on Soong and Choi (1986)).

Figure 2-8 displays the force equilibrium of a buckled beam element subjected to normal pressure and tangential friction force where $\widehat{M}$ is the bending moment, $\widehat{N}$ is the axial compressive force, $\hat{V}$ is the transverse shear force, $\hat{F}_n$ is the normal pressure force, μ is the coefficient of friction, ds is the arc length of the element, and R is the local radius of curvature for the deformed beam. The tangential and normal forces at the contact zone are expressed as follow,

$$\begin{cases} \hat{F}_k = \widehat{N}\dfrac{d^2w}{ds^2} + EI\dfrac{d^4w}{ds^4} \\ \mu\hat{F}_k = EI\dfrac{d^3w}{ds^3}\dfrac{d^2w}{ds^2} - \dfrac{d\widehat{N}}{ds} \end{cases} \tag{2-25}$$

where μ_f refers to the friction coefficient between the beam and constraints. The variation of the axial compression force is governed by the following ordinary differential equation,

$$\frac{d\widehat{N}}{ds} + \mu_f N\frac{d^2w}{ds^2} = EI\left(\frac{d^3w}{ds^3}\frac{d^2w}{ds^2} - \mu_f\frac{d^4w}{ds^4}\right) \tag{2-26}$$

The solution $\widehat{N}$ to Eq. (2-26) is given as,

$$\widehat{N} = e^{-\int_{s_0}^{s} f(\tau)\,d\tau}\left(\widehat{N}_{s=s_0} + \int_{s_0}^{s} g(\xi)\,e^{\int_{\xi_0}^{\xi} f(\tau)\,d\tau}\,d\xi\right) \tag{2-27}$$

where

$$\begin{cases} f(s) = \mu_f\dfrac{d^2w}{ds^2} \\ g(s) = EI\left(\dfrac{d^3w}{ds^3}\dfrac{d^2w}{ds^2} - \mu_f\dfrac{d^4w}{ds^4}\right) \end{cases} \tag{2-28}$$

Substituting Eq. (2-27) into Eq. (2-25), the tangential friction force is expressed as,

$$\mu_f \hat{F}_n = \mu_f \left[e^{-\int_{s_0}^{s} f(\tau)\, d\tau} \left(\hat{N}_{s=s_0} + \int_{s_0}^{s} g(\xi)\, e^{\int_{\xi_0}^{\xi} f(\tau)\, d\tau}\, d\xi \right) \frac{d^2 w}{ds^2} + EI\, \frac{d^4 w}{ds^4} \right] \tag{2-29}$$

Due to the discontinuity of thickness and/or width, the potential energy is computed in each segment, and then the total potential energy is the sum of the partial energies. The bending and compression strain energies u_j^b and u_j^c, respectively, and the work of the external work, u_j^p, in the j^{th} segment, can be written, by changing Eq. (2-21), as (Jiao et al., 2016),

$$\begin{cases} u_j^b = \dfrac{1}{2} E_j \displaystyle\int_{L_{j-1}}^{L_j} I_j(x) \left(\frac{d^2 w(x)}{dx^2} \right)^2 dx \\ u_j^c = \dfrac{1}{2} \dfrac{P^2}{E_j} \displaystyle\int_{L_{j-1}}^{L_j} \frac{1}{b_j(x)\, t_j(x)}\, dx \\ u_j^p = \dfrac{1}{2} \dfrac{P^2}{E_j} \displaystyle\int_{L_{j-1}}^{L_j} \frac{1}{b_j(x)\, t_j(x)}\, dx + \dfrac{P}{4} \displaystyle\int_{L_{j-1}}^{L_j} \left(\frac{dw(x)}{dx} \right)^2 dx \end{cases} \tag{2-30}$$

Therefore, the potential energy of the system that contains a total of *n* segments is expressed as,

$$\Pi = \sum_{j=1}^{n} \left(u_j^b + u_j^c + u_j^k - u_j^p \right)$$

$$= \sum_{j=1}^{n} \left(\frac{1}{2} E_j \int_{L_{j-1}}^{L_j} I_j(x) \left(\frac{d^2 w(x)}{dx^2} \right)^2 dx + \frac{1}{2} \int_{L_{j-1}}^{L_j} m_j(x) \left(\frac{\sum_{r=1}^{\infty} C_r(t)\, w_r(x)}{dt} \right)^2 dx \right. \\ \left. - \frac{1}{4} P \int_{L_{j-1}}^{L_j} \left(\frac{dw(x)}{dx} \right)^2 dx \right) \tag{2-31}$$

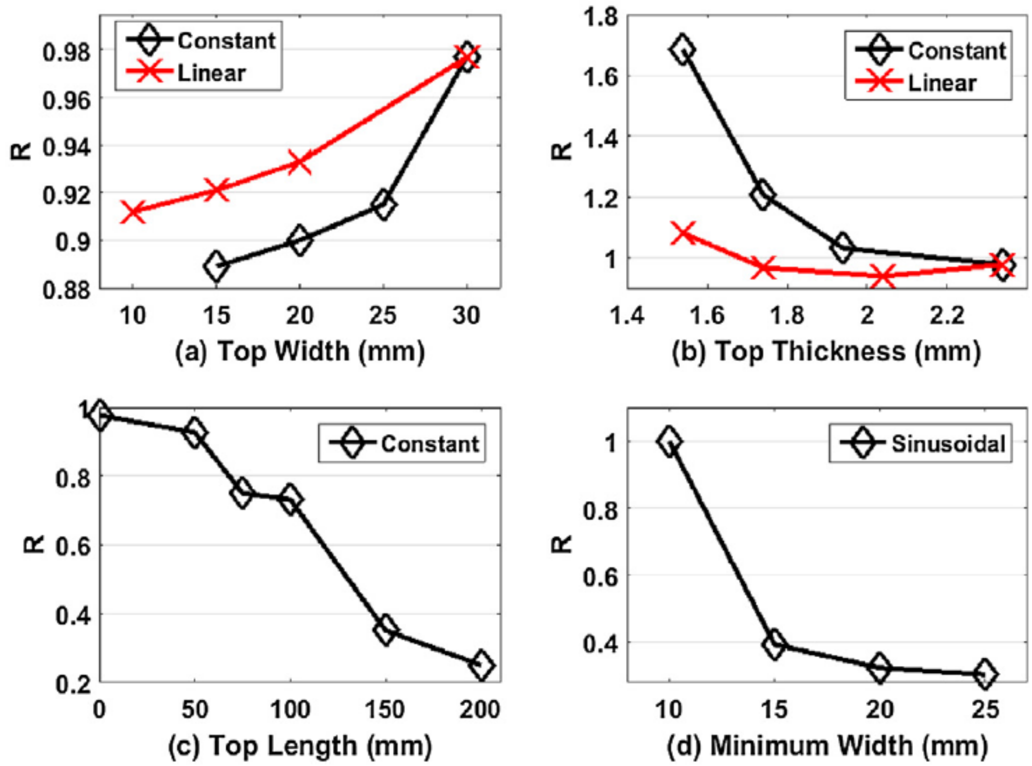

Figure 2-9. Schematic diagram of a deformed beam segment in the large deformation theory (Jiao et al. (2016)).

Figure 2-9 shows the variation of spacing ratio, $R = \frac{\Phi 7 - \Phi 5}{\Phi 5 - \Phi 3}$, with respect to different configurations of non-uniform beams (Jiao et al., 2016). Φ is defined as buckling mode transition in terms of axial force. It can be seen that buckling snap-through events can be sufficiently tuned by varying cross-section geometry of a beam.

2.4.2. Large Deformation Theory

Many theoretical models have been developed to examined the post-buckling response of largely deformed beams (Howell and Midha, 1995; Chen et al., 2011; Byklum and Amdahl, 2002; Wang et al., 2008; Song et al., 2008; Santos and Gao, 2012; Banerjee et al., 2008; Shen,

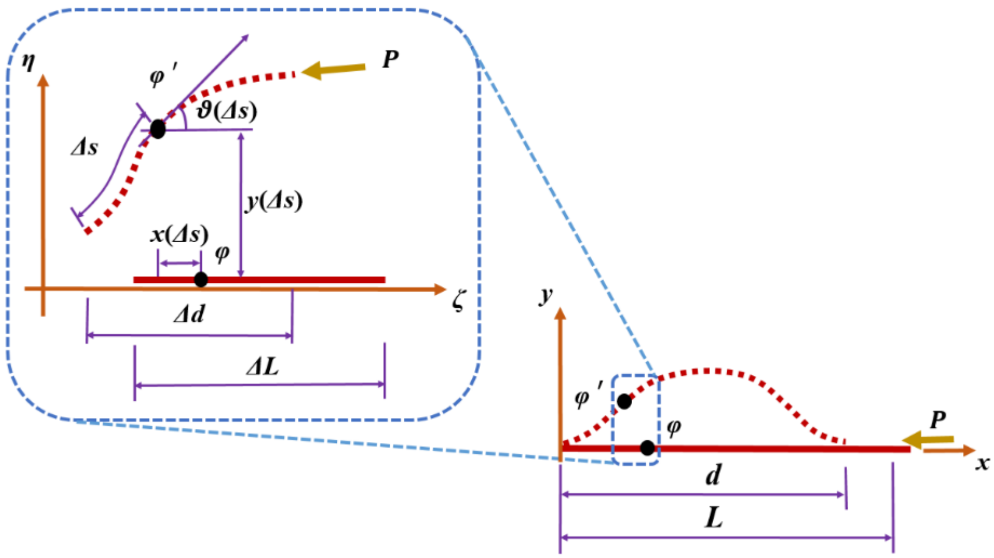

Figure 2-10. Schematic diagram of a deformed beam segment in the large deformation theory.

1999; Shvartsman, 2007; Lee, 2002; Chai, 1991; Chai, 1998; Srivastava and Hui, 2013 A&B; Chen et al., 1996; Solano-Carrillo, 2009; Sofiyev, 2014; Bigoni, 2012; Bosi et al., 2015; Wang, 2009; Katz and Givli, 2015; Chang and Sawamiphakdi, 1982; Doraiswamy et al., 2012; Ram, 2016). Different from the small deformation, the displacement in the longitudinal direction has to be taken into account due to the severe deflection of the beam in the transverse direction. Figure 2-10 displays the diagram of a deformed beam segment for the large deformation model. It can be seen that the location of a random point, φ, on the initially straight beam is changed to φ' under the gradually increased axial force.

In order to investigate the deformation, the segment is considered in a locally curvilinear coordinate $\zeta - \eta$. Since the deformed beam is assumed to be uniform, continuous and inextensible, the segment in the local coordinate can be applied to the entire beam length, namely $\Delta s \in [0 - L]$. Considering the deflected shape configuration of the system, it is found that the maximum deformed rotation angle, α, happens at $s = \frac{L}{4}, \frac{3L}{4}$. Due to the symmetry of the deflected beam configuration, only $\vartheta(s)|_{s=\frac{L}{4}}$ has been taken into account. Bosi et al. (2015) has presented the normalized governing equations of the system as,

$$\frac{d^2\theta(S)}{dS^2} + N^2 \sin[\theta(S)] = 0 \tag{2-32a}$$

$$\begin{cases} Y(0) = Y(1) = 0 \\ \theta(S)|_{S=0} = 0 \\ \left.\dfrac{d\theta(S)}{dS}\right|_{S=\frac{1}{4}} = 0 \end{cases} \tag{2-32b}$$

where $N = \sqrt{\frac{\hat{p}}{EI}}$ represents the normalized axial force placed to the deflected beam.

The non-dimensional factors are given as $S = \frac{s}{L}$, $\theta(S) = \vartheta(SL)$, $X(S) = \frac{x(SL)}{L}$, and $Y(S) = \frac{y(SL)}{h}$. Introducing the Jacobi amplitude function, $\Phi(S)$, a relationship is assumed as,

$$\sin\left[\frac{\theta(S)}{2}\right] = k \sin[\Phi(S)] \tag{2-33}$$

According to Eq. (2-33), the rotation angle, $\theta(S)$, may be written as

$$\theta(S) = 2\arcsin[k \sin[\Phi(S)]] \tag{2-34}$$

where k is defined based on the maximum deformation angle, α. Multiplying Eq. (2-32a) by $\frac{d\theta(S)}{dS}$ and substituting into Eq. (2-34), the rotation angel can be rewritten as

$$\theta(S) = 2\arcsin\big[k\ \mathbf{sn}[4mS\mathbf{K}, k]\big] \tag{2-35}$$

where **sn** denotes the Jacobi sine amplitude function, $m = 1,2,3, \ldots$ refers to the buckling mode of the system, and $\mathbf{K}(k)$ represents the complete elliptic integral function of the first kind at $\Phi = \frac{\pi}{2}$.

The displacements in the longitudinal and transverse directions can be expressed as

$$\begin{cases} X(S) = \int_0^S \cos[\theta(S)]\, dS \\ Y(S) = \int_0^S \sin[\theta(S)]\, dS \end{cases} \tag{2-36}$$

where $s \in [0 - 1]$.

Taking Eq. (2-35) into Eq. (2-36), $X(S)$ and $Y(S)$ can be written as

$$\begin{cases} X(S) = S - \dfrac{1}{2m\,\mathbf{K}}\ \mathbf{E}[\mathbf{am}[4mS\mathbf{K}, k], k] \\ Y(S) = -\dfrac{Lk}{2mh\,\mathbf{K}}\left[1 - \mathbf{cn}[4mS\mathbf{K}, k]\right] \end{cases} \tag{2-37}$$

2.5. Evaluation of the Existing Buckling and Post-buckling Analysis: Past Trends and Future Directions

Buckling and post-buckling may be generally defined as the instabilities of structures. Different types of buckling analyses are developed based on the characteristics of the structures. In recent years, the theoretical studies of buckling and post-buckling are compared and validated with numerical simulations and experiments. In addition, different types of buckling studies are found at multiscale, i.e., plastic, composite materials, dynamic, buckling of cylindrical shells subjected to axial loading, etc.

2.5.1. Trends and Future Directions for Micro/Nanoscale Beams

Micro/nanoscale slender beams are theoretically studied based on the size effect of the materials using material length factor. Many theories are presented to investigate the material length parameter, e.g., Eringen's nonlocal integral elasticity theory. According to the existing studies, material length factor plays a significant role in the static and dynamic response of micro/nanoscale beams. While approaching micro/nanoscale, the nonlocal effect becomes critical. In contrast, the nonlocal effect tends to reduce the critical buckling loads as well as free vibration frequencies, while increasing the static bending and post-buckling deflection.

Since nonlocal elasticity has been developed in recent years, it is generally extensive to apply nonlocal elasticity in the theoretical studies of micro/nanoscale materials. As one of potential research direction, the analysis of tapered nanowires might attract more attention in the future since few studies have proposed to address the problem in this aspect. Note that torsional analysis of nanotubes in the static and dynamic sense might also be a potential research direction in which nonlocal elasticity is a powerful tool. Since carbon nanotubes consists of structural waviness and curvature in fabrication, nonlocal elasticity provides a new horizon to cover the research field. In order to investigate the problem of nanowire buckling, it is of necessity to carry out the static and dynamic analysis of CNTs for better understand the performance of structures at micro/nanoscale. It is also noticed that, comparing with quite a few of theoretical studies, only few experiment has been reported and, therefore, research directions may also be related to experimental investigation of the characteristics of the micro/nanostructures.

2.5.2. Trends and Future Directions for Macroscale Beams

During the last century, the energy method, e.g., Hamilton's principle, has been successfully applied in the analysis of static and dynamic buckling response and stability/instability analysis of slender members, namely beams, shells and plates. In particular, different types of loading and boundary conditions have been investigated. For example, crack, foundation, in-plane force, non-homogeneity, point-support, restrained edges, stepped thickness, viscoelasticity, etc. Different types of such energy method have been developed for different applications over years, e.g., the Rayleigh-Ritz method including DQM-Ritz, Ritz-DQM and Chebyshev Ritz methods. In particular, different shape functions, e.g., a mix of polynomials, orthogonal polynomials, simple polynomials, trigonometric functions, etc., have been used as trial functions in the energy method. Simple polynomials have been extensively applied in most of the studies. It is also found that many studies based on simple polynomials have carried out analysis of numerical instability, i.e., situation that result in diverging instead of converging with the increase in the number of terms in displacement function. The problem of instability is reported to have been overcome by using. Note that the orthogonal polynomials are typically generated by using either a three-term recurrence relation or the Gram-Schmidt process. In addition, the implementation of simple polynomials consists of a generalized eigenvalue problem, whereas that of orthogonal polynomials produces a standard eigenvalue problem. Conducting simple polynomials in the numerical simulations of buckling analysis, the computational cost is recorded relatively low comparing with orthogonal polynomials. In addition, the computation cost is reported to decrease from the boundary conditions of clamped-clamped to free edge. However, limitations and drawbacks are found in the method of polynomials in buckling analysis, especially when the boundary conditions of structures are discontinuous or cracks exist in the structures.

2.6. Summary

Buckling has been considered as critical instability that led to different types of structural failures and, therefore, many studies have been conducted to enhance load-carrying capacity. Recently, research efforts have been switched to exploit the utility of buckling and post-buckling. However, sufficiently harnessing buckling performance of slender members is an in progressing field that has yet been fully explored. In order to effectively identify buckling and post-buckling response, different mechanisms have been developed in micro/nanoscale and macroscale. This topical review summarized the development of theoretical models on multiscale buckling and post-buckling analysis. The following findings can be drawn from the presented review:

- A severe size dependency has been captured in micro/nanoscale buckling analysis. Many theories have been carried out to take into account size effects on buckling response, i.e., nonlocal elasticity theory, non-classical couple stress elasticity theory, and strain gradient elasticity theory. In order to obtain post-buckling response, mechanisms are of necessity to investigate the systems that contain different types of elements rather than only beam/plate, namely shell or pre-deformed elements, or certain lateral constraints along element surface. However, lack of studies have been conducted regarding post-buckling identification in micro/nanoscale.
- In macroscale buckling and post-buckling analysis, studies are carried out using small deformation or large deformation theory with respect to the deformation of buckled elements. Many factors are developed to indicate the applicability of the theories, e.g., slenderness ratio or the ratio of deflection and element length. Based on small deformation theory, many theoretical studies have taken into account deflections in the phases of

buckling and post-buckling by deploying constraints, but inadequate efforts are found in large deformation theory.

CHAPTER 3

POST-BUCKLING RESPONSE OF NON-UNIFORM BEAMS USING SMALL DEFORMATION THEORY

3.1. Overview

Using small deformation assumptions, an energy-based theoretical model has been developed (Borchani et al., 2014; Borchani et al., 2015). The model accurately predicts the post-buckling response of bilaterally constrained uniform cross-section beams subjected to gradually increasing axial forces. However, uniform beams do not permit to adequately control the post-buckling behavior and, hence, optimize the energy conversion efficiency of the system. A recent study has showed that the controlling of the spacing between the snap-through transitions is possible using non-uniform cross section beams (Jiao et al., 2016). This chapter aims to maximize the harvested electric power using non-prismatic beams. In Chapter III, a theoretical model is presented to capture and control the static and dynamic post-buckling events of non-uniform cross-section beams. The model presented in this chapter allows for accurate prediction of the deflected shapes and post-buckling mode transitions of non-uniform beams under quasi-static axial forces. The theoretical results are then experimentally validated. The main outcome is to design non-prismatic beams that allow the control of both spacing between transition events and location of the snap-through point. A comparison between the generated output powers shows that non-prismatic beams present a great advantage over prismatic beams.

3.1.1. Operational Principle

Mechanical energy concentrators and triggers have been introduced as a solution to harvest energy and sense quasi-static events (Lajnef et al., 2014; Lajnef et al., 2012; Lajnef et al., 2015). These mechanisms consist of a slender beam that is bilaterally constrained by two rigid walls and subjected to an axial loading. The proposed concept is shown in Figure 1-1 packaged into a device for embedment or attachment to structural components. Under quasi-static structural deformations (e.g., due to service deformations, temperature fluctuations, or slow degradation in material properties), the device capsule is compressed (or tensioned), inducing variations in axial deformations to the enclosed beam elements. Due to the presence of bilateral constraints, the variation of the axial forces induces multiple sudden and high-rate buckling snap-through transitions. The compressed element stores accumulated strain energy, then suddenly releases it as kinetic energy when the axial compressive force reaches a critical buckling load threshold. Using a piezoelectric energy scavenger, attached to the buckled element in a cantilevered configuration, these high-rate motions are converted into electric energy that can be stored or used to power wireless sensors.

A typical force-displacement response of a bilaterally constrained beam is displayed in Figure 3-1. The presented beam’s behavior has been experimentally determined under displacement-controlled axial loadings (Lajnef et al., 2012). The post-buckling snap-through transitions can be seen by the load drops in the force–deformation response. The figure labels ($\Phi3$; $\Phi5$, etc.) indicate the buckling mode shape to which the column transitions after the snap-through event. Each of the mode transitions represents the switch between a stable equilibrium branch and another that reduces the total potential energy in the system. The beam was loaded past its seventh buckled mode ($\Phi7$) and then unloaded. Successive transitions to lower buckling modes were also observed during the unloading phase. However, the forces, and consequently displacements, at which step-down transitions occur, are much lower than those of inverse transitions during the loading phase. Furthermore, the beam returns to lower buckling modes through a different equilibrium path during unloading. The hysteretic nature of the response is due to the friction between the strip and the walls and the existence of multiple equilibrium configurations.

The snap-through transitions between equilibrium positions induces a high-rate input acceleration to the attached energy harvesting oscillator. Figure 3-2 displays the energy harvester's response under a full loading cycle past the beam's seventh buckling mode. The first voltage oscillation is caused by the first contact between the strip and the rigid constraints, corresponding to the first buckling mode. The other successive voltage output events are generated by the beam's snap-through transitions between buckling modes.

As mentioned above, the device capsule can either be compressed or tensioned depending on the response of the structure. In order to harvest energy from both cases, the device can be pre-compressed into one of its buckled configurations and then embedded within the structure. Therefore, the buckled slender beam transitions into a higher or a lower buckling configuration depending on the direction of its axial load. Figure 3-3 displays the piezoelectric voltage output under an alternating axial load. The constrained beam was preloaded past its fifth buckling mode ($\Phi 5$). Loading cycles were then applied between a maximum load past the seventh mode ($\Phi 7$) equilibrium position and a minimum load below the third stable configuration ($\Phi 3$). In the figure, the labels $\Phi 3$ to $\Phi 7$ indicate the positions of mode transitions. This figure clearly shows that the system can be initially centered (positioned) so as to harvest energy from compressive as well as from tensile input global loading deformations. The levels of the applied forces can be controlled by tuning the geometry and material properties of the beam.

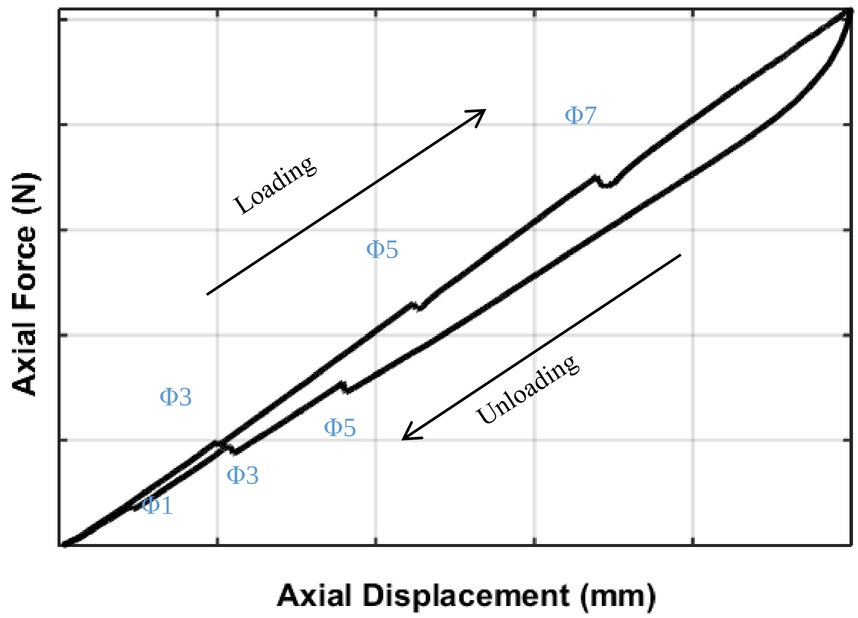

Figure 3-1. Experimental force-displacement response of a bilaterally constrained beam.

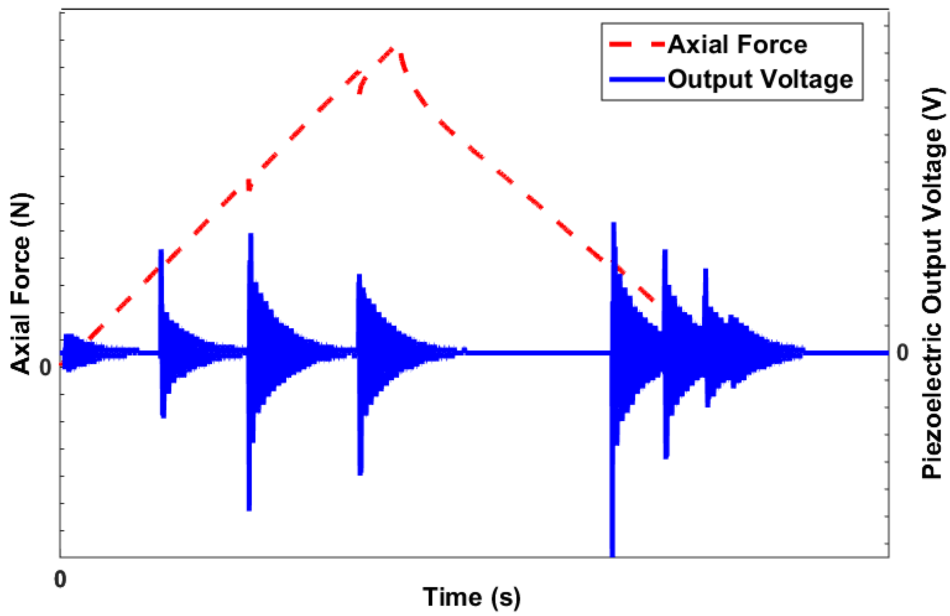

Figure 3-2. Piezoelectric output voltage response under a full load cycle.

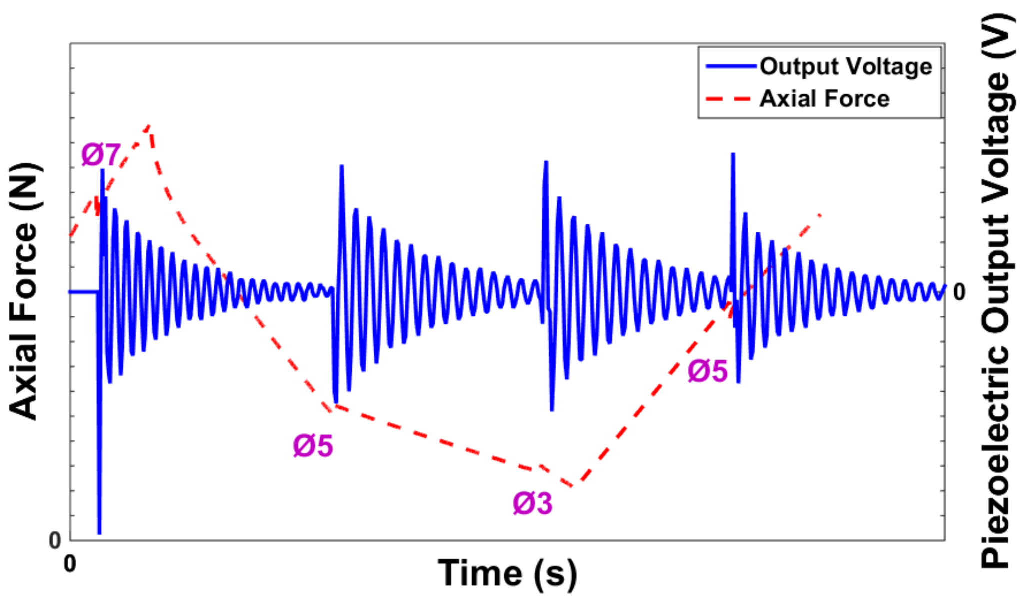

Figure 3-3. Piezoelectric output voltage response under a full load cycle.

3.1.2. Design Optimality

Figure 3-4 presents a flowchart that details the design optimality criteria. The energy harvesting cell shown in Figure 3-4(a) consists of a clamped-clamped homogeneous non-prismatic beam that is bilaterally constrained by fixed rigid walls. A piezoelectric vibrator is attached to the beam in a cantilever configuration. Under external quasi-statically-increasing axial forces, the beam deflects in the first buckling mode until it touches one of the lateral constraints. As the axial force increases, the lateral boundary exerts lateral forces on the beam forcing it to jump into higher buckling modes, i.e. Φ3, as shown in Figure 3-4(a). The snap-through transition of the beam transforms the quasi-static global axial deformation into a localized high acceleration motion. The attached piezoelectric harvester converts the local kinetic energy into electric power.

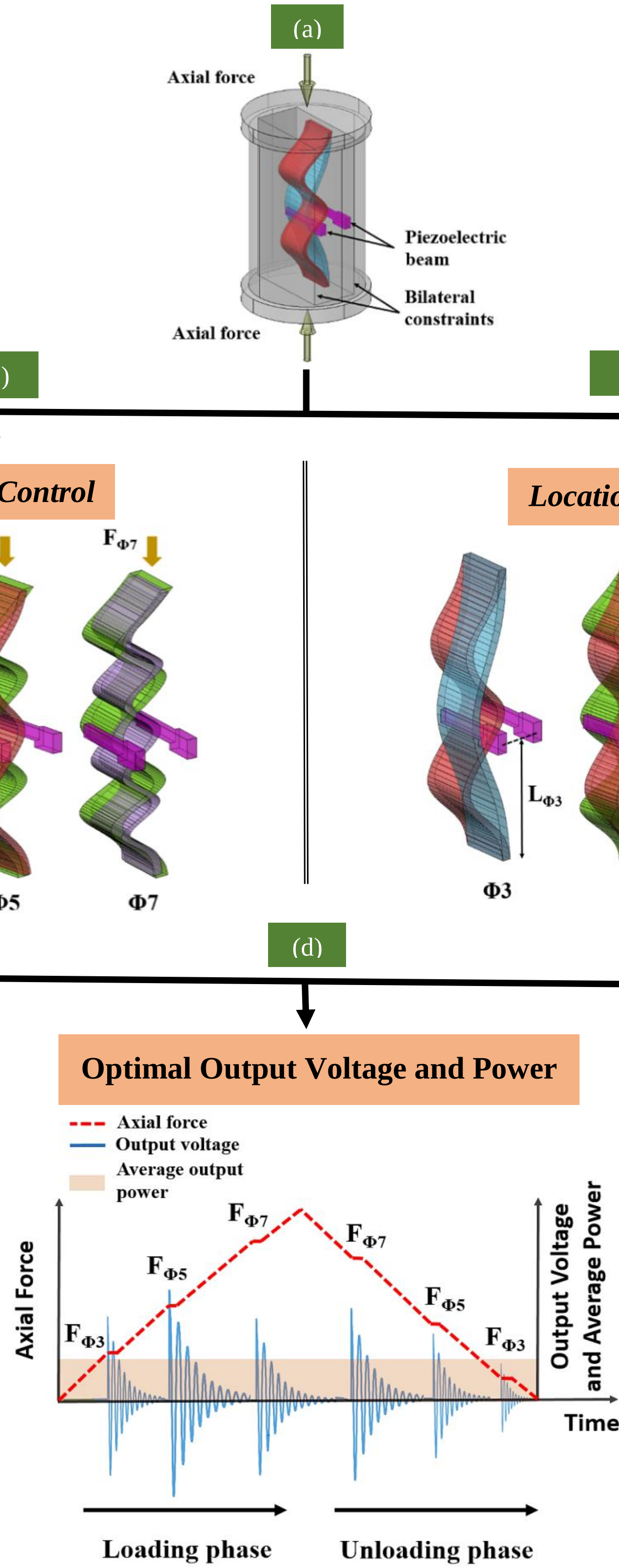

Figure 3-4. Schematic of the optimal design.

In order to maximize the piezoelectric output energy and reduce the electronic power leakage due to circuit biasing, two important parameters have to be controlled. These parameters are the spacing between the snap-through transitions and the location of the snapping point. An optimal spacing between the snap-through events is defined such that a transition occurs as soon as the voltage generated by the previous transition drops below a certain threshold (as shown in Figure 3-4(d)). This threshold corresponds to the voltage required to bias the electronic circuits. While, the snap-throughs have to occur at the same location that corresponds to the base of the piezoelectric harvester. Therefore the energy converter harvests the maximum kinetic energy released during transitions. This study aims to control the location and spacing between snap-through transitions, as shown in Figure 3-4(b) and (c). The spacing is represented by the ratio between the forces at which transitions occur. The spacing ratio is expressed as,

$$R = \frac{\mathrm{F}_{\Phi 7} - \mathrm{F}_{\Phi 5}}{\mathrm{F}_{\Phi 5} - \mathrm{F}_{\Phi 3}} \tag{3-1}$$

The snap-through location refers to the point that travels the largest distance during buckling mode transitions. A parameter *D* that represents the difference between the transition locations is introduced as,

$$D = |L_{\Phi 7} - L_{\Phi 5}| + |L_{\Phi 5} - L_{\Phi 3}| + |L_{\Phi 3} - L_{\Phi 7}| \tag{3-2}$$

where $L_{\Phi i}$ (i = 3, 5 and 7) denote the location of the snapping point during the transition to mode i. By eliminating *D*, all the locations of the snap-through transitions are guaranteed to coincide. The objective is to coincide these points at all transitions. Therefore, installing the piezoelectric harvester at that location would maximize the harvested output energy. Based on the proposed design, Figure 3-4(d) conceptually displays the optimal output voltage, and average power with respect to the applied axial force. By optimizing the device, the snap-through events can be induced at specific axial forces, while the output voltage and the average output power are maximized. Different geometry configurations and dimensions are investigated. For each geometry, the response of the beam is determined by numerically minimizing the potential energy of the system. The solutions to the minimization problem are the coefficients Ai (i=1..∞) that determine the transverse and axial deflections of the beam under an axial load. The transitions are witnessed by a jump or discontinuity in the force-displacement response. The location of the snap-through is determined by comparing between the deflected shapes before and after each transition. The spacing ratio between snap-through transitions is computed using Eq. (3-1). The geometry configuration of the beam is changed until achieving the desired spacing ratio. Then the dimensions are tuned to coincide snap-through locations.

3.2. Theoretical Analysis of Non-Uniform Cross-Section Beams

3.2.1. Theoretical Model Based on an Summation Algorithm

3.2.1.1. Post-Buckling Analysis

The problem under consideration consists of a slender non-prismatic beam that is placed between two frictionless bilateral constraints and subjected to an axial loading. As shown in Figure 3-5, the beam's thickness t(x), width $b(x)$, cross section area $A(x)$and moment of inertia $I(x)$ are considered non-constant and vary with respect to the longitudinal abscissa x. The Young's modulus E, beam's length L and gap separating the bilateral constraints h_0 are assumed constants. The net gap between the beam and the lateral constraint is defined as $h(x) = h_0 - t(x)$. The transverse deflection of the beam and the applied axial force are denoted by $\hat{w}(x)$ and

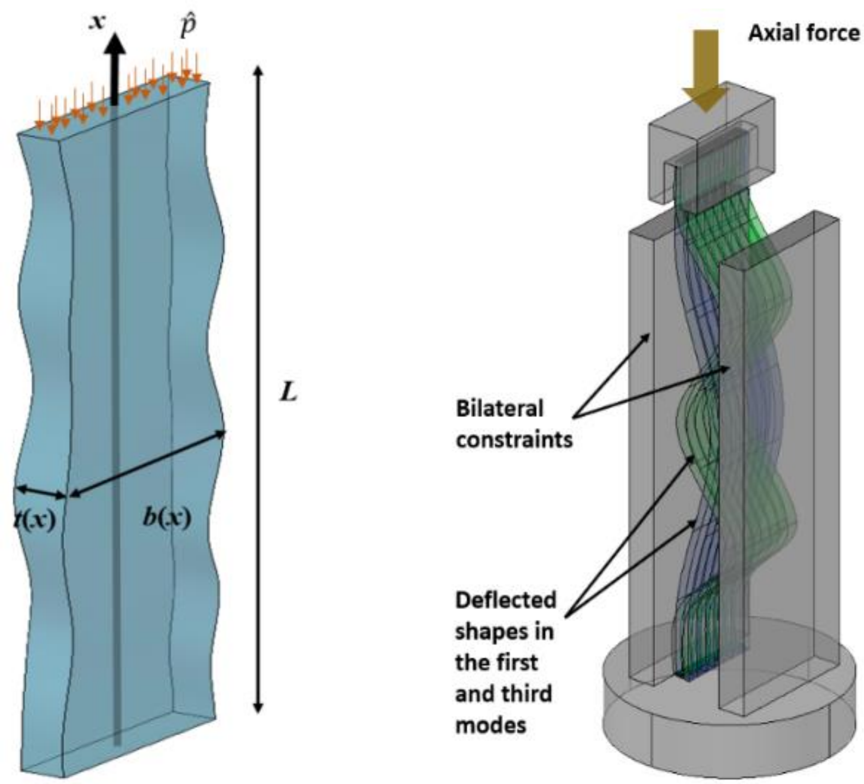

(a) (b)

Figure 3-5. (a) Schematic of a beam with random geometry properties, and (b) examples of its buckled configurations in the first and third modes.

$\hat{p}$, respectively. Nonlinear Euler-Bernoulli beam theory is used under small deformation assumptions to model the beam. The governing equation of the beam's buckling can be written as,

$$EI(x)\frac{d^4\widehat{w}(x)}{dx^4}+\left[\hat{p}-\frac{1}{2L}\int_0^L EA(x)\left(\frac{d\widehat{w}(x)}{dx}\right)^2\,dx\right]\frac{d^2\widehat{w}(x)}{dx^2}=0 \tag{3-3}$$

The boundary conditions of Eq. (3-3) are given by

$$\hat{w}(0) = \hat{w}(L) = 0$$
$$\left.\frac{d\hat{w}(x)}{dx}\right|_{x=0} = \left.\frac{d\hat{w}(x)}{dx}\right|_{x=L} = 0 \tag{3-4}$$

Eqs. (3-3) and (3-4) can be expressed in non-dimensional forms as,

$$\frac{d^4W(X)}{dX^4} + N^2\frac{d^2W(X)}{dX^2} = 0 \tag{3-5}$$

$$W(0) = W(1) = 0 \quad and \quad \left.\frac{dW(X)}{dX}\right|_{X=0} = \left.\frac{dW(X)}{dX}\right|_{X=1} = 0 \tag{3-6}$$

where the non-dimensional variables are defined as,

$$X = \frac{x}{L}, \qquad W(X) = \frac{\hat{w}(X\,L)}{h(XL)} \quad \text{and} \quad N^2 = \frac{\hat{p}L^2}{EI(XL)} - \frac{h(XL)^2 A(XL)}{2\,I(XL)}\int_0^1 \left(\frac{dW}{dX}\right)^2 dX \tag{3-7}$$

The symmetric and antisymmetric mode shapes of the general solution to Eq. (3-5) and Eq. (3-6) can be expressed, respectively, as,

$$\begin{gathered} W^s(X) = 1 - cos(N_i X) \\ N_i = (i+1)\pi \end{gathered}, \qquad (i = 1, 3, \dots) \tag{3-8}$$

and

$$\begin{gathered} W^a(X) = 1 - 2X - cos\left(N_j X\right) + \frac{2sin\left(N_j X\right)}{N_j} \\ N_j = 2.86\pi, 4.92\pi, 6.94\pi, 8.95\pi, \dots \end{gathered}, \qquad (j = 2, 4, \dots) \tag{3-9}$$

N_i and N_j in Eqs. (3-8) and (3-9) refer to the eigenvalues of the symmetric and antisymmetric modes, which are determined by solving the equations $sin(N_i/2) = 0$ and $tan(N_j/2) = N_j/2$, respectively.

Since the buckling modes, described in Eqs. (3-8) and (3-9), generate an orthogonal basis, a superposition method can be used to express the deflection of the beam as a linear combination of the buckling modes as,

$$W(X) = \sum_{i=1,3,5,\dots}^{\infty} C_i\, W_i^s(X) + \sum_{j=2,4,6,\dots}^{\infty} C_j\, W_j^a(X) \tag{3-10}$$

where $C_i(i = 1..\infty)$ are weight coefficients that determine the contribution of each buckling mode to the transverse deflection of the beam.

3.2.1.2. Energy Analysis

In this study, an energy method is applied to analyze the post-buckling response of a beam with random geometry properties under axial loadings. Since the bilateral constraints are assumed frictionless, the total energy (**Ω**) of the dynamic system at any equilibrium state consists of two components, i.e., the total potential energy (**Π**) and kinetic energy (**K**). The total potential energy of the deflected beam consists of three components: bending energy u_b, compressive strain energy u_c and work of external force u_p . These energies can be written, in terms of the axial force $\hat{p}$, as,

$$u_b = \frac{1}{2} E \int_0^L I(x) \left[\frac{d^2\widehat{w}(x)}{dx^2}\right]^2 dx \tag{3-11a}$$

$$u_c = \frac{1}{2} S \varDelta_c \tag{3-11b}$$

$$u_p = \frac{1}{2} \hat{p} \varDelta \tag{3-11c}$$

where $S,$ $\varDelta_c$ and $\varDelta$ refer to the axial compressive force, axial compressive deformation and overall variation of the beam's length, respectively. They can be related to the applied force $\hat{p}$ and beam's deflection $\widehat{w}(x)$ by,

$$S = \hat{p} \tag{3-12a}$$

$$\varDelta_c = \frac{\hat{p}}{E} \int_0^L \frac{1}{b(x)t(x)} dx \tag{3-12b}$$

$$\varDelta = \varDelta_c + \frac{1}{2} \int_0^L \left[\frac{d\widehat{w}(x)}{dx} \right]^2 dx \tag{3-12c}$$

Substituting Eq. (3-12) into Eq. (3-11), the total potential energy can be calculated as,

$$\begin{aligned} \mathbf{\Pi} &= u_b + u_c - u_p \\ &= \frac{1}{2} E \int_0^L I(x) \left[\frac{d^2 \widehat{w}(x)}{dx^2} \right]^2 dx - \frac{1}{4} \hat{p} \int_0^L \left[\frac{d\widehat{w}(x)}{dx} \right]^2 dx \end{aligned} \tag{3-13}$$

Substituting Eq. (3-7) into Eq. (3-13) yields,

$$\mathbf{\Pi} = \frac{EL}{24}\int_0^1 h(X)^2 b(X) t(X)^3 \left[\frac{d^2W(X)}{dX^2}\right]^2 dX - \frac{\hat{p}}{4L}\int_0^1 h(X)^2 \left[\frac{dW(X)}{dX}\right]^2 dX \tag{3-14}$$

Taking Eq. (3-10) into Eq. (3-14), the total potential energy of the system is obtained as,

$$\begin{aligned}\mathbf{\Pi} = {} & \frac{EL}{24}\int_0^1 h^2 b\, t^3 \left[\sum_{i=1,3,5,\ldots}^{\infty}\left(C_i\,\frac{d^2W_i^s}{dX^2}\right) + \sum_{j=2,4,6,\ldots}^{\infty}\left(C_j\,\frac{d^2W_j^a}{dX^2}\right)\right]^2 dX \\ & - \frac{\hat{p}}{4L}\int_0^1 h^2 \left[\sum_{i=1,3,5,\ldots}^{\infty}\left(C_i\,\frac{dW_i^s}{dX}\right) + \sum_{j=2,4,6,\ldots}^{\infty}\left(C_j\,\frac{dW_j^a}{dX}\right)\right]^2 dX\end{aligned} \tag{3-15}$$

The kinetic energy of the beam can be expressed as (Asghari et al., 2012),

$$\mathbf{K} = \frac{1}{2}\int_0^L \int_A \rho \left[\left(\frac{\partial \hat{u}}{\partial t} - z\frac{\partial^2 \widehat{w}}{\partial t \partial x}\right)^2 + \left(\frac{\partial \widehat{w}}{\partial t}\right)^2\right] dA\, dx \tag{3-16}$$

which can be rewritten as,

$$\begin{aligned}\mathbf{K} = \frac{\rho}{2}\int_0^L \Bigg[& \underbrace{A(x)\left(\frac{\partial \hat{u}}{\partial t}\right)^2}_{\text{Axial kinetic energy}} + \underbrace{\int_A \left[z^2\left(\frac{\partial^2 \widehat{w}}{\partial t \partial x}\right)^2 - 2z\frac{\partial \hat{u}\,\partial^2 \widehat{w}}{\partial t^2 \partial x}\right] dA}_{\text{Rotational kinetic energy}} \\ & + \underbrace{A(x)\left(\frac{\partial \widehat{w}}{\partial t}\right)^2}_{\text{Transverse kinetic energy}}\Bigg] dx\end{aligned} \tag{3-17}$$

where ρ refers to the constant mass density of the homogeneous beam. Eq. (3-17) consists of three components, including the kinetic energies due to axial, rotational and transverse inertias. Since the axial force is quasi-static and small deformations and rotations are assumed, both axial and rotational kinetic energies are neglected. Therefore, using the normalization factors defined in Eq. (3-7), the kinetic energy is simplified as,

$$\mathbf{K} = \frac{\rho L^3}{2} \int_0^1 A(X) h(X)^2 \left(\frac{\partial W(X,t)}{\partial t} \right)^2 dX \tag{3-18}$$

Using the Galerkin discretization method to separate time and space coordinates, the transverse displacement can be written as a linear combination of the admissible functions multiplied by unknown temporal coordinate,

$$W(X,t) = \sum_{k=1}^{\infty} \alpha_k(t)\, W_k(X) \tag{3-19}$$

where $\alpha_k(t)$ is defined as the generalized temporal coordinate and $W_k(X)$ are the buckling modes. Taking Eqs. (3-10) and (3-19) into (3-18), the kinetic energy is expressed as,

$$\mathbf{K} = \frac{\rho L^3}{2} \int_0^1 A(x) h(X)^2 \left[\sum_{k=1}^{\infty} \frac{d\alpha_k(t)}{dt} \left(\sum_{i=1,3,5,\ldots}^{\infty} C_i\, W_i^s(X) + \sum_{j=2,4,6,\ldots}^{\infty} C_j\, W_j^a(X) \right) \right]^2 dX \tag{3-20}$$

According to Eqs. (3-15) and (3-20), the total energy of the system is given by,

$$\boldsymbol{\Omega} = \boldsymbol{\Pi} + \mathbf{K} = \frac{EL}{24}\int_0^1 h^2 b\, t^3 \left[\sum_{i=1,3,5,\dots}^{\infty}\left(C_i\,\frac{d^2W_i^s}{dX^2}\right) + \sum_{j=2,4,6,\dots}^{\infty}\left(C_j\,\frac{d^2W_j^a}{dX^2}\right)\right]^2 dX$$

$$- \frac{\hat{p}}{4L}\int_0^1 h^2 \left[\sum_{i=1,3,5,\dots}^{\infty}\left(C_i\,\frac{dW_i^s}{dX}\right) + \sum_{j=2,4,6,\dots}^{\infty}\left(C_j\,\frac{dW_j^a}{dX}\right)\right]^2 dX$$

$$+ \frac{\rho L^3}{2}\int_0^1 Ah^2 \left[\sum_{k=1}^{\infty}\frac{d\alpha_k(t)}{dt}\left(\sum_{i=1,3,5,\dots}^{\infty} C_i\,W_i^s(X) \right.\right. \tag{3-21}$$

$$\left.\left. + \sum_{j=2,4,6,\dots}^{\infty} C_j\,W_j^a(X)\right)\right]^2 dX$$

The unknown coefficients C_i in Eq. (3-21) can be determined by solving the following constrained minimization problem,

$$\begin{cases} \text{Min}\ \boldsymbol{\Omega}(C_i) \\ 0 \le W(X) \le 1 \end{cases} \tag{3-22}$$

In Eq. (3-22), the unknown coefficients are determined by minimizing the total potential energy of the system within the bilateral constraints. Due to the nonlinearity of the objective function, Eq. (3-22) is numerically solved using Nelder–Mead algorithm (Jiao et al., 2016). Even though Nelder–Mead is not a true global optimization, it works reasonably well in our case as the system does not contain many local energy minima. The model is used to investigate the dynamic post-buckling response of a notched beam under a cyclic load. The loading protocol follows the following function,

$$\hat{p} = \begin{cases} \hat{p}_{max} \dfrac{2t}{T} & t = \left[0, \dfrac{T}{2}\right] \\ \hat{p}_{max} \left(2 - \dfrac{2t}{T}\right) & t = \left[\dfrac{T}{2}, T\right] \end{cases} \tag{3-23}$$

where $\hat{p}_{max}$ and T constitutes the loading amplitude and period, respectively. The geometry of the beam and loading parameters are detailed in Table 3-1. Figure 3-6 displays the theoretically simulated dynamic response of the beam. As can be seen, the dynamic model is able to detect the coexistence of multiple equilibrium configurations and difference between loading and unloading equilibrium paths. However, due to non-consideration of friction the hysteretic behavior is missed and the transition forces during unloading are overestimated. Friction will be considered in future studies to improve the modeling of the unloading branch. However, the loading phase can be accurately described using the current static model. The static model can be obtained by dropping the kinetic energy term and minimizing the potential energy instead of the total energy. The location of the snap-through transitions depends only on the geometry of the beam. Therefore, maximization of the levels of the harvested energy under monotonic axial load applies to dynamic loadings as well.

Table 3-1. Geometry properties of the notched specimen.

	Top	Notch	Bottom
Length (mm)	112.5	25	112.5
Width (mm)	30	14	30
Thickness (mm)	2.34	2.34	2.34
Loading Period (s)		10	
Maximum Load (N)		3000	

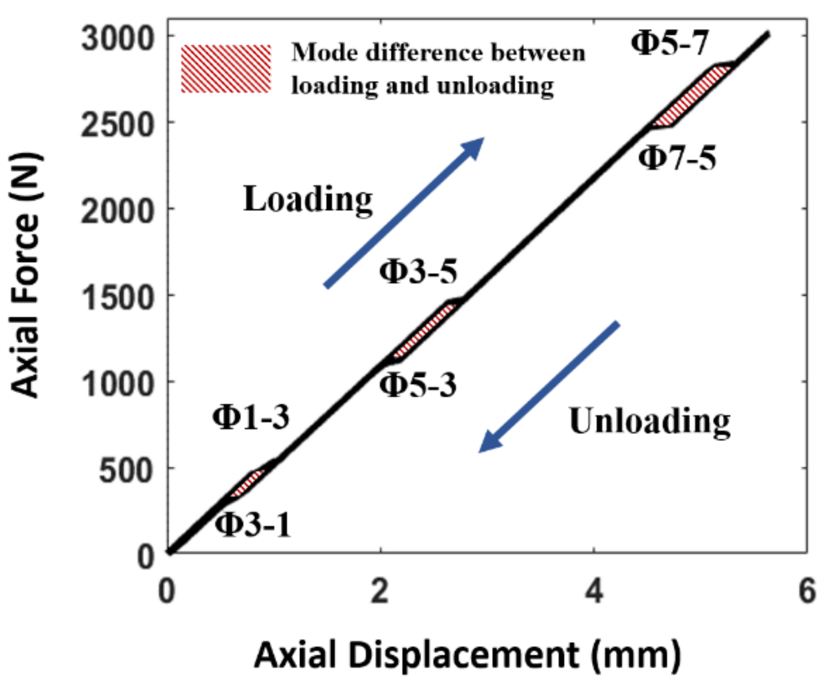

Figure 3-6. Dynamic force-displacement response under a cyclic load.

3.2.2. A Close-Form Theoretical Model

3.2.2.1. Post-Buckling Analysis

According to the studies presented in (Li et al., 1994; 2001), the static equation that governs the governing equation presented in Eq. (3-3) is reduced to,

$$\frac{d^2M(X)}{dX^2} + \frac{P}{EI(X)}\ M(X) = 0 \tag{3-24}$$

where $P = \hat{p}L^2$ is constant. The general solution of Eq. (3-24) may be expressed as,

$$M(X) = C_1\Omega_1(X) + C_2\Omega_2(X) \tag{3-25}$$

where $\Omega_i(X)$ and $C_i,\ (i = 1{,}2)$ are linearly independent special solutions and integral constants of Eq. (3-24), respectively. The solutions $\Omega_i(X)$ depend on the distribution of the flexural stiffness function $EI(x)$. Therefore, the general solution for different beam shape configurations can be obtained by integrating Eq. (3-25) as,

$$\frac{dW(X)}{dX} = C_1\int \Omega_1(X)\ dX + C_2\int \Omega_2(X)\ dX + C_3 \tag{3-26a}$$

$$W(X) = C_1\int\int \Omega_1(X)\ dX\ \ dX + C_2\int\int \Omega_2(X)\ dX\ \ dX + C_3X + C_4 \tag{3-26b}$$

Since different beam shape configurations lead to different independent special solutions, the cases presented in Figure 3-7 are categorized into four investigated groups, namely, piecewise constant, linear width, linear thickness, and radical width.

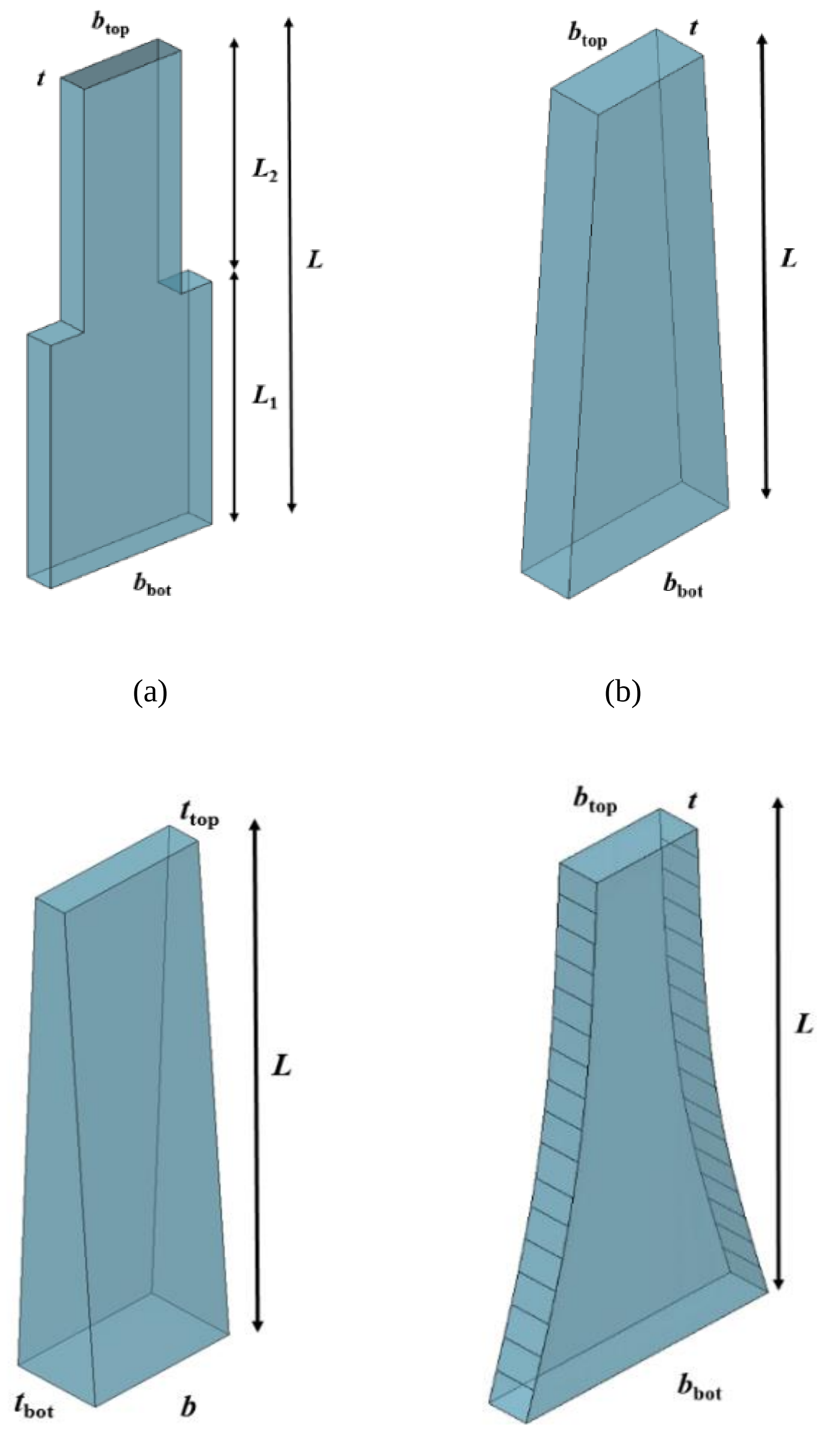

(a) (b)

(c) (d)

Figure 3-7. Studied beam shape configurations: (a) piecewise constant width, (b) linear width, (c) linear thickness, and (d) radical width.

This section focuses on the T-beam shape configuration that consists of two uniform segments, presented in Figure 3-7(a). Note that for multiple uniform segments, same procedure can be followed to obtain shape functions. The independent solutions, presented in Eq. (3-25), of the k^{th} segment $(k = 1, 2)$ can be expressed as in Li et al. (1994) as,

$$\begin{cases} \Omega_{k1}(X) = \sin(n_k X) \\ \Omega_{k2}(X) = \cos(n_k X) \\ \quad n_k = \sqrt{\dfrac{P}{EI_k}} \end{cases} \tag{3-27}$$

Substituting Eq. (3-27) into Eq. (3-26), the rotation and deflection functions of each segment are obtained as,

$$\frac{dW_k{}^{PWC}(X)}{dX} = -C_{k1}\frac{\cos(n_k X)}{n_k} + C_{k2}\frac{\sin(n_k X)}{n_k} + C_3 \tag{3-28a}$$

$$W_k{}^{PWC}(X) = -C_{k1}\frac{\sin(n_k X)}{n_k{}^2} - C_{k2}\frac{\cos(n_k X)}{n_k{}^2} + C_3 X + C_4 \tag{3-28b}$$

where C_{ki} $(k = 1, 2$ & $i = 1, 2)$, C_3, and C_4 are the integration constants that can be determined using boundary conditions. Substituting Eq. (3-28) into Eq. (3-6) and taking into account the continuity of the beam's rotation and deflection at the joint between the two segments $(X = L_1/L)$, a total of six algebraic equations are obtained as,

$$-C_{12}\frac{1}{n_1{}^2} + C_4 = 0 \tag{3-29a}$$

$$-C_{11}\frac{1}{n_1}+C_3=0 \tag{3-29b}$$

$$-C_{21}\frac{\sin(n_2)}{{n_2}^2}-C_{22}\frac{\cos(n_2)}{{n_2}^2}+C_3+C_4=0 \tag{3-29c}$$

$$-C_{21}\frac{\cos(n_2)}{n_2}+C_{22}\frac{\sin(n_2)}{n_2}+C_3=0 \tag{3-29d}$$

$$\begin{aligned}&\frac{C_{11}}{{n_1}^2}\sin\left(\frac{n_1L_1}{L}\right)+\frac{C_{12}}{{n_1}^2}\cos\left(\frac{n_1L_1}{L}\right)\\&-\frac{C_{21}}{{n_2}^2}\sin\left(\frac{n_2L_1}{L}\right)-\frac{C_{22}}{{n_2}^2}\cos\left(\frac{n_2L_1}{L}\right)=0\end{aligned} \tag{3-29e}$$

$$\begin{aligned}&-\frac{C_{11}}{n_1}\cos\left(\frac{n_1L_1}{L}\right)+\frac{C_{12}}{n_1}\sin\left(\frac{n_1L_1}{L}\right)\\&+\frac{C_{21}}{n_2}\cos\left(\frac{n_2L_1}{L}\right)-\frac{C_{22}}{n_2}\sin\left(\frac{n_2L_1}{L}\right)=0\end{aligned} \tag{3-29f}$$

Using Eq. (3-29), the integration constants can be expressed in terms of C_4, and then substituted into Eq. (3-28b) to obtain the corresponding shape function, $\psi_i(X)$ $(i=1,2)$. Eq. (3-29) represents an eigenvalue problem for n_i $(i=1,2)$. The characteristic equation for n_i can be written as,

$$\frac{1}{{n_1}^4{n_2}^4}(2n_1n_2 + \sin(n_2)\sin(\Gamma)\,[({n_1}^2 + {n_2}^2)$$
$$\times \cos(\Lambda) - {n_1}^2 n_2 \sin(\Lambda)] - \cos(n_2)\sin(\Gamma)$$
$$\times [{n_1}^2 n_2 \cos(\Lambda) + ({n_1}^2 + {n_2}^2)\sin(\Lambda)]$$
$$- n_1 n_2 \cos(\Gamma)\,[2\cos(n_2 - \Lambda)$$
$$+ n_2 \sin(n_2 - \Lambda)]) = 0 \tag{3-30}$$

where $\Gamma = n_1 L_1/L$ and $\Lambda = n_2 L_1/L$. Taking into account the geometry of the piecewise constant beam, two geometry parameters can be introduced: $\mu = \frac{b_{top}}{b_{bot}}$ $(0 < \mu \leq 1)$ and $v = \frac{L_1}{L}$ $(0 < v \leq 1)$. Based on Eq. (3-27), the eigenvalues n_1 and n_2 can be related by ${n_2}^2 = \frac{{n_1}^2}{\mu}$. Therefore, the eigenvalues n_1 can be computed by numerically solving Eq. (3-30) and then used to determine n_2. For instance, if $\mu = \frac{1}{2}$ and $v = \frac{1}{2}$, then $n_2 = \sqrt{2}n_1$ and the first four eigenvalues of n_1 are solved as 5.08, 7.587, 10.285, and 12.865. The general form of the buckling shape function is then obtained as,

$$\psi_i(X)^{PWC} = \begin{cases} {\psi_i}^{\mathrm{I}}(X)^{PWC} & if\ \ 0 \leq X \leq \dfrac{1}{2} \\ {\psi_i}^{\mathrm{II}}(X)^{PWC} & if\ \ \dfrac{1}{2} \leq X \leq 1 \end{cases} \tag{3-31}$$

where

$$\psi_i^{\mathrm{I}}(X)^{PWC} = 1 - \cos(n_i X) + \frac{n_i \sin\left(\frac{1}{2} n_i\right) + \sqrt{2} n_i \cos\left(\frac{\sqrt{2}}{2} n_i\right)}{\cos\left(\frac{\sqrt{2}}{2} n_i\right) + \sqrt{2} n_i \sin\left(\frac{\sqrt{2}}{2} n_i\right) - \cos\left(\frac{n_i}{2}\right)} \left[\frac{\sin(n_i X)}{n_i} - X\right] \tag{3-32a}$$

$$\psi_i^{\mathrm{II}}(X)^{PWC} = 1 + \frac{1}{\cos\left(\frac{\sqrt{2}}{2} n_i\right) + \sqrt{2} n_i \sin\left(\frac{\sqrt{2}}{2} n_i\right) - \cos\left(\frac{n_i}{2}\right)} \left[\cos\left(\frac{n_i}{2}\right) \cos\left[\sqrt{2} n_i (1 - X)\right] - \cos\left[\sqrt{2} n_i \left(X - \frac{1}{2}\right)\right] - \frac{\sqrt{2}}{2} \sin\left(\frac{n_i}{2}\right) \sin\left[\sqrt{2} n_i (1 - X)\right] - \sqrt{2} n_i \sin\left(\frac{\sqrt{2}}{2} n_i\right) X + n_i \sin\left(\frac{n_i}{2}\right) \left[\cos\left[\sqrt{2} n_i (1 - X)\right] - X\right]\right] \tag{3-32b}$$

The linear function of the beam width in Figure 3-7(b) is given by,

$$b(X) = b_{top} + \left(b_{bot} - b_{top}\right) X \tag{3-33}$$

The flexural stiffness function $EI(X)$ can be written in the form,

$$EI(X) = \alpha(1 + \beta X)^{\xi} \tag{3-34}$$

where the quantities α, β and ξ are defined as,

$$\alpha = \frac{Eb_{bot}t^3}{12}, \qquad \beta = \frac{b_{bot}}{b_{top}} - 1, \quad \text{and} \quad \xi = 1 \tag{3-35}$$

The linearly independent special solutions that constitute the general solution $M(X)^{LnrW}$ presented in Eq. (3-25) are as in Li et al. (1994) ($k_i = \frac{1}{2}$ and $\nu_i = 1$) as,

$$\begin{cases} \Omega_1(X) = \sqrt{1+\beta X} \ \ \mathbf{J}_1[\Phi^{LnrW}] \\ \Omega_2(X) = \sqrt{1+\beta X} \ \mathbf{Y}_1[\Phi^{LnrW}] \\ \Phi^{LnrW} = 2n(1+\beta X)^{\frac{1}{2}} \\ n = \sqrt{\dfrac{P}{\alpha\beta^2}} \end{cases} \tag{3-36}$$

where **J** and **Y** refer to the Bessel function of the first and second kinds. Substituting Eq. (3-36) into Eq. (3-26), the general deflection functions of the linear width beam can be obtained as,

$$\frac{dW(X)^{LnrW}}{dX} = C_1 \frac{2K^{\frac{3}{2}} \ {}_{\mathbf{p}}\mathbf{F}_{\mathbf{q}}\left[\frac{3}{2};\left(2,\frac{5}{2}\right);-K\right]}{3\beta n^{\frac{5}{2}}\sqrt{\pi}}$$

$$+ C_2 \mathbf{G}_{\mathbf{p}\,\mathbf{q}}^{\mathbf{m}\,\mathbf{n}}\left[0;-1;\left(-\frac{1}{2},\frac{1}{2}\right);(-1,-1);\sqrt{K};\frac{1}{2}\right] \tag{3-37a}$$

$$\cdot \frac{K}{\beta n^{\frac{5}{2}}\sqrt{\pi}} + C_3$$

$$W(X)^{LnrW} = C_1 \frac{4K^{\frac{5}{2}}\ {}_{\mathbf{p}}\mathbf{F}_{\mathbf{q}}\left[\frac{3}{2};\left(2,\frac{7}{2}\right);-K\right]}{15\beta^2 n^{\frac{5}{2}}\sqrt{\pi}}$$

$$+ C_2 \mathbf{G}_{\mathbf{p}\,\mathbf{q}}^{\mathbf{m}\,\mathbf{n}}\left[0;-1;\left(-\frac{1}{2},\frac{1}{2}\right);(-2,-1);\sqrt{K};\frac{1}{2}\right]\cdot\frac{K}{\beta^2 n^{\frac{9}{2}}\sqrt{\pi}} + C_3 X \tag{3-37b}$$

$$+ C_4$$

where $K = n^2(1+\beta X)$. ${}_{\mathbf{p}}\mathbf{F}_{\mathbf{q}}$ and $\mathbf{G}_{\mathbf{p}\,\mathbf{q}}^{\mathbf{m}\,\mathbf{n}}$ represent the generalized hypergeometric and Meijer G functions, respectively. Using the boundary conditions in Eq. (3-6) and following the same procedure as piecewise constant sections, eigenvalues and buckling mode shapes are determined by numerically solving by the resulting characteristic equation.

The linear function of the beam thickness in Figure 3-7(c) is defined as,

$$t(X) = t_{top} + \left(t_{bot} - t_{top}\right)X \tag{3-38}$$

Substituting Eq. (3-38) into the flexural stiffness function defined in Eq. (3-34), the quantities can be written as,

$$\alpha = \frac{Ebt_{bot}{}^3}{12}, \qquad \beta = \frac{t_{bot}}{t_{top}} - 1 \ \ and\ \xi = 3 \tag{3-39}$$

The linearly independent special solutions that constitute the general solution, following the form in Eq. (3-25), can be obtained, for $k_i = -\frac{1}{2}$ and $\nu_i = -1$, as,

$$
\begin{cases}
\Omega_1(X) = \sqrt{1+\beta X}\ \ \mathbf{J}_{-1}[\Phi^{LnrT}] \\
\Omega_2(X) = \sqrt{1+\beta X}\ \ \mathbf{Y}_{-1}[\Phi^{LnrT}] \\
\Phi^{LnrT} = -2n(1+\beta X)^{-\frac{1}{2}} \\
n = \sqrt{\dfrac{P}{\alpha\beta^2}}
\end{cases}
\tag{3-40}
$$

Substituting Eq. (3-40) into Eq. (3-26), the deflected shape of the linear thickness case can be written with four unknown integration coefficients C_i $(i = 1, .., 4)$. Using the boundary conditions in Eq. (3-6), the eigenvalues and the buckling mode shapes for linear thickness are obtained.

The radical function of the beam width displayed in Figure 3-7(d) can be written as,

$$
b(X) = \sqrt{b_{bot} - 2BX} \tag{3-41}
$$

where B is a parameter that controls the width variation. Taking Eq. (3-41) into the flexural stiffness function in Eq. (3-34), the quantities to define the radical shape configuration can be written as,

$$
\alpha = \frac{E\sqrt{b_{bot}}t^3}{12}, \qquad \beta = -\frac{2A}{b_{bot}} \ \ and \ \ \xi = \frac{1}{2} \tag{3-42}
$$

Similarly, the linearly independent special solutions can be written as,

$$
\begin{cases}
\Omega_1(X) = \sqrt{1+\beta X}\ \mathrm{J}_{\frac{2}{3}}[\Phi^{RadW}] \\
\Omega_2(X) = \sqrt{1+\beta X}\ \mathrm{J}_{-\frac{2}{3}}[\Phi^{RadW}] \\
\Phi^{RadW} = \frac{4}{3} n (1+\beta X)^{\frac{3}{4}} \\
n = \sqrt{\frac{P}{\alpha \beta^2}}
\end{cases}
\tag{3-43}
$$

Based on the same procedures, the shape function for radical width, $W(X)^{RadW}$, are obtained as well.

In the same manner as Eq. (3-10), the buckling modes in the fore presented cases form an orthogonal basis. Therefore, the superposition method is used to express the deflection of the beams as a linear combination of the buckling modes as,

$$
W(X) = \sum_{i=1}^{\infty} C_i \psi_i(X) \tag{3-44}
$$

where C_i $(i = 1, \dots, \infty)$ represent the weight coefficients that determine the contribution of each buckling mode to the transverse deflection.

3.2.2.2. Energy Analysis

Similarly to Section 3.2.1.2, the energy method is used to calculate the post-buckling response of the non-prismatic beam. The total energy (**Ω**) of the system is analyzed as the summation of the total potential energy (**Π**) and kinetic energy (**K**). Taking Eq. (3-44) into Eqs. (3-14) and (3-18), the total energy of the system can be obtained with respect to the unknown coefficients C_i. Solving by the constrained minimization problem defined in Eq. (3-22), the unknown coefficients are determined by numerically minimizing the total potential energy of the system within the bilateral constraints (Jiao et al., 2016).

3.3. Model Validation

3.3.1. Validation with Existing Study on Uniform Cross-Section Beams

In order to verify the current analytical formulation, the model was first simplified into a uniform cross-section and compared with the previously published results (Lajnef et al., 2014). The beam consisted of a length of 250 mm, a thickness of 2.34 mm, a width of 30 mm, a Young's modulus of 2.3 GPa, and a gap of 4 mm. The beam was partitioned into three segments with equal widths and thicknesses. The potential energy in each segment was computed. Then the total potential energy was minimized under the confinement constraints. Figure 3-8 presents the response of a uniform cross-section beam under a gradually increasing axial force, simulated by both formulations: current and previously published models. The labels $\Phi 3$, $\Phi 5$, and $\Phi 7$ refer to the dominant buckling modes to which the beam transitions after the snap-through events. Both responses coincide with a maximum difference of 7.69% at transition $\Phi 5$. We believe the slight difference is due to the numerical error from the minimization solver of the total potential energy in Eqs. (3-10) and (3-44). Since the current model addresses non-uniform beams, a more complicated total potential energy is minimized in this study than the previous work that addressed uniformed beams.

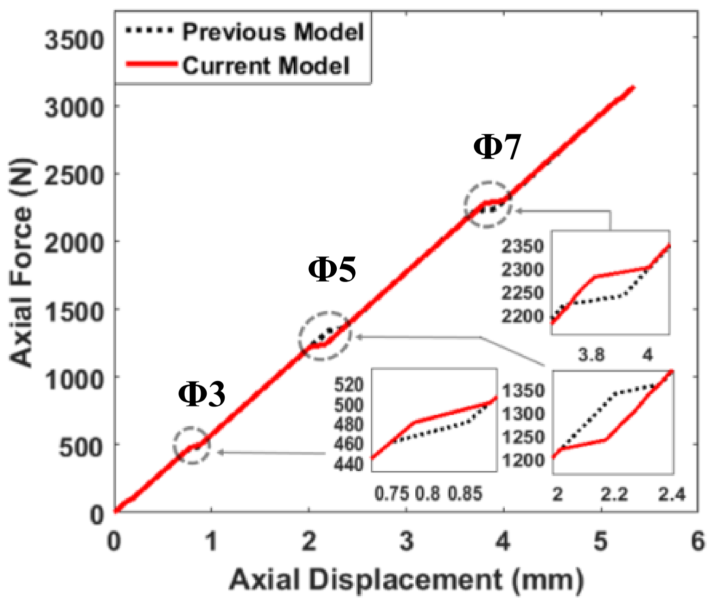

Figure 3-8. Comparison between the current and the previously published models for uniform cross-section beams.

3.3.2. Validation with Experiment

To validate the presented theoretical model, a notched polycarbonate beam, whose geometry shape is presented in Figure 3-9(a), was experimentally investigated. The experimental setup followed the setup and procedure presented in Lajnef at al. (2014). The beam had a Young's modulus of 2.3 GPa, constant thickness of 2.34 mm and total length of 250 mm. The beam had fixed end supports and was confined between two rigid aluminum constraining walls as shown in Figure 3-9(b). The gap separating the lateral constraints was fixed at 4 mm. The loading protocol consisted in applying a gradually increasing compressive force to the top of the beam using a universal mechanical testing frame. In order to highlight the deflected shapes of the tested specimen, the front edge of the beam was painted in a fluorescent color. A black light was used to separate it from its ambience as shown in Figure 3-9(c). Figure 3-9(d) shows the deflected shapes of the beam in different buckling modes.

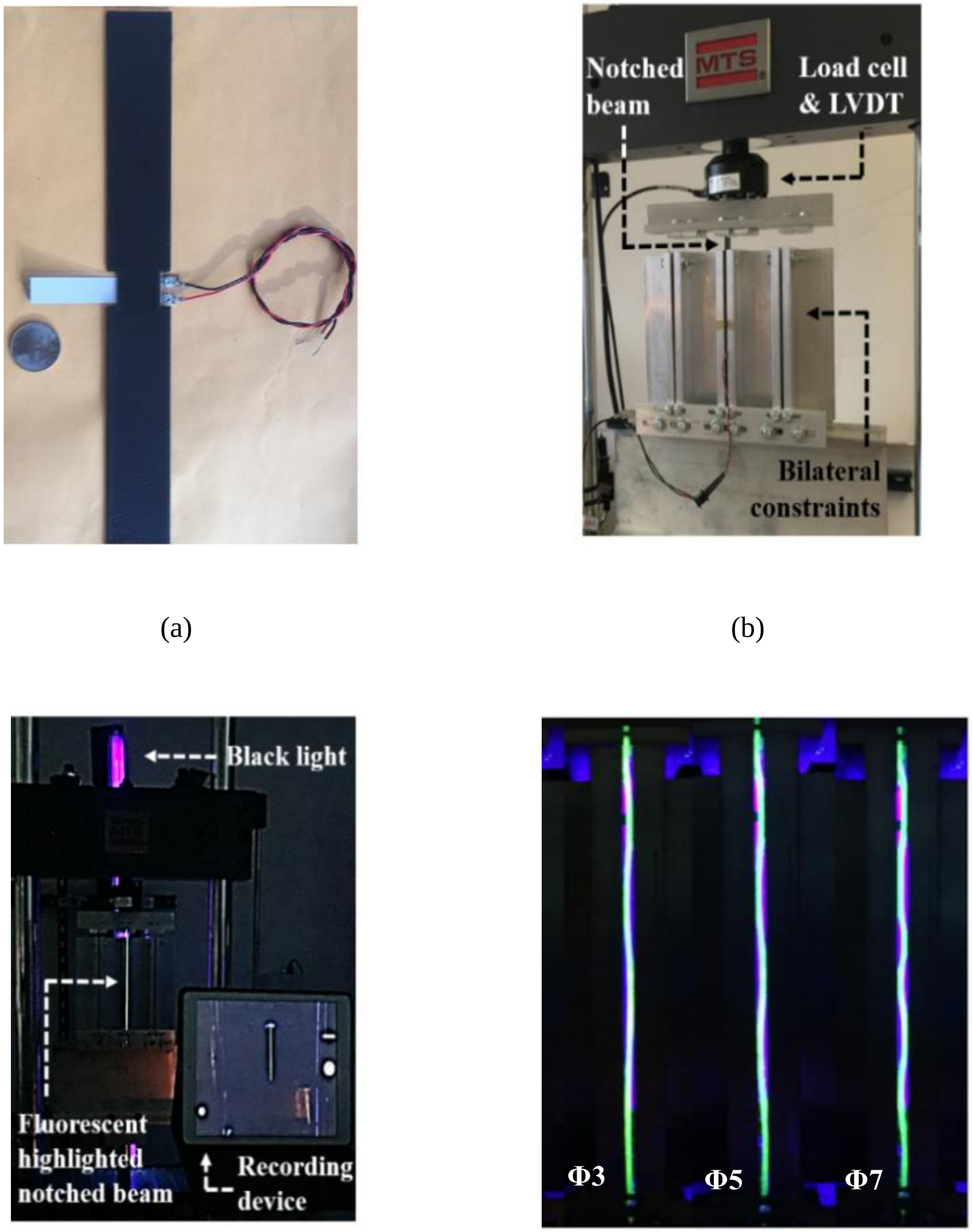

(a) (b)

(c) (d)

Figure 3-9. (a) Tested sample with an installed piezoelectric harvester, (b) testing setup, (c) testing under the black light, and (d) highlighted deflected shapes of a notched beam.

Figure 3-10 presents a comparison between theoretical and experimental results. The labels Φ_i (i = 3, 5 and 7) denote the mode transition events during which the beam jumps to a higher buckling mode i. Figure 3-10(a) highlights the difference in the force-displacement response of the beam. While, Figure 3-10(b) compares the deflected shapes of the beam under different buckling configurations. Image processing tools were used to extract the highlighted shapes of the beams at transitions. The image of the deflected beam was converted into a binary image. Then, the Canny method was used to detect the edges and contour of the beam. Thanks to the fluorescence of the beam's front edge and use of black light, the edges were sharp and easy to detect. The object was then separated from the image and normalized to match the size of the theoretical deflection shape. The number of pixels along the beam corresponds to the number of points used to discretize its length and the transverse deflection was computed by normalizing the highest bright pixel number to 1.

Table 3-2 summarizes the theoretically computed and experimentally measured axial forces as well as the difference between the deflected shapes. The error between the shapes was numerically calculated using the Euclidien distance formula expressed as,

$$Diff = \frac{\sqrt{\sum_{i=1}^{N}[\widehat{w}^{theo}(x_i) - \widehat{w}^{exp}(x_i)]^2}}{\sqrt{\sum_{i=1}^{N}[\widehat{w}^{exp}(x_i)]^2}} \times 100\% \tag{3-45}$$

where N represents the total number of points used to discretise the beam's length.

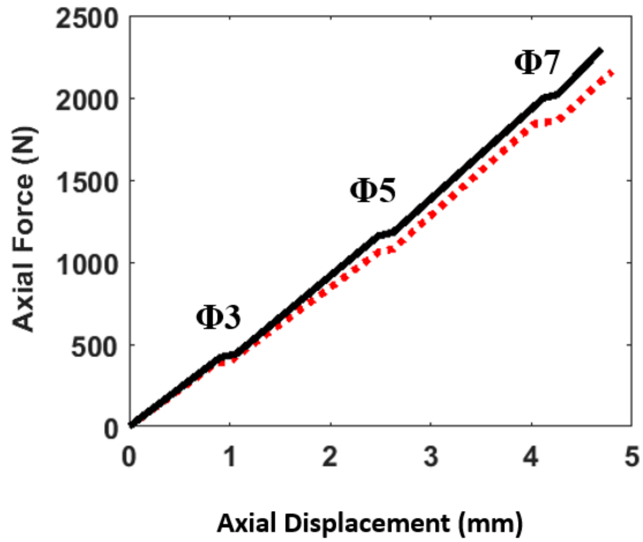

(a)

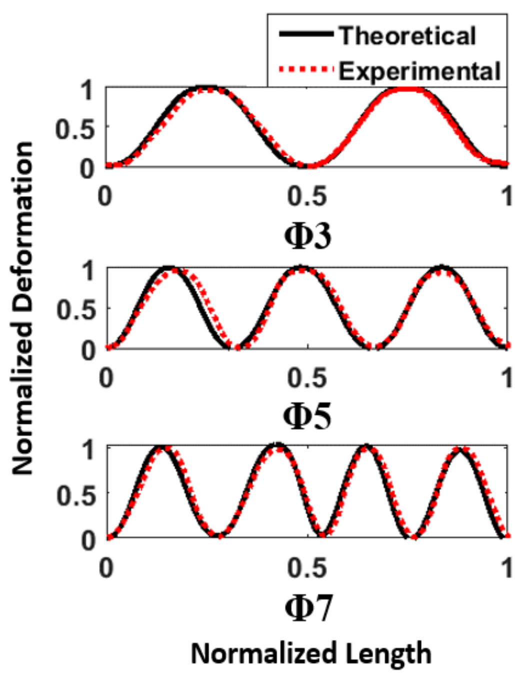

(b)

Figure 3-10. Comparisons between theoretical and experimental (a) force-displacement responses and (b) normalized deflected shape

Table 3-2. Comparison between theoretical and experimental results in terms of forces and deflected shapes at transitions.

	Spacing			Shape Diff (%)
	F^{theo} (N)	F^{exp} (N)	Error (%)	
Φ_3	420	388.92	7.99	6.78
Φ_5	1140	1061.91	7.35	**8.26**
Φ_7	2000	1840.56	**8.66**	8.22

3.4. Effect of Geometry Properties on Post-Buckling Response

3.4.1. Spacing Analysis with Respect to Force-Displacement Relationship

The main parameters that contribute to the cross-section variation are the thickness and width. Their variation can be either continuous along the beam (as shown is Figure 3-11(d)-(f)), therefore the total potential energy is computed over the whole beam, or piecewise continuous (Figure 3-11(a)-(c)) and hence, the total potential energy is the sum of partial potential energies in each segment. In the latter case, the length of each segment is considered an important parameter as well. The total length and the elastic modulus of the beam and the gap separating the lateral constraints were fixed at 250 mm, 2.3 GPa and 4 mm, respectively. The variation of the width, thickness and segments length is detailed in Table 3-3.

Table 3-3. Variable parameter in each of the studied cases.

Case	Group	Variable	Size (mm)
(a)	Piecewise constant	b_{top}	15; 20; 25; 30
(b)		L_{top}	0; 50; 100
(c)		t_{top}	1.54; 1.74; 1.94; 2.34
(d)	Linear	b_{top}	15; 20; 25; 30
(e)		t_{top}	1.54; 1.74; 2.04; 2.34
(f)	Sinusoidal	b_{min}	15; 20; 25

3.4.1.1. Piecewise Constant Cross-Section

The studied cases are divided into two groups. The first group consists of piecewise constant cross-sections where either the thickness or width varies between the segments. While, the second group consists of continuous linear or sinusoidal variation of either width or thickness. In all cases, the width and thickness at the bottom edge are constants as 30 mm and 2.3 mm, respectively. The first case presented in Figure 3-11(a) investigates the effect of the top width on the post-buckling response of the beam. The beam is divided into two equi-length segments. The top width is varied between 15 mm and 30 mm, as shown in Table 3-3. The second case, presented in Figure 3-11(b), studies the sensitivity of the response to the segments length. The top width is fixed at 15 mm (half of the bottom edge width) and the length of the top segment is varied between 0 thickness is investigated in case (c). The beam is divided into two equi-length segments and the top thickness is varied between 1.54 mm and 2.34 mm, as detailed in Table 3-3. The change in the response of the three cases is presented in Figure 3-12. The stiffness (slope within the same buckling modes) and the axial force at which the buckling transitions happened are drastically affected by the change of the studied parameters. More importantly, the spacing between the transition events, noted by Φ3, Φ5 and Φ7, is very sensitive to the geometry dimensions. Figure 3-12(a) shows that the smaller is the top width of the beam, the larger is the spacing between Φ3 and Φ5 but the lesser is the spacing between Φ5 and Φ7. The ratio between the two spacing is defined as $R = (F_7 - F_5)/(F_5 - F_3)$, where F_i denotes the axial force at which transition to buckling mode i occurs. Results in Figure 3-12(b) and (c) demonstrate similar effect of top length and thickness on the stiffness and spacing ratio between different buckling mode transitions. However, the ratio between the two spacing is found inversely proportional to both length and thickness of the top section.

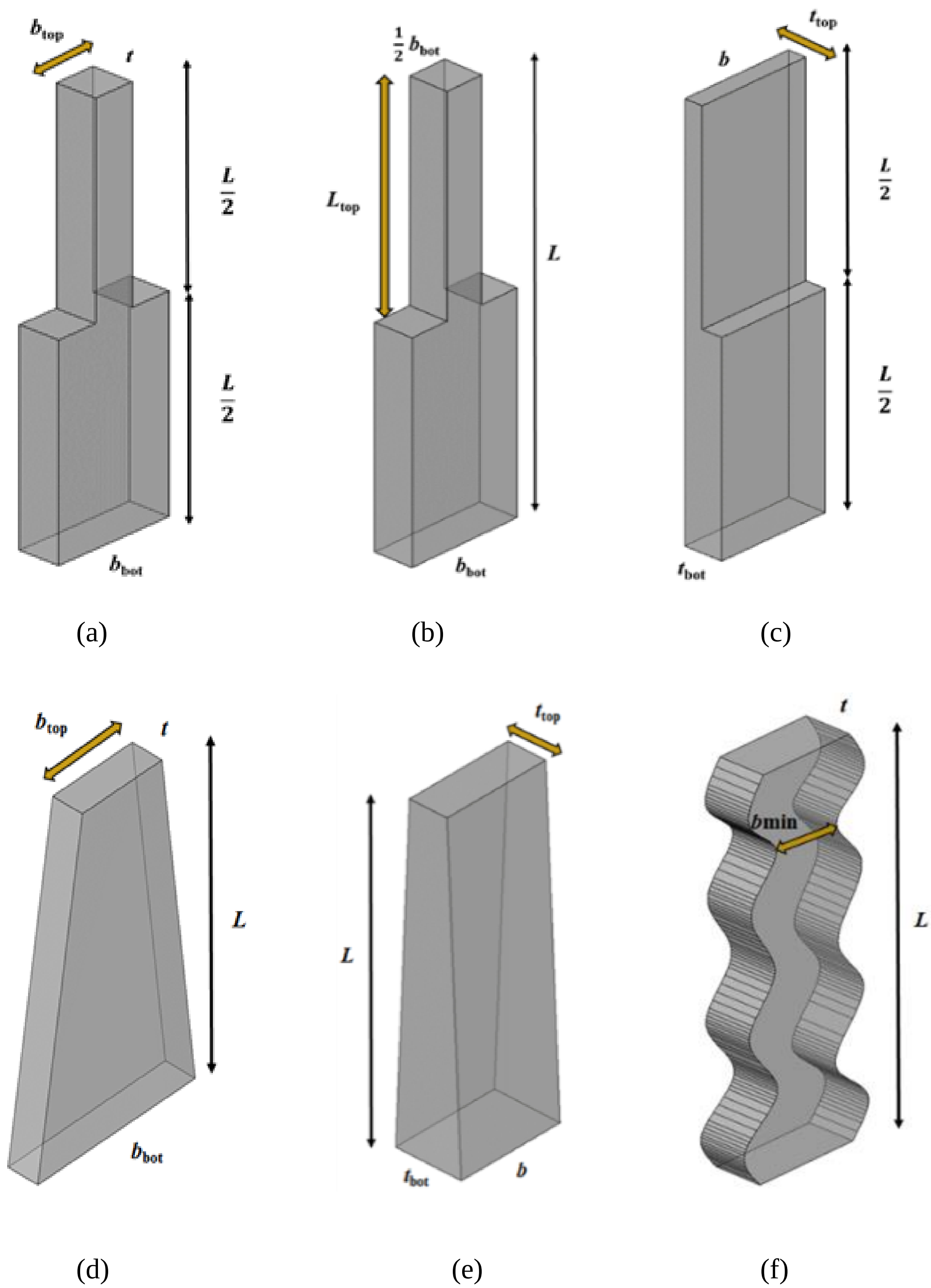

Figure 3-11. Studied cases (not to scale) comprising (a) piecewise constant width, (b) piecewise constant section with different segment lengths, (c) piecewise constant thickness (d) linear width, (e) linear thickness and (f) sinusoidal width.

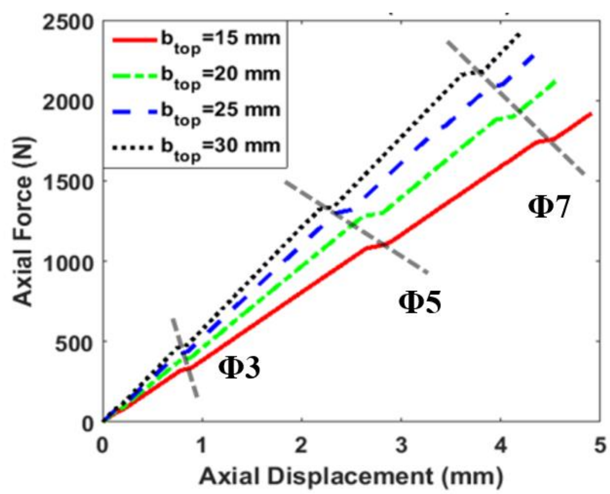

(a)

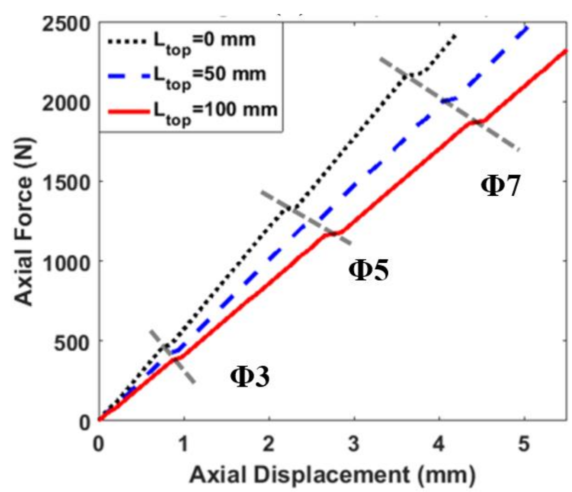

(b)

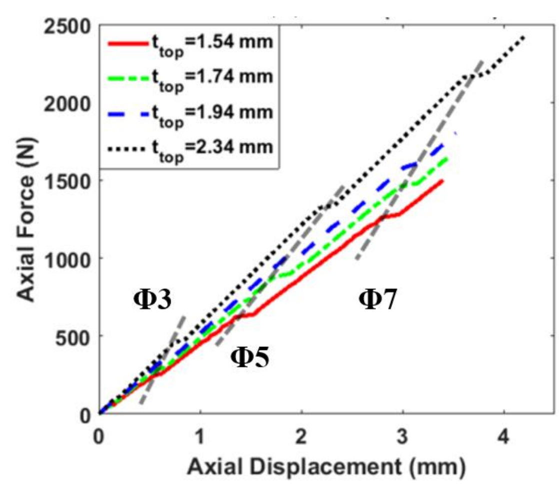

(c)

Figure 3-12. Effect of (a) top width, (b) top segment length and (c) top thickness on the transition events of a piecewise constant cross-section beam.

3.4.1.2. Linear and Sinusoidal Cross-Sections

The beam width and thickness can be defined as continuous linear or non-linear functions in terms of the longitudinal coordinate, *x*. The linear functions defining the beam width and thickness shown in Figure 3-11(d) and (e), respectively, are given by,

$$b(x) = b_{bot} - \frac{b_{bot} - b_{top}}{L} x \tag{3-46}$$

and

$$t(x) = t_{bot} - \frac{t_{bot} - t_{top}}{L} x \tag{3-47}$$

The sinusoidal function related to the width geometry presented in Figure 3-11(f) is expressed as,

$$b(x) = b_{bot} + 2A\, sin\left(2\pi m \frac{x}{L}\right) \tag{3-48}$$

where b_{bot} and t_{bot} are fixed at 30 mm and 2.34 mm, respectively, and the top thickness, t_{top}, top width, b_{top}, sine amplitude, *A*, and number of waves, *m*, are variable.

Figure 3-13(a) and (b) present the response of a beam with linear width and thickness, respectively. The width of the top edge varies between 10 mm and 30 mm and the thickness between 1.54 mm and 2.34 mm as detailed in Table 3-3. Results show that the effect of these two parameters on the beam's response is similar to the piecewise constant scenarios presented above. The effect of the sine amplitude on the response of a beam with sinusoidal width variation is presented in Figure 3-13(c). The wave number, m, was fixed at 1.

Results show that an increase in the sine amplitude (i.e. reduction of the least section width) results in a larger spacing between Φ5 and Φ7 but a lesser spacing between Φ3 and Φ5. Therefore the sine amplitude has an opposite effect to the top width in piecewise constant sections.

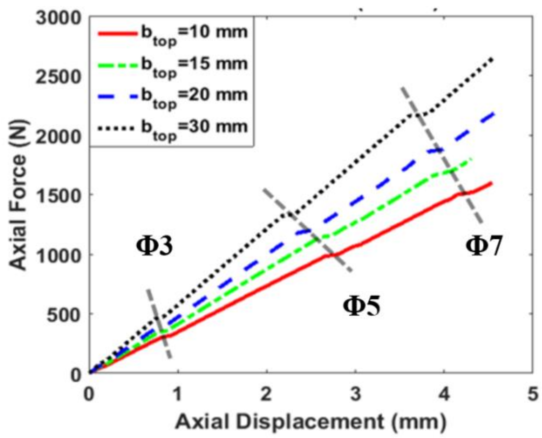

(a)

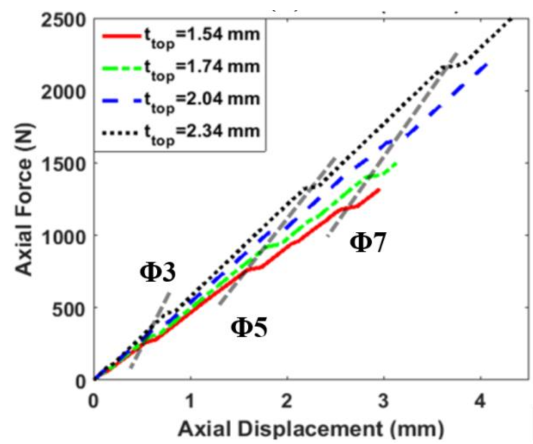

(b)

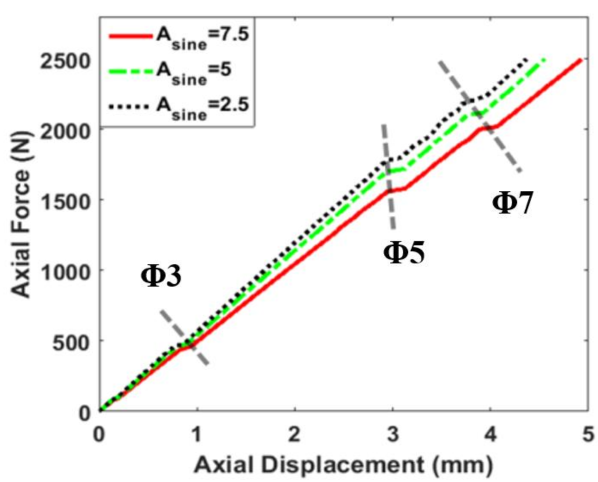

(c)

Figure 3-13. Effect of (a) top width, (b) top thickness and (c) sine amplitude on the transition events of a linearly/sinusoidally varied cross-section beam.

3.4.2. Location Analysis with Respect to Deformed Beam Shape Configuration

In this section, the theoretical model is used to examine the impact of the geometry properties (i.e. shape, width and thickness) on the beam's deformation. The same material properties as Section 3.4.1 are used. One parameter is varied in each case, while the other parameters are kept constant. Different shape configurations were considered, e.g., (a) notched width that has three uniform segments, (b) cross width that has three uniform segments, (c) linear width, (d) linear thickness, and (e) radical width. Table 3-4 summarizes the geometry variation that corresponds to each of the configurations.

The distance traveled by the beam during a transition is defined as the difference between its deflected shapes just before and after that transition. It can be expressed by,

Table 3-4. Beam geometry variation in different configurations.

Case	Configuration	Variable	Size (mm)
(a)	Notched width	b_{notch}	15; 17; 20; 25
(b)	Cross width	b_{mid}	35; 37; 45
(c)	Linear width	b_{top}	15; 17; 20; 25
(d)	Linear thickness	t_{top}	1.54; 1.74;1.94; 2.04
(e)	Radical width	b_{top}	15; 17; 20; 25

$$W_{td} = W_{post} - W_{pre} \tag{3-49}$$

The location of the maximum traveled distance is the abscissa x that maximizes that difference, as shown in Figure 3-14. The results presented in Figure 3-14 correspond to case (a) in Table 3-4 where the top width b_{top} is 15 mm. The maximum traveled distances are located at 0.56, 0.33, and 0.54, for transitions Φ_3, Φ_5 and Φ_7, respectively. Our objective is to design the beam such that all transitions occur at the same location which will be the most suitable site to attach the energy harvester.

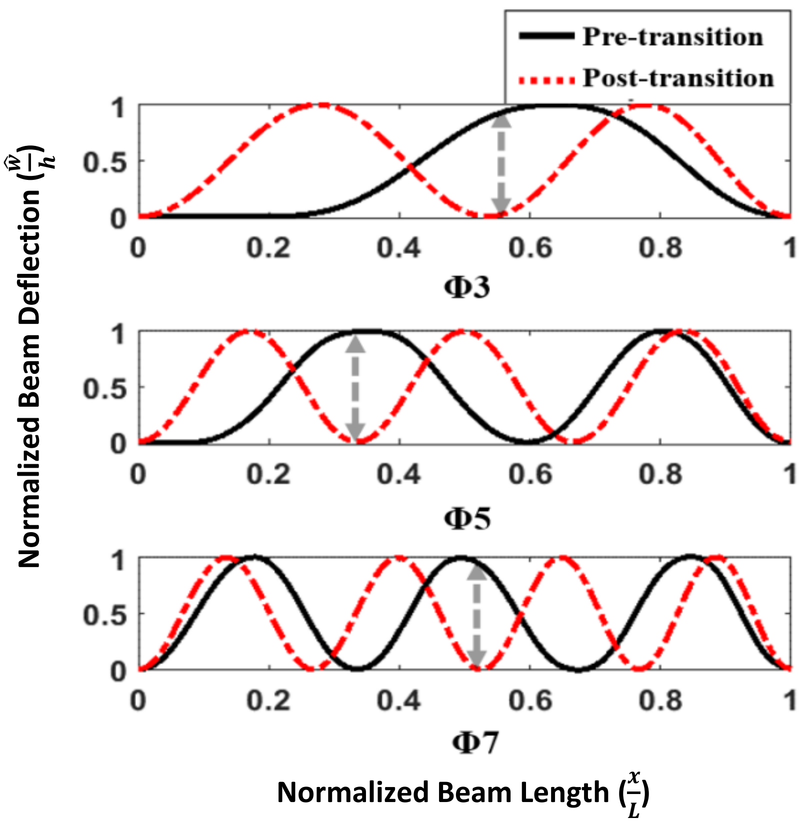

Figure 3-14. Locations of the maximum traveled distance during buckling mode transitions (Case (a) in Table 3-4, b_{top}=15 mm).

3.4.2.1. Notched Width

Figure 3-15(a) and 3-16(a) show the traveled distances and the migration of the snap-through locations with respect to the notch width that changes from 15 mm to 25 mm. The transitions Φ_3 and Φ_5 are shown non-sensitive to the width ofthe notch and always occur at the same location which is the beam's midspan. As b_{notch} increases, the location of Φ_7 tends to approach the midspan as well. Note that only the width of the notch is considered in this section. Its length, thickness and location surely affect the snap-through behavior as well.

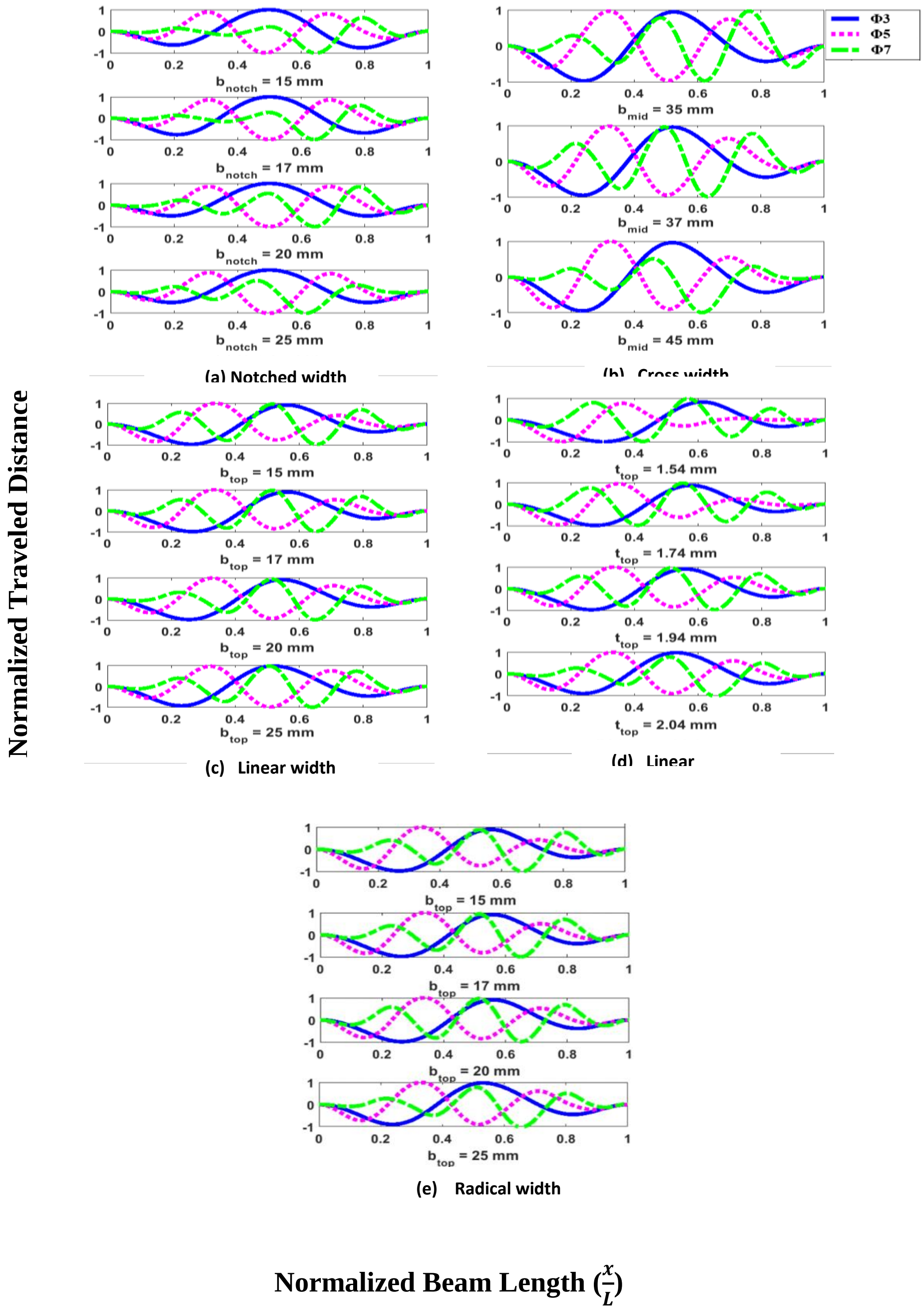

Figure 3-15. Normalized distance traveled during buckling mode transitions for different beam configurations.

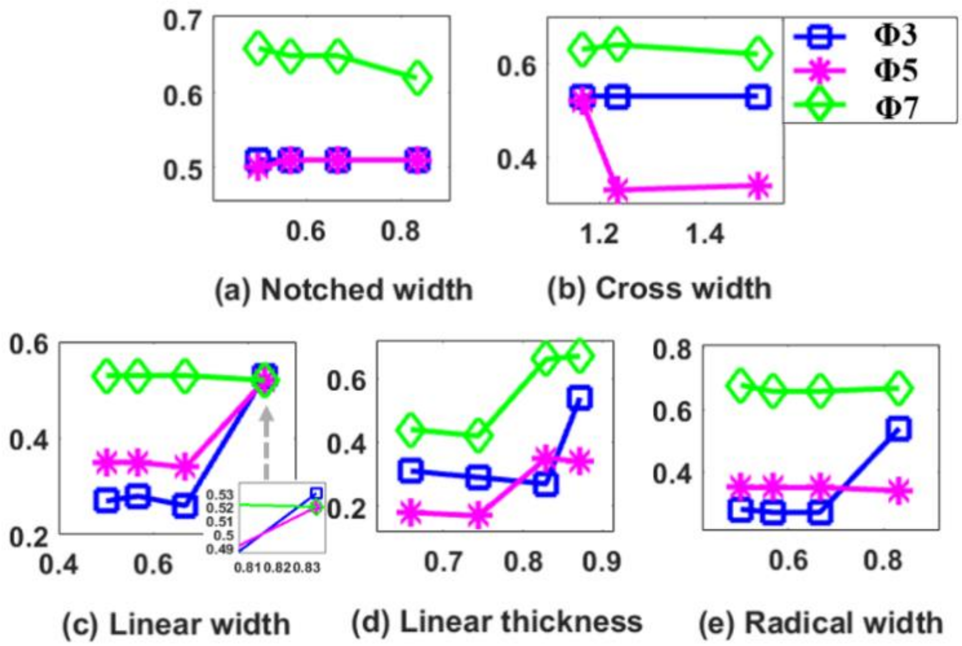

Figure 3-16. Migration of the snap-through locations with respect to the variables for different beam shape configuration

3.4.2.2. Cross Width

Figure 3-15(b) and 3-16(b) present the traveled distances and the migration of the snap-through locations, respectively, in terms of the cross width. The width varies between 35 mm and 45 mm. Two of the transitions (i.e. Φ_3 and Φ_7) maintain their locations as the width changes. Therefore, this configuration is not suitable for our application.

3.4.2.3. Linear Width

The top width of the beam is varied between 15 mm and 25 mm. Figure 3-15(c) shows the normalized traveled distance at transitions, for different top width values. It can be seen that the snap-through locations are sensitive to the top width. The locations of transitions Φ_3 and Φ_5

approach the midspan of the beam as the top width increases. However, Φ_7 remains invariant. Figure 3-16(c) displays the change in the transition locations due to top width variation.

3.4.2.4. Linear Thickness

In the linear variation of the beam's thickness, Figure 3-15(d) displays the traveled distance with respect to the beam's top thickness that varies from 1.54 mm to 2.04 mm. The location of the largest traveled distance is extremely sensitive to the top thickness. Figure 3-16(d) shows that for low values of top thickness, the snap-through tends to occur in the thicker half of the beam.

3.4.2.5. Radical Width

The top width varies between 15 mm and 25 mm. Figure 3-15(e) displays the influence of such configuration on the distance traveled by the beam at transitions. This figure shows similar transition patterns as the linear width variation shown in Figure 3-15(a). However Figure 3-16(e) highlights that the locations of the transition Φ_7 are not the same and, more importantly, the location of both transitions Φ_5 and Φ_7 are non-sensitive to the top width in this configuration.

To sum up, the snap-through locations are more sensitive to the linear and notched width than the other studied configurations. Therefore, the next section focuses on designing beams in these categories such that they exhibit all buckling mode transitions at the same location.

3.4.3. Spacing and Location Analysis

In this section, the theoretical model is used to examine the impact of different geometry shapes on the spacing and location of the transitions. Four configurations of non-uniform cross-section beams were considered: linear, notched, radical and sinusoidal. In each case, two parameters are varied as shown in Figure 3-17. Through the entire study, the beam's Young's modulus E and gap between the two lateral constraints h_0 are maintained invariant and equal to 2.3 GPa and 4 mm, respectively. The width b_{bot} and thickness t_{bot} at the bottom of the non-uniform beams are also fixed at 30 mm and 2.34 mm, respectively. The notched beam configuration is displayed in Figure 3-17(b). The notch width and length are both fixed at 15 mm. The linear variation of the beam's width and thickness, shown in Figure 3-17(a), are defined as linear functions of x as,

$$b(x) = b_{bot} - \frac{(b_{bot} - b_{top})}{L} x \tag{3-50}$$

$$t(x) = t_{bot} - \frac{(t_{bot} - t_{top})}{L} x \tag{3-51}$$

In the same manner, the radical width variation in Figure 3-17(c) is given by,

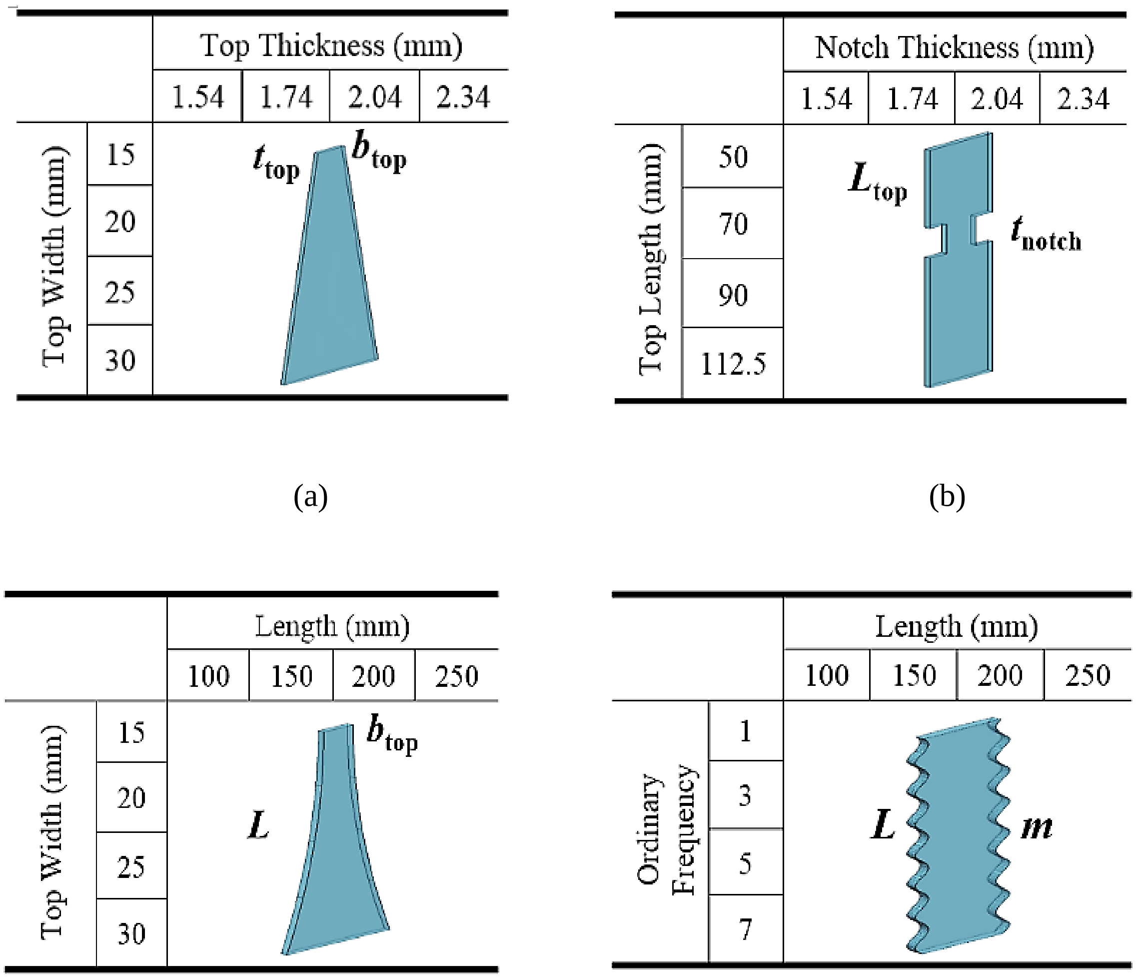

(a) (b)

(c) (d)

Figure 3-17. Investigated (a) linear, (b) notched, (c) radical, and (d) sinusoidal beam configurations.

$$b(x) = b - 2\beta\sqrt{x} \tag{3-52}$$

where β represents a parameter that defines the width change. The sinusoidal width of the beam shown in Figure 3-17(d) is defined by,

$$b(x) = b_{bot} + 2Bsin\left(2\pi m \frac{x}{L}\right) \tag{3-53}$$

where B and m denote the amplitude of the sinusoidal function and number of waves, respectively.

Figure 3-18 presents the effect of linear variations of thickness and width on the spacing between transitions. The different buckled configurations of the beam are shown in Figure 3-18(a). The displayed beam corresponds to a 2.04 mm top thickness and a 15 mm top width. The corresponding force-displacement response is displayed in Figure 3-18(b). The forces at which transitions occur are highlighted in the figure. Figure 3-18(c) shows the influence of the top width and thickness on the spacing ratio. Note that the top width is changed from 15 to 30 mm, and the top thickness from1.54 to 2.34 mm, as detailed in Figure 3-17(a). The variation ranges of these two parameters induce a variation of the spacing ratio between 0.7 and 1.2. The nadir value is obtained when the top width and thickness are in the middle of the ranges, and the peak value is when the variables are at the edges. The impact on the locations of the snap-through transitions is presented in Figure 3-19. The deflected shapes of the beam before and after each transition are displayed in Figure 3-19(a). Figure 3-19(b) displays the distance traveled by the beam during snap-throughs. The locations of the maximum traveled distances are highlighted in the figure. Figure 3-19(c) presents the variations of the snap-through locations due to top width and thickness. It can be seen that they are most likely to coincide when the beam's top width and top thickness reach the peak values. The normalized location difference D is determined as displayed in Figure 3-19(d). The design goal is to eliminate D, such that all transitions occur at the same place. This goal can be met by selecting the variable values within the region highlighted by a red circle.

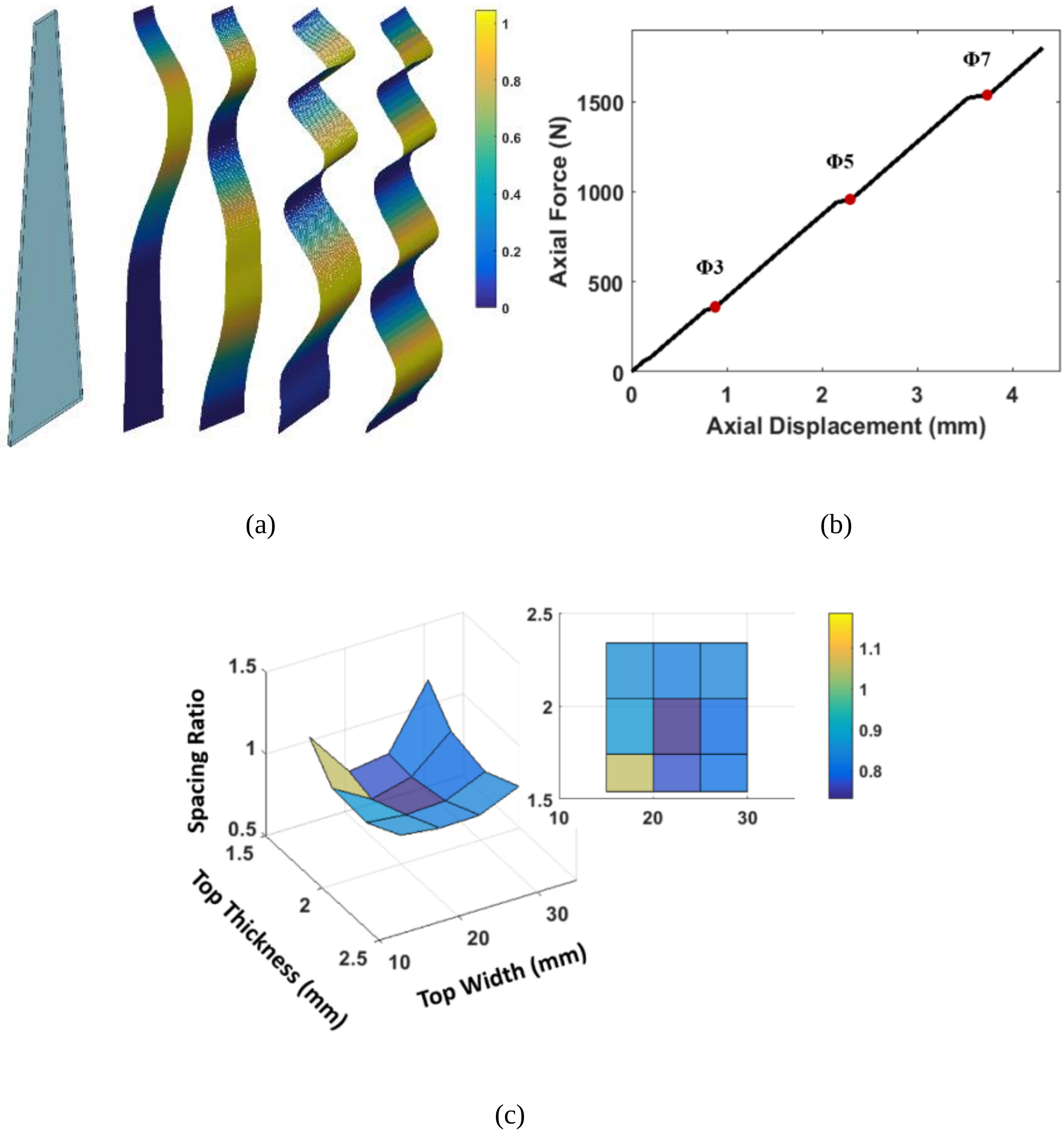

Figure 3-18. (a) Buckled configurations, (b) force-displacement response, and (c) spacing ratio with respect to the top width and thickness of a linear beam.

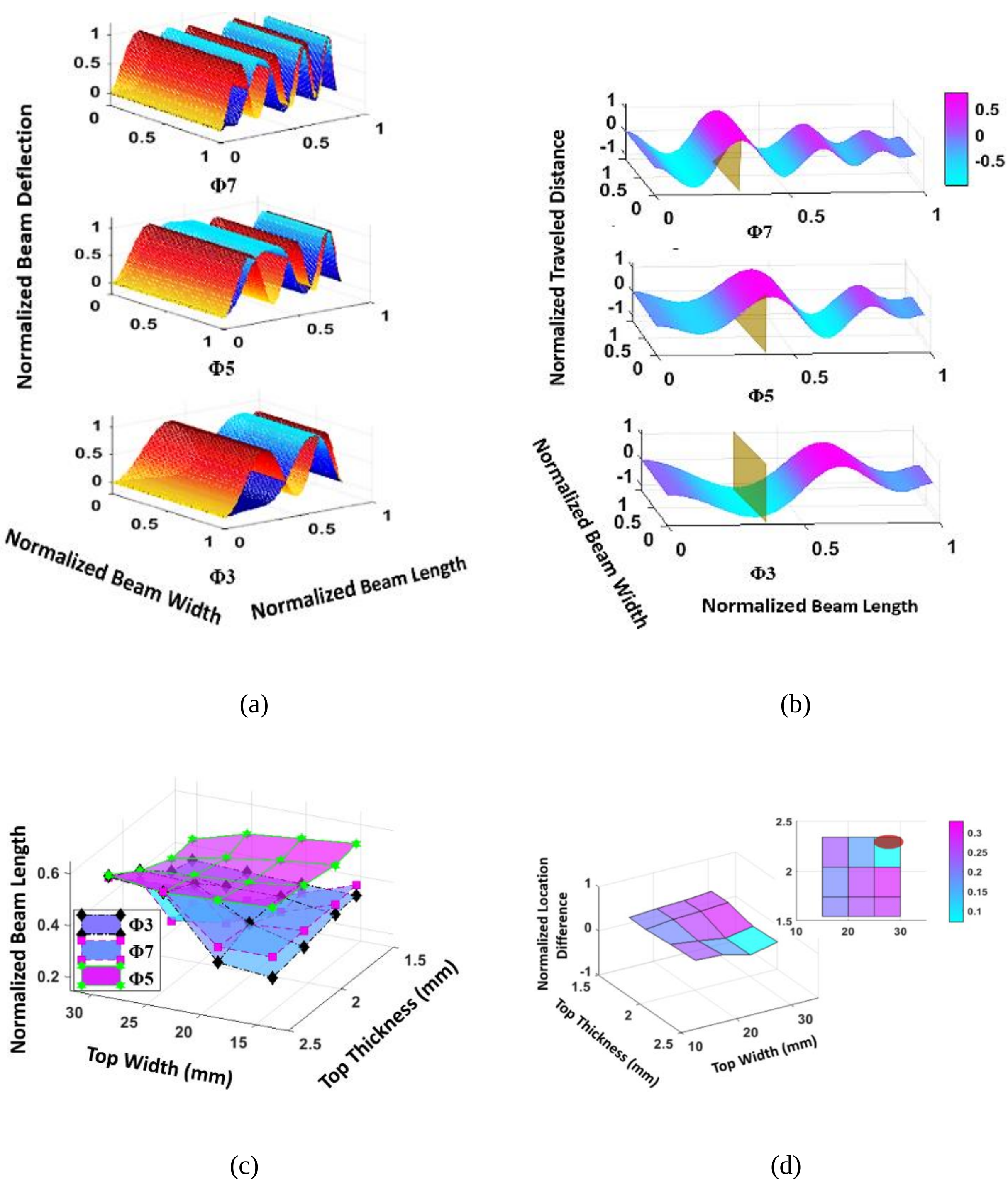

Figure 3-19. (a) Deflected shapes, (b) normalized traveled distance, (c) variation of snap-through locations and (d) normalized location difference with respect to the top width and thickness of a linear beam.

Similarly, the notched beam configuration presented in Figure 3-17(b) is studied. The top length and notch thickness vary as detailed in the figure. Figure 3-20(a) shows the normalized deflected beam shapes. The displayed beam corresponds to a 70 mm top length and a 1.74 mm notch thickness. The effect of the two parameters on the spacing ratio and normalized location difference are shown in Figure 3-20 (b) and (c), respectively. It can be seen that the spacing ratio varies from 0.9 to 1.3. Lower values are achievable by increasing the top length and notch thickness. On the other hand, the mismatch between the snap-through locations can be eliminated by adopting a top length and notch thickness within the region highlighted in Figure 3-20(c).

Figure 3-21 investigates the effects of the top width and beam total length of the radical beam's response. Figure 3-21(a) shows the deflected beam shapes. The displayed beam corresponds to a 15 mm top thickness and a 150 mm length. Figure 3-21(b) presents the variation of the spacing ratio due to the investigated parameters. Results show that the spacing is significantly affected by the beam length, but non-sensitive to the top width. For instance, if the length increases from 100 mm to 250 mm, the ratio changes approximately from 0.2 to 1.2. Figure 3-21(c) displays the effect on the snap-through location. Results show that the minimum location difference that can be achieved using this geometry configuration is around 0.15. Therefore, this configuration is not suitable for this study.

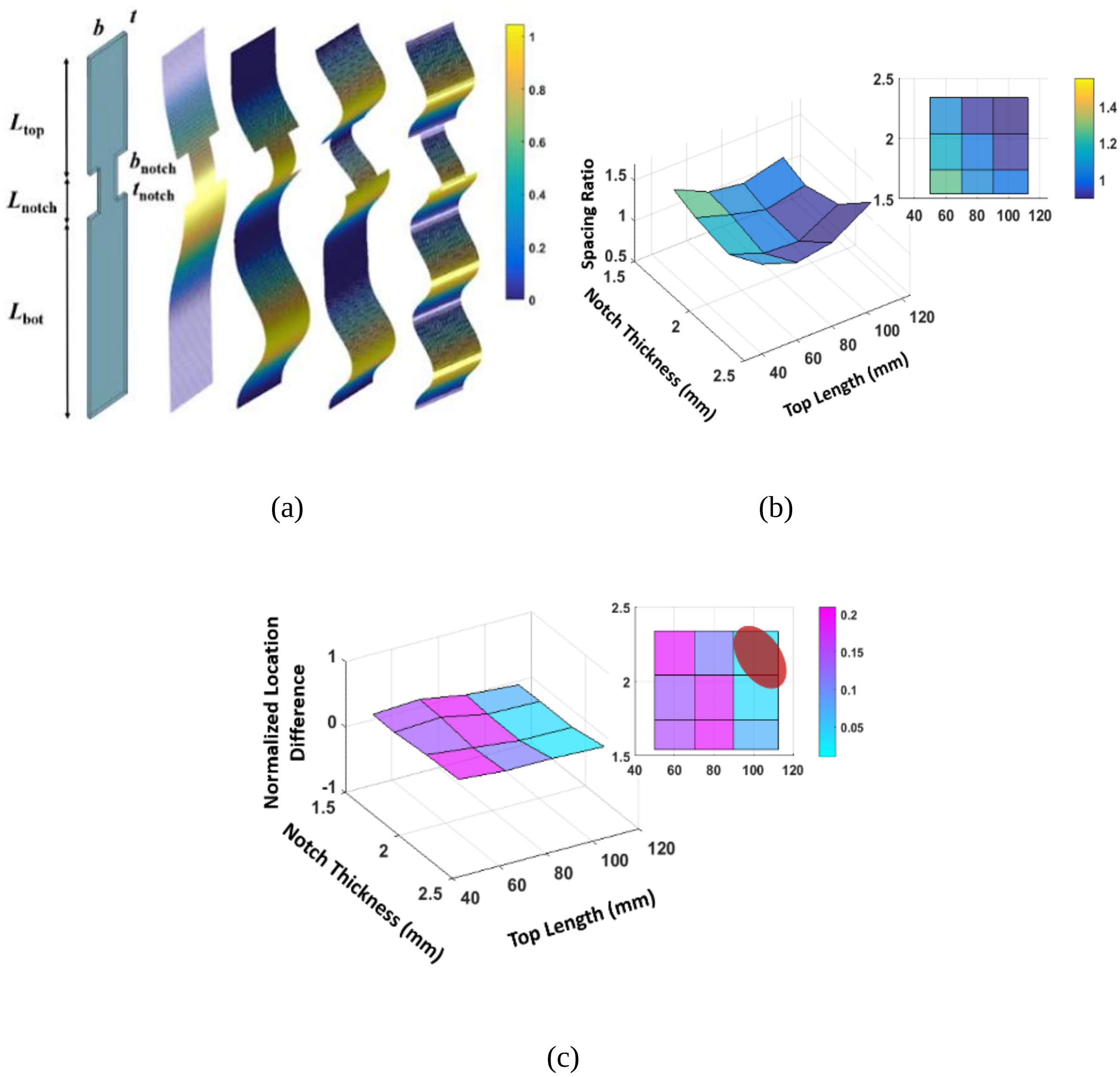

Figure 3-20. Spacing and location studies of the notched beam with respect to the top length and notched thickness: (a) deflected beam shapes, (b) spacing ratio and (c) normalized location difference.

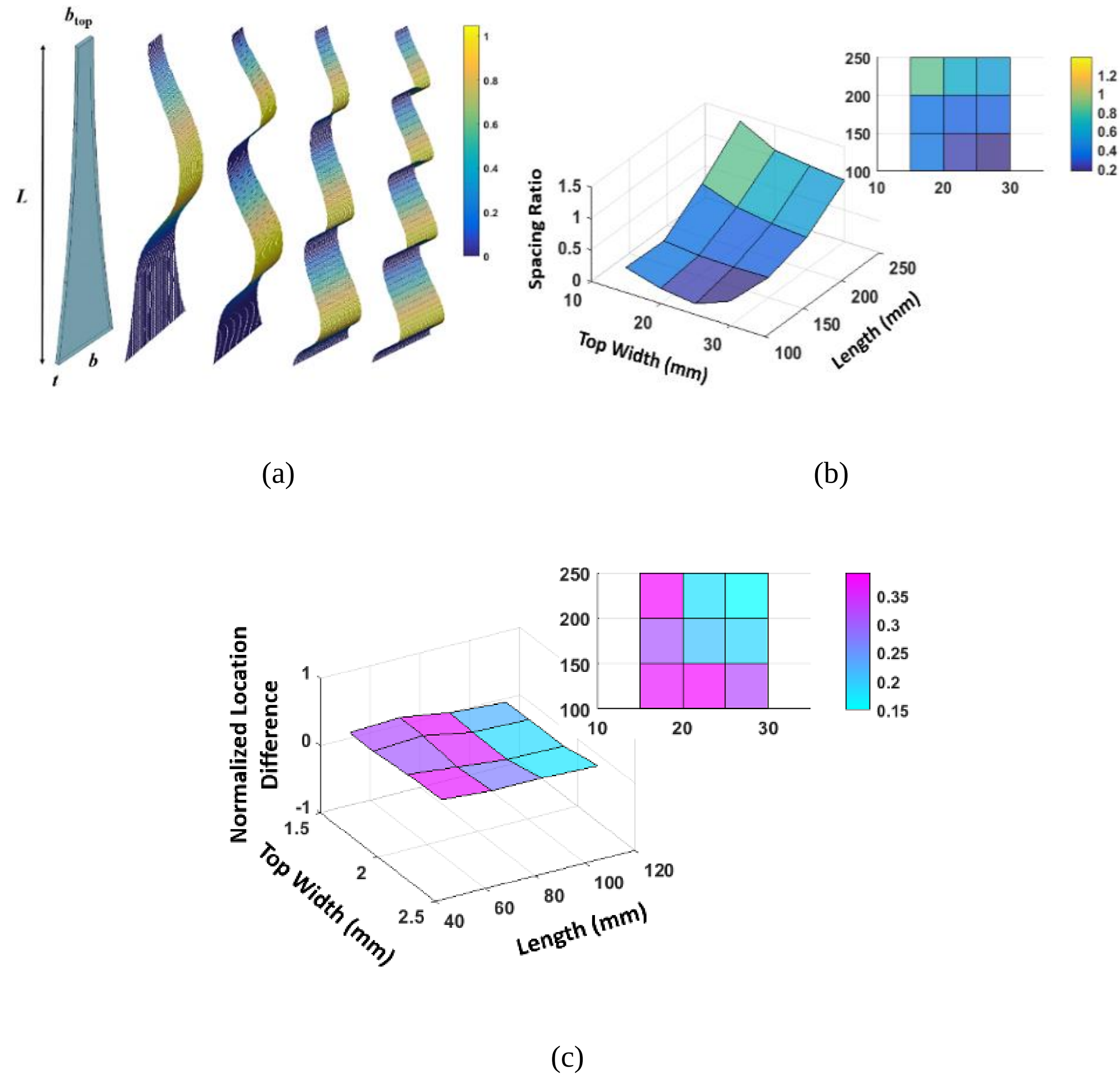

Figure 3-21. Spacing and location studies of the radical beam with respect to the top width and beam length: (a) deflected beam shapes, (b) spacing ratio and (c) normalized location difference.

The sinusoidal beam configuration presented in Figure 3-17(d) is investigated with respect to its ordinary frequency and beam length. Figure 3-22(a) shows the buckled beam shape. The ordinary frequency and length of the displayed beam are 7 and 200 mm, respectively. Figure 3-22(b) shows that the spacing ratio, R, is likely to be proportional to the ordinary frequency, but inversely proportional to the beam length. The design goal of eliminating the location difference can be obtained when the beam length is close to 250 mm, as marked in Figure 3-22(c). Results show that the ordinary frequency does not affect the transition locations as critically as the beam length.

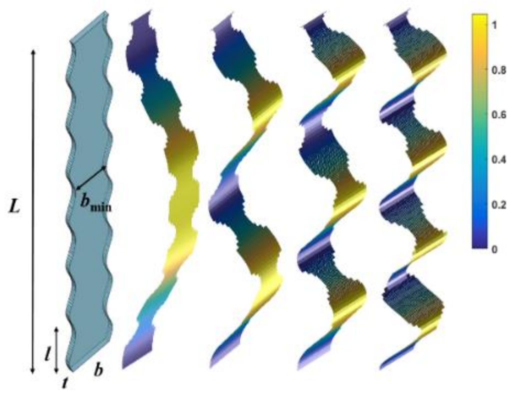

(a)

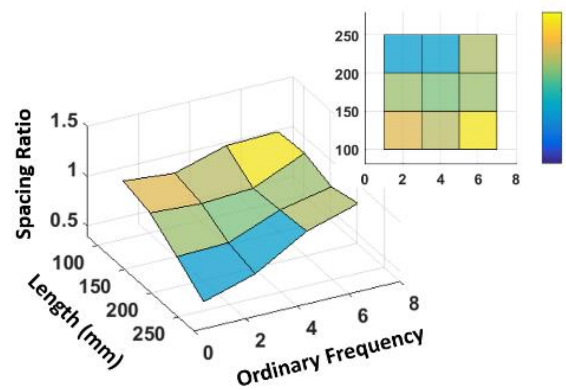

(b)

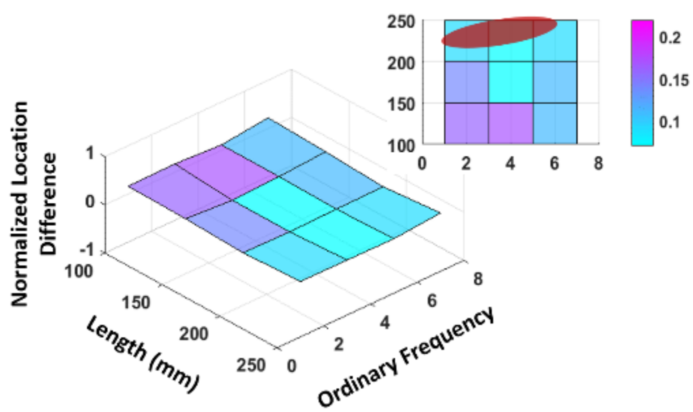

(c)

Figure 3-22. Spacing and location studies of the sinusoidal beam with respect to the ordinary frequency and beam length: (a) deflected beam shapes, (b) spacing ratio and (c) normalized location difference.

According to the results presented in Figure 3-18 to 3-22, the spacing ratio can be varied approximately from 0.2 to 1.3 and a unique transition location can be achieved by adopting linear, notched or sinusoidal beam configurations. On the other hand, the radical beam does not exhibit the desired behavior and, therefore, will be excluded from the considered configurations.

3.5. Optimal Design

3.5.1. Spacing Design

The main objective in this section is to attain elastic post-buckling responses with controlled spacing between buckling mode transitions. The primary parameters controlling the post-buckling behavior of a beam are its width, thickness and length of its segments in the case of piecewise constant cross-sections. Therefore, it is crucial to investigate their effect on the spacing ratio, *R*. Figure 3-23 displays the spacing ratio variation with respect to the beam's top width and thickness in both piecewise constant and linear scenarios (Figure 3-11(a), (c), (d) and (e)), top segment length in piecewise uniform cross-sections (Figure 3-11(b)) and minimum cross-section width in a sinusoidal width variation scenario (Figure 3-11(f)). Results in Figure 3-23(a) and (b) show that piecewise constant width and/or thickness allows more control over the spacing between transitions than linear width or thickness variation as it covers a wider range of spacing ratio values. High values can be attained by reducing the top thickness and adopting either piecewise constant or linear cross-sections. On the other hand, low ratio values can be easily achieved either by increasing the length of the top segment (Figure 3-23(c)) or adopt a sinusoidal shape (Figure 3-23(d)). It should be mentioned that a unit spacing ratio is attainable by many geometry configurations such as sinusoidal or even uniform cross- section beams.

Results in Figure 3-23 prove that a large range of spacing ratio can be covered by varying the shape and/or geometry dimensions. Figure 3-24 presents examples of beam geometries with different spacing ratios that span between 0.25 and 1.5. Their force-displacement responses are presented in Figure 3-25.

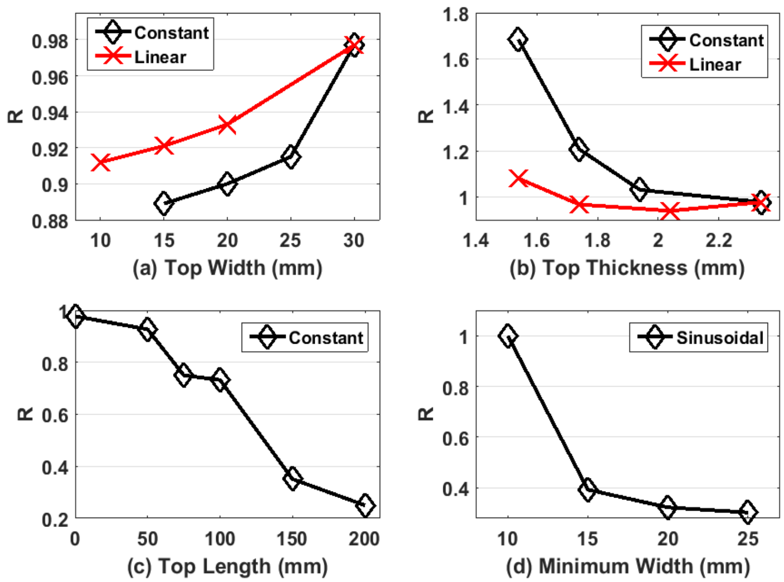

Figure 3-23. Variation of the spacing ratio with respect to (a) top width in piecewise constant and linear scenarios, (b) top thickness in piecewise constant and linear scenarios, (c) top segment length in a piecewise constant cross-section scenario and (d) minimum width in a sinusoidal scenario.

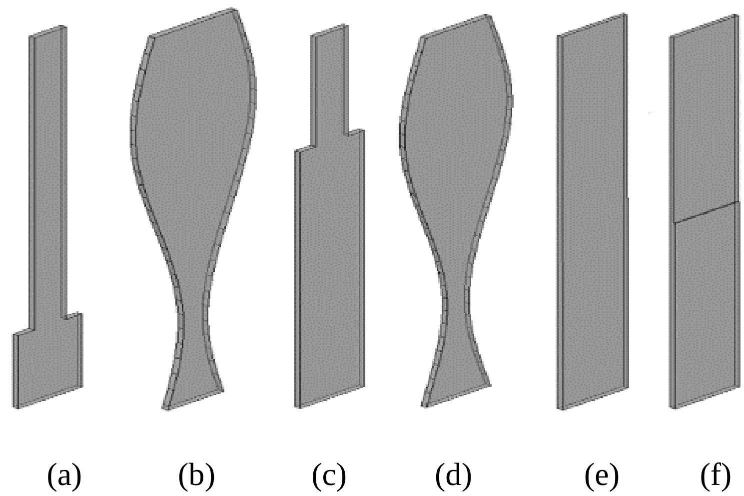

Figure 3-24. Beam configurations with specific spacing ratio (a) R=0.25, (b) R=0.5, (c) R=0.75, (d) R=1.0, (e) R=1.25 and (f) R=1.5.

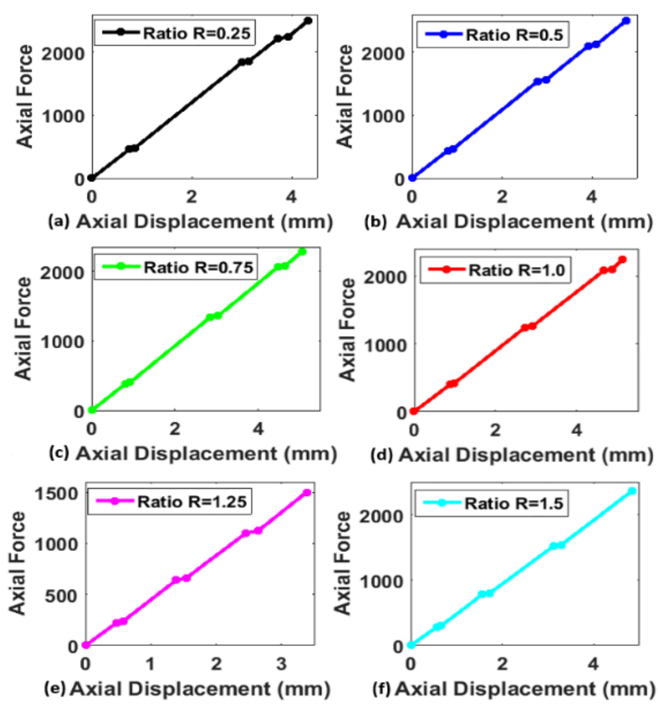

Figure 3-25. Force-displacement responses with transition spacing ratios (a) R=0.25, (b) R=0.5, (c) R=0.75, (d) R=1.0, (e) R=1.25 and (f) R=1.5.

As shown in the Figure 3-25, the shape and dimension properties of the beam not only affect its stiffness but more importantly, the ratio between its transition events. It can be designed in a way to control the exact axial force values at which transitions occur. For instance, the beam shape presented in Figure 3-24(a) was designed to achieve a spacing ratio of 0.25 as shown in Figure 3-25(a). The top width is fixed at 15 mm and the length of the top segment was determined to be 200 mm. Similarly, the target spacing ratios of 0.5 and 1 are obtained by reducing the minimum width of the sinusoidal beam to 13 mm and 10 mm, as shown in Figure 3-24(b) and (d), respectively. Likewise, a ratio of 1.25 was achieved by adjusting the top thickness to 1.45 mm and adopting a linear thickness variation (as shown in Figure 3-24(e)), while a ratio of 1.5 is attained by a piecewise constant thickness configuration with a top thickness of 1.7 mm. To validate the designs presented in Figure 3-24, the geometry configuration that corresponds to a spacing ratio of 0.75 (presented in Figure 3-24(c)) was experimentally tested. This configuration was chosen for its ease of construction. The experimental and theoretical post-buckling responses of the beam are displayed in Figure 3-26. Results show a good agreement between the theoretical and experimental results. Table 3-5 summarizes the theoretical and experimental forces at which mode transitions occur and the spacing ratio between the transitions. It can be seen that the theoretical model accurately predicted the buckling events of the designed beam with a maximum error of 3.36% in terms of the axial force recorded at transition $\Phi 7$.

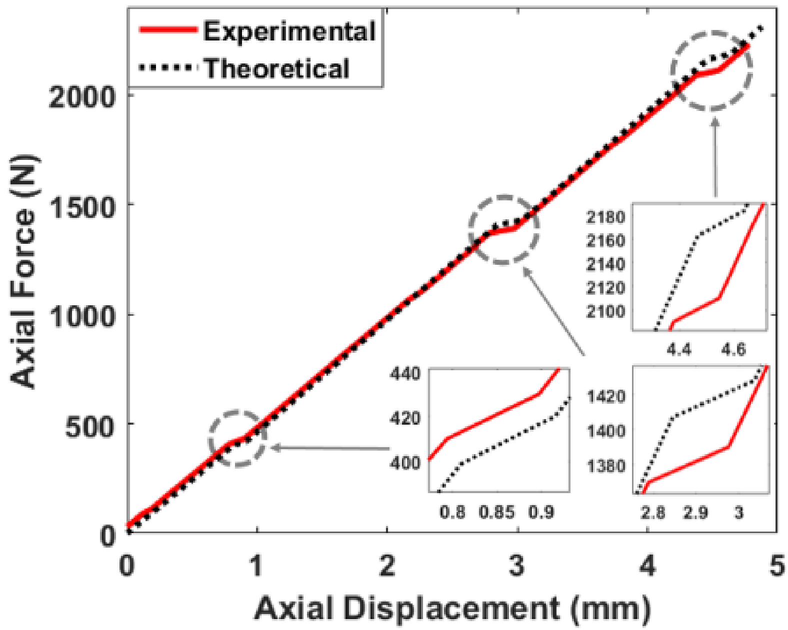

Figure 3-26. Theoretical and experimental post-buckling responses of the beam designed with a 0.75 spacing ratio.

Table 3-5. Comparison between theoretical and experimental results.

	Force at mode transitions			R
	F_3 (N)	F_5 (N)	F_7 (N)	
Theoretical	400	1400	2160	0.76
Experimental	410.6	1362.4	2087.5	0.762
Error (%)	0.49	1.74	3.36	0.26

3.5.2. Location Design

The optimal design in this section is defined such that the snapping point is the same during all buckling mode transitions. In order to achieve such a goal, design parameters must be adjusted such that the snap-through location curves, presented in Figure 3-16, intersects at one point. It can be seen that notched and linear width configuration, presented in Figs. 3-16(a) and (c), provide adequately close intersection points, unlike the other configurations. Therefore, linear and notched width configurations are selected to design for a beam that snaps at the same location for all transitions. In Figure 3-16(c), the intersection between the curves representing Φ_3 and Φ_5 occur at $b_{top}/b_{bot} = 0.816$, and Φ_5 and Φ_7 at $b_{top}/b_{bot} = 0.824$. Since the two ratios are close, a mean ratio of 0.82 (i.e. top width of 24.6 mm) is selected.

Figure 3-27 displays deflected shapes of the designed linear width beam just before and after each transition as well as the location of the maximum traveled distance. Table 3-6 details the geometry properties of the beam as well as the snap-through locations and traveled distances during transitions.

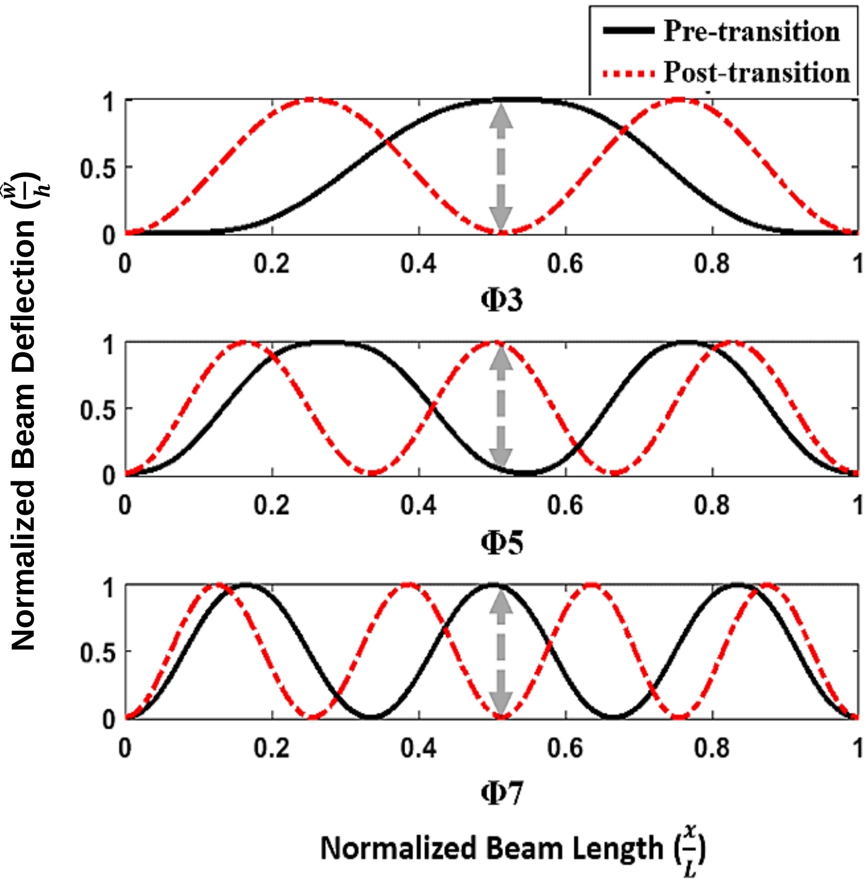

Figure 3-27. Location of the snap-through in the designed linear width configuration

$(\frac{b_{top}}{b_{bot}} = 0.824)$.

Table 3-6. Geometry properties of the optimally designed beams.

	Design Variable		Length (mm)	Thickness (mm)	Width (mm)	Mode Transition	Traveled distance	Location
						Φ_3	0.9999	0.51
Linear	Top Width	24.6	250	2.34	30	Φ_5	0.9759	0.51
						Φ_7	0.9433	0.51
	Notch length	15				Φ_3	1	0.5
Notch	Notch width	20	105 105	2.04	30	Φ_5	1	0.5
	Thickness	1.94				Φ_7	0.9973	0.5

As pointed out in the previous section the notched configuration is of great practical interest to install the piezoelectric transducer. Figure 3-16(a) only examined the effect of the notch width, while other parameters such as the notch length, notch thickness and notch location are fixed. The snap-through location can be further controlled by tuning these parameters. Table 3-6 presents the geometry properties of a notched beam designed to snap at its midspan during all transitions. The notch is placed at the midspan such that the beam is symmetric. Therefore, the deflected configuration is always symmetric and the snapping point at transitions is located at the beam's midspan. The deflected shapes and transitions location are shown in Figure 3-28. The linear and notched beams designed in this section offer the advantage of increasing the efficiency of the energy harvester. The snap-through transitions always occur at the same location that constitutes the ideal site to place a piezoelectric energy scavenger. Therefore the scavenger's base is always excited with the maximum acceleration that can be generated during transitions.

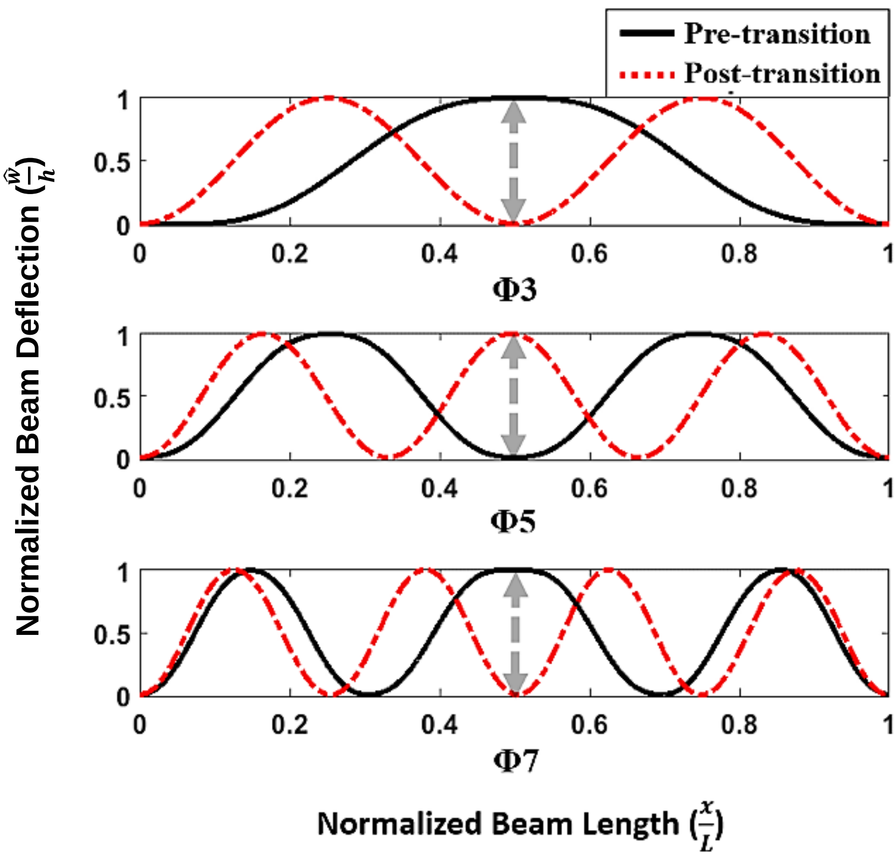

Figure 3-28. Location of the snap-through in the designed notched beam configuration.

In order to validate the designs presented in Section 4, the designed notch configuration, whose deflected shapes were presented in Figure 3-28, was experimentally tested. The experimental setup and loading protocol are as described in Section 2.2. A PVDF piezoelectric energy harvester oscillator was mounted in a cantilevered configuration at the midspan of the polycarbonate strip in order to harvest the snap-through energy. Figure 3-29 shows the beam, PVDF film and tip mass. The material and geometry properties of the energy harvester are summarized in Table 3-7. The lumped mass was 0.27 g and the output voltage was measured across a 50 MΩ resistor. Note that PVDF piezoelectric elements were used for ease of handling and installation. However, flexible PZT/Aluminum harvesters can be used to generate higher levels of power.

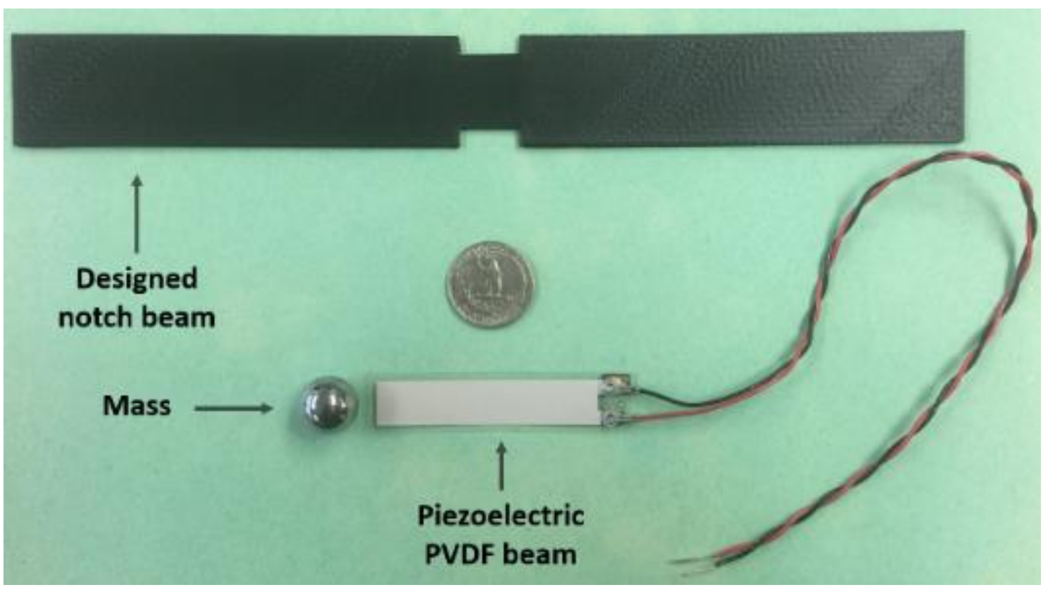

Figure 3-29. Designed notch beam and PVDF vibrator.

Table 3-7. Designed beam configurations and geometry properties

Material Properties		Geometry Properties	
Elastic Modulus (GPa)	2	Length (mm)	61
Capacitance (nF)	2.8	Width (mm)	12
Electrical Permittivity (F/m)	155×10^{-12}	Thickness (μm)	28

Figure 3-30 displays the output piezoelectric voltages generated by the PVDF vibrators attached to both notched and uniform cross-section beams, as well as the applied axial forces. The successive voltage output events are generated by the snap-through of the strip at mode transitions, accompanied by a slight drop in the force levels. The figure shows that when using an optimized configuration, the output voltage is higher and the harvester is able to freely vibrate. On the other hand, the uniform cross section configuration does not display the same behavior. The reason could be that the snapping point does not coincide with the location of the piezoelectric harvester, and therefore the latter is subjected to some sort of twisting due to the section rotation. Table 3-8 presents the maximum output voltages and energies generated using the designed notched and uniform prismatic beams. Output voltage differences of 60% and 73% were recorded at transitions Φ3 and Φ5, respectively. More importantly, the difference of the output energy is 78.57%. These results demonstrate that the energy conversion efficiency of the energy harvesting mechanism can be significantly enhanced by adopting an optimized non-prismatic beam configuration

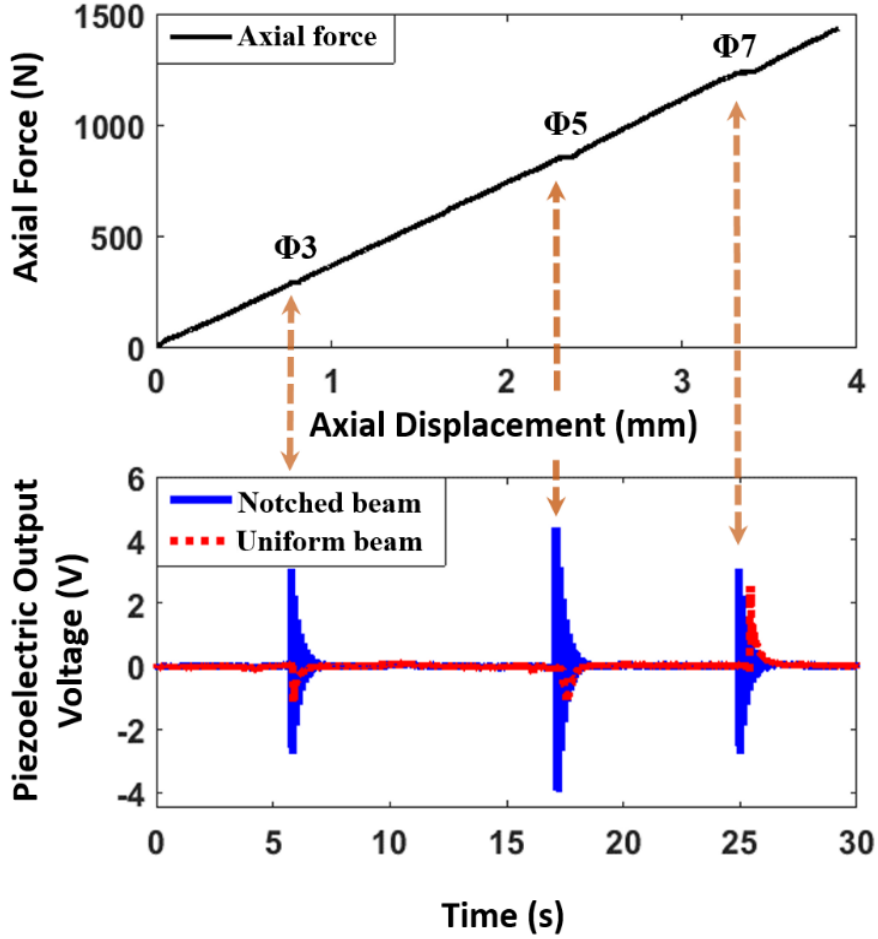

Figure 3-30. Piezoelectric output voltages generated using the notched and uniform cross section beams.

Table 3-8. Piezoelectric output voltages and energies.

		Notched Beam	Uniform Beam	Difference (%)
Voltage (V)	Φ_3	3.13	-1.26	59.74
	Φ_5	4.27	-1.14	73.3
	Φ_7	3.08	2.89	6.17
Energy (μJ)		0.0422	0.0098	**78.57**

3.6. Summary

The main objective of this work was to amplify the levels of the harvestable energy by controlling the snap-through transitions of the energy conversion mechanism. The mechanism consisted of a bilaterally constrained axially loaded beam with an attached piezoelectric energy harvester. Under a quasi-statically increasing axial load, the beam snapped between buckling mode configurations driving the harvester into free vibration. Since prismatic cross-section beams provided a limited control over the beam's response, this chapter investigated the use of non-prismatic beams as a solution to control the spacing and location of the snap-through transitions.

Using an energy method, an experimentally validated theoretical model was developed to simulate the post-buckling response of non-uniform beam configurations. A buckling analysis was firstly carried out to determine the buckling mode shapes of non-prismatic beams. The use of these buckling mode shapes instead of the uniform mode shapes increases the accuracy of the model. The model was then used to study the effect of multiple non-uniform cross-section configurations and geometry dimensions on the snap-through location of the beam. In particular, optimal designs were presented with respect to the shape and dimensions of the beams for more efficient energy conversion. By optimizing the buckling element, the harvestable power were significantly increased than a uniform prismatic beam.

CHAPTER 4

POST-BUCKLING RESPONSE OF BILATERALLY CONSTRINED BEAMS USING LARGE DEFORMATION THEORY

4.1. Overview

Post-buckling response has performed competitive applications in the fields of bistable and multistable systems, namely actuation, remote sensing, or energy harvesting. Among these applications, the mode transition of post-buckling response is particularly used in the mechanisms such that the stored strain energy can be released to kinetic energy. Through the process, the low-rate and low-frequency excitations are transformed into high-rate motions that generates electrical power on piezoelectric transducers. Therefore, it is of critical research interest to conduct a post-buckling analysis regarding buckling snap-through. This paper develops a large deformation model to investigate the post-buckling response of a bilaterally constrained beam subjected to a quasi-static axial force. The rotation-based equilibrium equations are formulated for the system based on the nonlinear Euler-Bernoulli beam theory. An energy method is used to solve the equations by minimizing the total potential energy under the constraints of bilateral boundaries. The presented large deformation model satisfactorily measures the post-buckling behavior of the bilaterally constrained beam in terms of both the shape deformation and force-displacement relationship. The theoretical model sufficiently captures the beam end shortening and deformation angle under different buckling modes, particularly higher modes such as Φ3 and Φ5. This is overlooked by previous models. The proposed model is validated with both an existing small deformation model and experimental results with respected to beam shape deflection and force-displacement relationship. Good agreements are achieved. It is indicated that the presented large deformation model is effective in understanding and predicting the post-buckling response of a bilaterally constrained beam.

4.2. Introduction

The analysis of buckling and post-buckling response of a variety of structures have been extensively studied. Particularly, research interests have been emphasized on the "smart applications" of buckling response – the potential of using buckling behavior to deploy and activate structures in many applications, i.e. MEMS or energy harvesting device for self-powered devices (Lajnef et al., 2014; Alavi et al., 2017).

In order to theoretically identify the post-buckling response of slender beams, many theories have been developed. Howell and Midha (1995) numerically solved the buckling instability of a tip loaded cantilever beam under large deformation assumptions. Beam tip rotation is presented with respect to critical buckling load. Lee (2002) and Shvartsman (2007) presented theoretical models to study the large deflection behavior of non-uniform cantilever beam under tip load. Zhao et al. (2008) have developed a theoretical model to determine the response of a polynomial curved beam under gradually increased external forces. A finite-deformation theory was developed by Song et al. (2008) to investigate the behavior of thin buckled films on compliant substrates. Solano-Carrillo (2009) theoretically solved the large-deformed buckling response of cantilever beams under both tip and uniformly distributed loads. Santos and Gao (2011) presented a canonical dual mixed numerical method for post-buckling analysis of elastic beams under large deformation assumptions. A theoretical model is developed by Jiao et al. (2012) and Chen et al. (2013) to measure the local buckling behavior of an I-beam with sinusoidal web geometry. Sofiyev (2014) studied the large deformation performance of truncated conical shells under time dependent axial loads using superposition principle and Galerkin procedure. Bigoni (2012) and Bosi et al. (2015) theoretically and numerically examined the injection of an elastic rod with gradually increased length. Buckling analysis is carried out based on the total potential energy of the system. Geometric equilibrium equations are used to solve for the critical buckling load. However, those theoretical models and numerical solutions did not take into account the constraints along the beam length. Therefore, only the first buckling mode deflection is measured.

A variety of constraints along beam length are added to achieve higher buckling modes beyond the bistable configurations. Due to the control in the transverse direction, the slender beam buckles to the first mode until it touches the constraints. Increasing the external force, the system jumps through a suddenly unstable status to reach the steady third buckling mode, and thereby regaining stiffness for greater loading. Many geometric assumptions have taken into account in the previous theoretical studies to measure such post-buckling response. Chai (1998) presented a theoretical model to study large rotations that occur to a bilaterally constrained beam subjected to an axial force. Geometric equilibrium is applied to the model to achieve large end-shortening that caused by buckling deformation. The model accurately predicts different buckling statuses, i.e. point touching that deformed beam touches the lateral constraints, and flattening that the touching point increases to a flattening line contact. Under the assumption that the gap between the bilateral constraints is not smaller than a certain value, however, the large deformation model is limited to only the first buckling mode, which does not take into account buckling mode transition. Srivastava and Hui (2013; 2013) theoretically studied both the adhesionless and adhesive contacts of a pressurized neo-Hookean plane-strain membrane against a rigid substrate under large deformation assumptions. Katz and Givil (2015) theoretically studied the post-buckling response of a beam subjected to bilateral constraints, i.e. one fixed wall and one springy wall that moves laterally against a spring. Geometric compatibility is used to solve the governing equations under both small and large deformation assumptions. However, the theoretical model sufficiently captures the system stiffness but the mode transition is increasingly overestimated that leads to progressively inaccuracy as the system snaps into higher buckling mode (Borchani et al. 2015). Lajnef et al. (2014) and Borchani et al. (2014; 2015) developed a theoretical model to measure a slender beam under both fixed, bilateral constraints under small deformation assumptions. Jiao et al. (2017) expended the theoretical model to non-uniform beam configurations such that the post-buckling response can be effectively controlled and tuned. Due to the orthogonality of the general solution, the superposition method is used to achieve a mode function that linearly combines different buckling modes. An energy method is used to minimize the total potential energy of the system, such that to determine the coefficients that define the contribution of each buckling mode. This model sufficiently measures the deformed buckling shapes of the beam, particularly for higher buckling modes at different loading states, namely modes 5 and 7. Under the assumptions of small deformation, however, the model neglects the deformation in the longitudinal direction.

This paper develops a theoretical model to predict the post-buckling behavior of a bilaterally constrained beam subjected to a gradually increased axial force under large deformation assumptions. The primary objective of this study is to present a model that accurately captures the buckling mode transitions, force-displacement response, and deflected configurations of the beam in different buckling modes. The presented model takes into account the impact of the gap between the bilateral constraints on the post-buckling response. If the gap is small comparing to the beam length, the system buckles and snaps into higher modes under compressive load. The end-shortening of the deflected beam is negligible, and hence small deformation presented by Borchani et al. (2015) is sufficient to predict the behavior. Increasing the gap, however, the beam end-shortening is critically increased, which also significantly delays buckling mode transition. In particular, if the gap is adequately large, the beam only buckles to the first mode with severe end-shortening and deformation. In this case, the end-shortening of the deformed beam has to be considered. The presented large deformation model is able to accurately capture the post-buckling behavior of a slender beam under different constraint scenarios. Based on the proposed model, the buckling mode transition is satisfactorily measured under a small constraint gap, especially for higher buckling mode. When the gap is large, the model also captures the deformation of the beam shape configuration in the first mode with acute end-shortening. The theoretical model developed in this study is based on the minimization of the total potential energy under the defined constraints, since the physical controls of the system can be mathematically calculated by finding the stable configuration with the minimum potential energy under such restrictions. Experiment is carried out to validate the presented model. Good agreements are obtained between the theoretical and testing results.

4.3. Problem Statement

The problem under consideration contains an initially straight slender beam subjected to a gradually increased axial force, $\hat{p}$, as shown in Figure 4-1. Figure 4-1(a) presents the bilaterally constrained beam under clamped-clamped boundary conditions, and Figure 4-1(b) shows the case under simply supported boundary conditions. The beams in the two cases have the same geometry and material properties as: a length, L, a uniform cross-section, A, a constant moment of inertia, I, and Young's modulus, E. The slender beam is placed between two frictionless rigid constraints with a constant gap, h. Increasing the axial force, the beam starts buckling to the first mode. Due to the bilateral constraints, the deformed beam tends to snap to higher buckling mode, rather than maintaining to the first mode only.

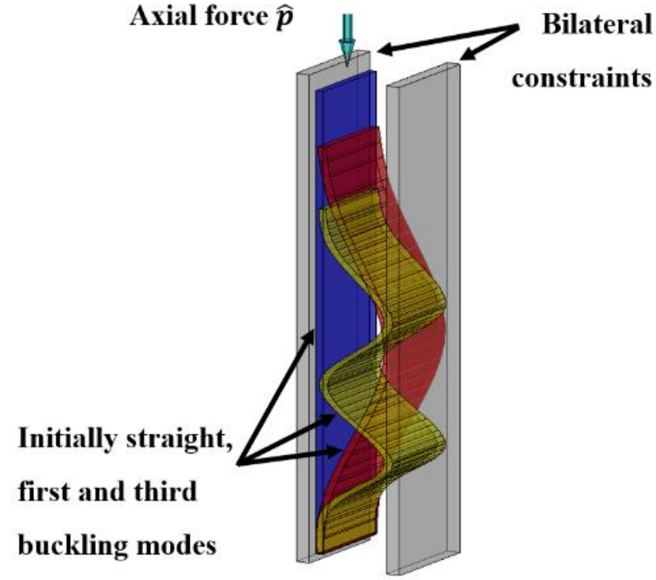

(a)

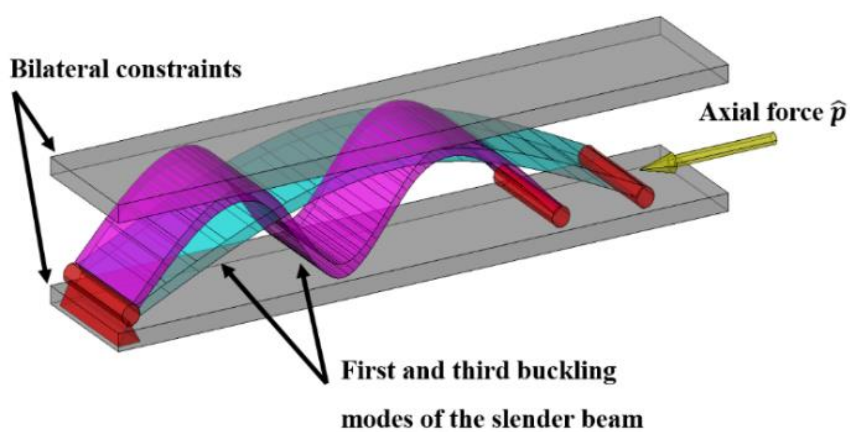

(b)

Figure 4-1. Schematic of bilaterally constrained (a) fixed-fixed and (b) simply supported beams under an axial force.

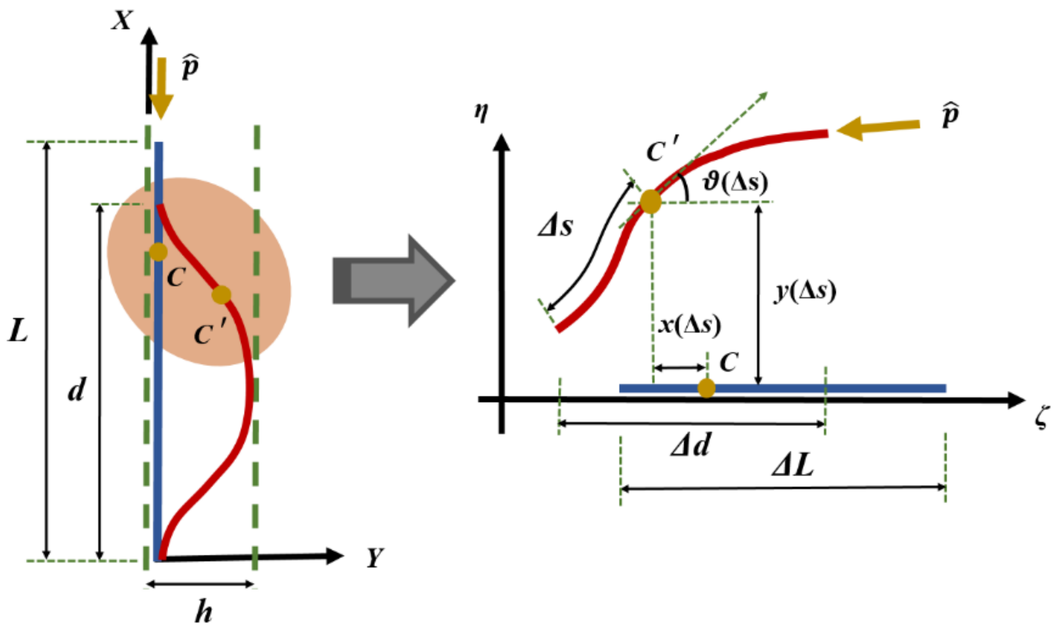

Figure 4-2. Segment diagram of the deformed beam by using the large deformation model.

4.4. Large Deformation Model of Clamped-Clamped Beams

4.4.1. Post-Buckling Analysis

Figure 4-2 displays the diagram of a deformed beam segment for the large deformation model. It can be seen that the location of a random point, *C*, on the initially straight beam is deformed to *C*' under the gradually increased axial force, $\hat{p}$. In order to investigate the deformation, the segment is considered in a locally curvilinear coordinate $\zeta - \eta$. The components of the deformation in ζ and η directions as well as the rotation angle of *C*' are defined as $x(\Delta s)$, $y(\Delta s)$, and $\vartheta(\Delta s)$, respectively. Since the deformed beam is assumed to be uniform, continuous and inextensible, the segment in the local coordinate can be applied to the entire beam length, namely $\Delta s \in [0 - L]$. Considering the deflected shape configuration of the system, it is found that the maximum deformed rotation angle, α, happens at,

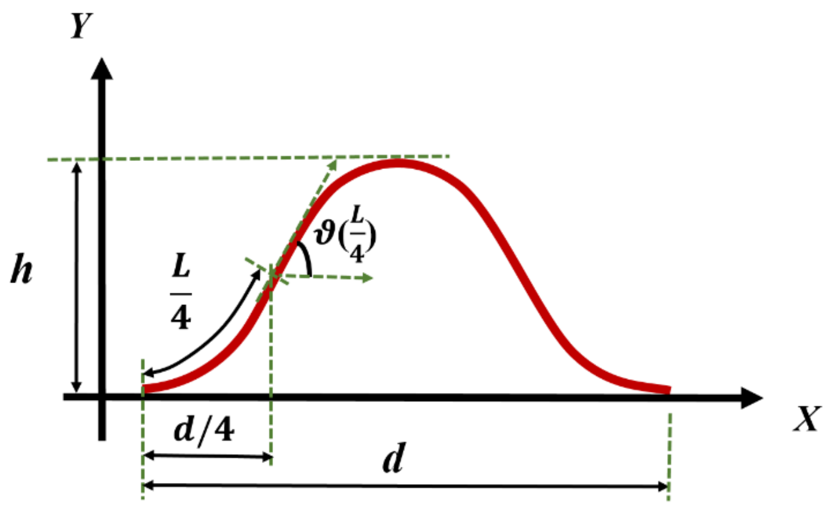

Figure 4-3. Maximum deformation angle of the deformed beam.

$$\mathrm{Max}[\vartheta(s)] = \alpha = \vartheta(s)|_{S=\frac{L}{4},\ \frac{3L}{4}} \tag{4-1}$$

Due to the symmetry of the deflected beam configuration, only $\vartheta(s)|_{S=\frac{L}{4}}$ has been taken into account in this study, as shown in Figure 4-3. The fixed-fixed slender beam can be formulated as a non-linear eigenvalue problem, and thus the normalized governing equations of the system yield,

$$\frac{d^2\theta(S)}{dS^2} + N^2 \sin[\theta(S)] = 0 \tag{4-2a}$$

$$\begin{cases} Y(0) = Y(1) = 0 \\ \theta(S)|_{S=0} = 0 \\ \left.\dfrac{d\theta(S)}{dS}\right|_{S=\frac{1}{4}} = 0 \end{cases} \tag{4-2b}$$

where $N = \sqrt{\frac{\hat{p}}{EI}}$ represents the normalized axial force placed to the deflected beam.

The non-dimensional factors are given as,

$$\begin{cases} S = \dfrac{s}{L} \\ \theta(S) = \vartheta(SL) \\ X(S) = \dfrac{x(SL)}{L} \\ Y(S) = \dfrac{y(SL)}{h} \end{cases} \tag{4-3}$$

Note that a trivial solution, $\theta(S) = 0$, always exists in Eq. (4-2). Therefore, the problem can be identified as solving for the non-trivial solution. Introducing the Jacobi amplitude function, $\Phi(S)$, a relationship is assumed as,

$$\sin\left[\frac{\theta(S)}{2}\right] = k\sin[\Phi(S)] \tag{4-4}$$

In addition, the following identities are applied in this study,

$$\begin{cases} \Phi(0) = \mathbf{am}[0, k] = 0 \\ \Phi\left(\dfrac{1}{4}\right) = \mathbf{am}\left[\dfrac{1}{4}, k\right] = \dfrac{\pi}{2} \\ k = \sin(\alpha) \end{cases} \tag{4-5}$$

where k is defined based on the maximum deformation angle, α.

According to Eq. (4-4), the rotation angle, $\theta(S)$, may be written as,

$$\theta(S) = 2\arcsin[k\sin[\Phi(S)]] \tag{4-6}$$

Multiplying Eq. (4-2a) by $\frac{d\theta(S)}{dS}$ and substituting into Eq. (4-4), leading through trigonometric derivations, we obtained,

$$\frac{d[\Phi(S)]}{dS} = N\sqrt{1 - k^2 \sin^2[\Phi(S)])} \tag{4-7}$$

Separating the variables and integrating Eq. (4-7) yields,

$$SN = \int_{\frac{2m+1}{2}\pi}^{\Phi(S)} \frac{1}{\sqrt{1 - k^2 \sin^2[\Phi(S)])}} d\Phi \tag{4-8}$$

where $m = 0, \pm 1, \pm 2, ...$

According to the discussion regarding Eq. (4-1), only $\frac{1}{4}$ of the beam length has taken into account in this study, namely $S = \frac{1}{4}$. Therefore, Eq. (4-8) can be rewritten as,

$$\frac{N}{4} = \int_{\frac{2m+1}{2}\pi}^{\frac{a+1}{2}\pi} \frac{1}{\sqrt{1 - k^2 \sin^2[\Phi(S)])}} d\Phi \tag{4-9}$$

where $a = 0, \pm 1, \pm 2, ...$ Eq. (4-9) represents a function of *m* as,

$$N = 4m\,\mathbf{K}(k) \tag{4-10}$$

where **K**(*k*) is the complete elliptic integral function of the first kind at $\Phi = \frac{\pi}{2}$ as,

$$\mathbf{K}(k) = \int_{0}^{\frac{\pi}{2}} \frac{1}{\sqrt{1 - k^2 \sin^2[\Phi(S)])}} d\Phi \tag{4-11}$$

Note that the integration of Eq. (4-8) can be expressed as,

$$SN = \Gamma_1 - \Gamma_2 \tag{4-12}$$

where

$$\begin{cases} \Gamma_1 = \displaystyle\int_0^{\Phi(S)} \frac{1}{\sqrt{1 - k^2 \sin^2[\Phi(S)]\text{)}}} d\Phi \\ \Gamma_2 = \displaystyle\int_0^{\frac{2m+1}{2}\pi} \frac{1}{\sqrt{1 - k^2 \sin^2[\Phi(S)]\text{)}}} d\Phi \end{cases} \tag{4-13}$$

Substituting Eqs. (4-12) and (4-13) into Eq. (4-9), we obtained,

$$SN + \Gamma_2 = \Gamma_1 \tag{4-14}$$

where yields

$$SN + (2m+1)\mathbf{K} = \int_0^{\Phi(S)} \frac{1}{\sqrt{1 - k^2 \sin^2[\Phi(S)]\text{)}}} d\Phi \tag{4-15}$$

Eq. (4-15) refers to,

$$\Phi(S) = \mathbf{am}[SN + (2m+1)\ \mathbf{K}, k] \tag{4-16}$$

According to the property of the Jacobi amplitude function, Eq. (4-16) yields,

$$\Phi(S) = \mathbf{am}[SN, k] + (2m+1)\pi \tag{4-17}$$

Substituting Eq. (4-10) into Eq. (4-17), we simplified and obtained,

$$\Phi(S) = \mathbf{am}[4mS\mathbf{K}, k] \tag{4-18}$$

where $m = 1,2,3, \ldots$ refers to the buckling mode of the system, $\mathbf{K}(k)$ represents the complete elliptic integral function of the first kind at $\Phi = \frac{\pi}{2}$.

Taking Eq. (4-18) into Eq. (4-6), the rotation angel, $\theta(S)$, can be rewritten as,

$$\theta(S) = 2\arcsin\left[k\ \mathbf{sn}[4mS\mathbf{K}, k]\right] \tag{4-19}$$

where **sn** denotes the Jacobi sine amplitude function. In order to predict the deformed shape of the slender beam, it is of interest to obtain the X and Y components of the displacement, namely $X(S)$ and $Y(S)$. It can be seen in Figure 4-2 that the differential equations define the changes of the components are given as,

$$\frac{dX(S)}{dS} = \cos[\theta(S)] \tag{4-20a}$$

$$\frac{dY(S)}{dS} = \sin[\theta(S)] \tag{4-20b}$$

and, hence, the displacements in the longitudinal and transverse directions can be expressed as,

$$X(S) = \int_0^S \cos[\theta(S)]\, dS \tag{4-21a}$$

$$Y(S) = \int_0^S \sin[\theta(S)]\, dS \tag{4-21b}$$

where $s \in [0-1]$.

Since the buckling modes calculated in Eq. (4-19) consist of an orthogonal basis, the superposition method is applied to the model. Taking Eq. (4-19) into Eq. (4-21), leading through trigonometric derivations, $X(S)$ and $Y(S)$ can be written as,

$$X(S) = \sum_{m=1}^{\infty} A_m \left[S - \frac{1}{2m\,\mathbf{K}}\,\mathbf{E}[\mathbf{am}[4mS\mathbf{K}, k], k] \right] \tag{4-22a}$$

$$Y(S) = \sum_{m=1}^{\infty} A_m \left[-\frac{Lk}{2mh\,\mathbf{K}} [1 - \mathbf{cn}[4mS\mathbf{K}, k]] \right] \tag{4-22b}$$

where A_m represents the weight coefficients that determine the contribution of each buckling mode to the beam deformation, **cn** stands for the Jacobi cosine amplitude function, and **E** refers to the incomplete elliptic integral function of the second kind.

In order to determine the deformed shape configuration of the slender beam described in Eq. (4-22), the only unknowns, A_m, need to be solved with respect to different buckling mode. Therefore, the total potential energy of the system needs to be minimized.

4.4.2. Energy Analysis

The normalized projection of the deformed beam in the longitudinal direction, *d*, can be calculated as,

$$d = \int_0^1 \sqrt{1 - \left[\frac{dY(S)}{dS}\right]^2}\, dS = \int_0^1 \cos[\theta(S)] dS \tag{4-23}$$

Therefore, the deformation in *X* direction yields,

$$\mathit{\Delta} = 1 - d = 1 - \int_0^1 \cos[\theta(S)]\, dS \tag{4-24}$$

The total potential energy in the system, Π, is defined as the summation of the deformed beam's elastic energy and the work contributed by the external force, $\hat{p}$. The normalized total potential energy is,

$$\Pi_{\text{norm}} = \underbrace{\frac{1}{2}\int_0^1 \left[\frac{d\theta(S)}{dS}\right]^2 dS}_{\text{Elastic energy}} - \underbrace{\frac{1}{2}P\mathit{\Delta}}_{\text{External work}} \tag{4-25}$$

where the non-dimensional factors are,

$$\begin{cases} \Pi_{\text{norm}} = \dfrac{L^3}{EIh^2}\Pi \\ P = \dfrac{L^2}{EI}\hat{p} \end{cases} \tag{4-26}$$

Substituting Eq. (4-19) into Eq. (4-25), the elastic energy and external work terms of the total potential energy become,

$$\cos[\theta(S)] = \sum_{m=1}^{\infty} A_m{}^2[1 - 2k^2\, \mathbf{sn}[4mS\mathbf{K}, k]^2] \tag{4-27a}$$

$$\frac{d\theta(S)}{dS} = 8k\mathbf{K}\sum_{m=1}^{\infty}\left[\frac{A_m m\ \mathbf{cn}[4mS\mathbf{K}, k]}{\sqrt{1 - k^2\, \mathbf{sn}[4mS\mathbf{K}, k]^2}}\ \mathbf{dn}[4mS\mathbf{K}, k]\right] \tag{4-27b}$$

where **dn** represents the Jacobi elliptic function. Substituting Eq. (4-27) into Eq. (4-25), the normalized total potential energy can eventually be written as,

$$\Pi_{\text{norm}} = 32k^2\,\mathbf{K}^2 \sum_{m=1}^{\infty} {A_m}^2 m^2 \int_0^1 \frac{\mathbf{cn}[4mS\mathbf{K},k]^2}{1-k^2\,\mathbf{sn}[4mS\mathbf{K},k]^2}\,\mathbf{dn}[4mS\mathbf{K},k]^2\,dS - Pk^2 \sum_{m=1}^{\infty} {A_m}^2 \int_0^1 \mathbf{sn}[4mS\mathbf{K},k]^2 dS \tag{4-28}$$

The total potential energy presented in Eq. (4-28) is then minimized with respect to A_m. Since the bilateral constraints allow the deflected beam to buckle into higher modes, the constant gap between the rigid walls, h, is considered as the normalized boundary condition for the transverse deflection of the beam, namely $Y(S) \in [0-1]$. The snap-through transitions of the beam shape from lower to higher buckling modes are then induced when the total potential energy, Π_{norm}, jumps through an unstable path to achieve the most “temporarily appropriate” stable shape configuration with the minimum value. Therefore, the constrained minimization problem of the total potential energy for the system can be written as,

$$\begin{cases} Min\ [\Pi_{\text{norm}}(A_m)] \\ \quad 0 \le Y(S) \le 1 \end{cases} \tag{4-29}$$

The coefficients, A_m, determined in Eq. (4-29) provide an accurate representation of the beam deflected configuration at each loading state. Taking the coefficients into Eq. (4-22), the beam deformation at each buckling mode can be predicted.

4.5. Large Deformation Model of Simply Supported Beams

4.5.1. Post-Buckling Analysis

Figure 4-4 displays the diagram of a deformed beam segment for the nonlinear large deformation model. The location of a random point, *A*, on the initially straight beam is deformed to *A*'. Similarly to the clamped-clamped beam in Figure 4-2, the segment is considered in a locally curvilinear coordinate $\zeta-\eta$. The simply supported beam can, therefore, be described as a non-linear eigenvalue problem. Therefore, the normalized governing equations of the system yields,

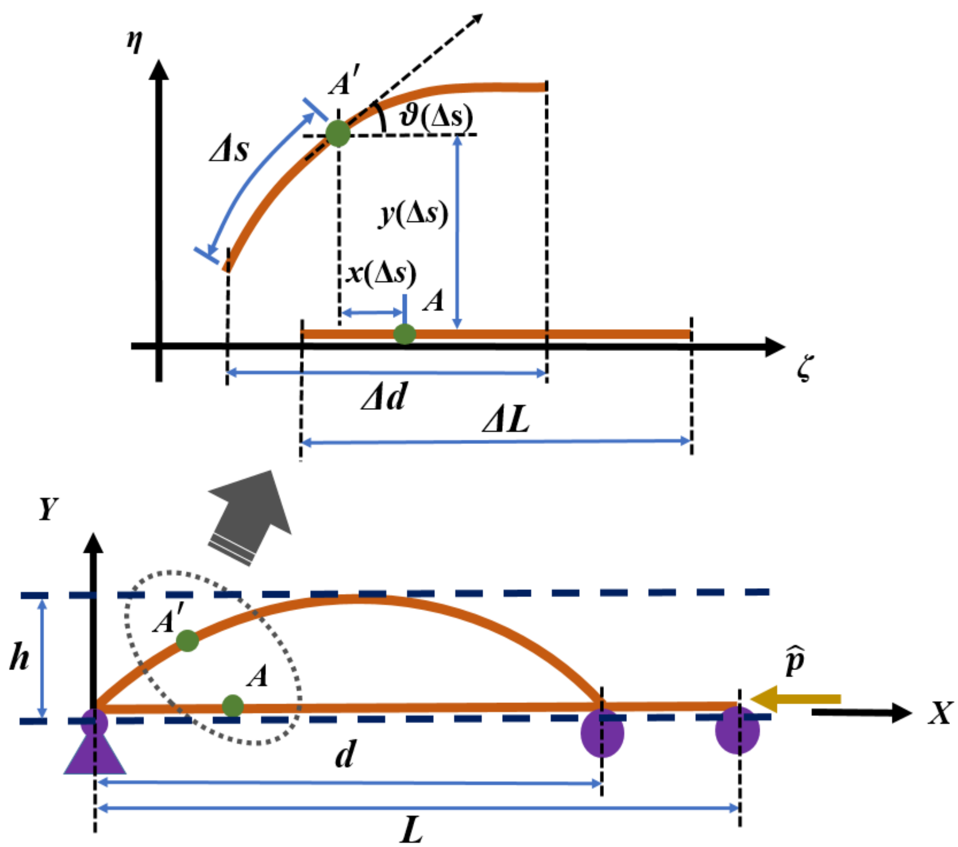

Figure 4-4. Segment diagram of the deformed beam by using the nonlinear large deformation model.

$$\frac{d^2\theta(S)}{dS^2} + N^2 \sin[\theta(S)] = 0 \tag{4-30a}$$

$$\begin{cases} Y(0) = Y(1) = 0 \\ \left.\frac{d\theta(S)}{dS}\right|_{S=0} = \left.\frac{d\theta(S)}{dS}\right|_{S=1} = 0 \end{cases} \tag{4-30b}$$

where $N = \sqrt{\hat{p}/EI}$. Note that the governing equation in Eq. (4-30a) is the same as Eq. (4-2a), however, the boundary conditions in Eq. (4-30b) are defined differently.

Similarly to Eq. (4-6), the rotation angle, $\theta(S)$, of the deflected simply supported beam is given as,

$$\theta(S) = 2\mathrm{arcsin}\big[k\ \mathbf{sn}[(2mS + 1)\mathbf{K}, k]\big] \tag{4-31}$$

Taking Eq. (4-31) into Eq. (4-21), the X and Y components of the beam can be obtained. Therefore, the normalized displacements in the longitudinal and transverse directions, following the principles in an orthogonal basis as Eq. (4-22), are written as,

$$X(S) = \sum_{m=1}^{\infty} A_m \left[-S + \frac{1}{m\,\mathbf{K}}\Big[\mathbf{E}\big[\mathbf{am}[(2mS + 1)\ \mathbf{K}, k]\big] - \mathbf{E}\big[\mathbf{am}[\mathbf{K}, k]\big]\Big]\right] \tag{4-32a}$$

$$Y(S) = \sum_{m=1}^{\infty} A_m \left[-\frac{Lk}{mh\,\mathbf{K}}\ \mathbf{cn}[(2mS + 1)\ \mathbf{K}, k]\right] \tag{4-32b}$$

where A_m represent the weight coefficients that determine the contribution of each buckling mode, m, to the beam deformation.

4.5.2. Energy Analysis

The total potential energy in the system, Π, is calculated as the summation of the elastic energy of the deformed beam and the work contributed by the external force, $\hat{p}$, as given in Eq. (4-25). Substituting Eq. (4-32) into Eq. (4-25), the normalized total potential energy can be written as,

$$\begin{aligned}\Pi_{\text{norm}} &= 8\,\mathbf{K}^2 k^2 \sum_{m=1}^{\infty} {A_m}^2 m^2 \int_0^1 \mathbf{cn}[(2mS+1)\,\mathbf{K}, k]^2 dS \\ &- Pk^2 \sum_{m=1}^{\infty} {A_m}^2 \int_0^1 \mathbf{sn}[(2mS+1)\,\mathbf{K}, k]^2 dS\end{aligned} \tag{4-33}$$

Taking Eq. (4-33) into the constrained minimization problem defined in Eq. (4-29), the coefficients, A_m, can be determined. Taking the coefficients into Eq. (4-32), the beam deformation at each buckling mode can be predicted.

4.6. Model Validation

4.6.1. Validation of Clamped-Clamped, Large Deformation Model

4.6.1.1. Validation with Small Deformation Model

The theoretical model developed in Section 3.2 is reduced to uniform beams and compared with the presented large deformation model. The geometry and material properties of the system are summarized in Table 4-1.

Table 4-1. Geometry and material properties of the small deformation model.

Beam Length (mm)	250
Beam Thickness (mm)	2.34
Beam Width (mm)	30
Young's Modulus (GPa)	2.3

The axial force-displacement relationship by the presented model is validated with the small deformation model. Two gaps are investigated, namely 20 mm and 50 mm. Figure 4-5 displays the comparisons. It is shown in Figure 4-5(a) that the post-buckling response predicted by the two theoretical models have sufficient agreements. The slopes of the curvilinear relationship generated by the large deformation model, which represents the stiffness of the system, satisfactorily matches the results based on the existing small deformation model. Particularly, the maximum differences of 2.73% and 3.64%, in terms of axial forces, are measured at mode transitions Φ3 and Φ5, respectively. Figure 4-5(b) indicates that the maximum differences between the two models with the gap of 50 mm. Note that only Φ3 is achieved, with a difference of 2%, since $\frac{h}{L} = 0.2$, the physical length of the beam does not meet the request for Φ5 between the gap.

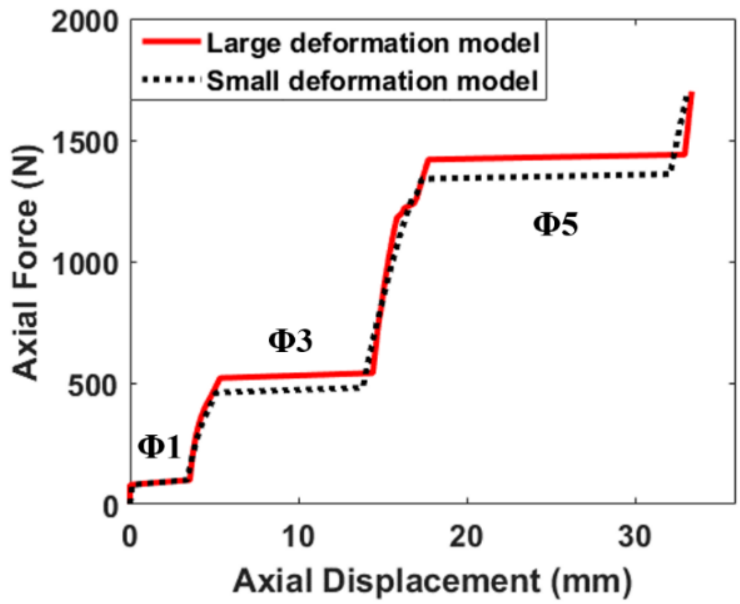

(a)

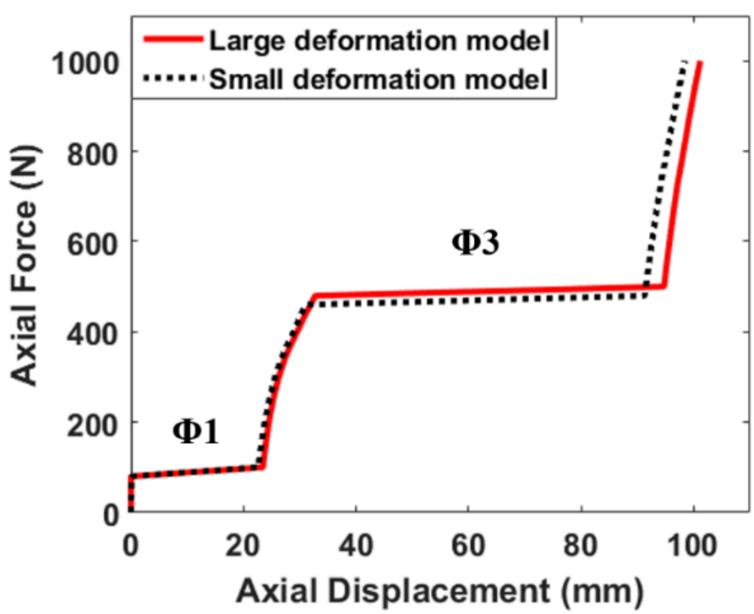

(b)

Figure 4-5. Comparison of the axial force and displacement response between the presented large and small deformation models with gaps of (a) 20 mm and (b) 50 mm.

According to Figure 4-5, it is concluded that the force-displacement relationship obtained from the large deformation model satisfactorily agree with the results by the existing small deformation model. In addition, increasing the gap between the bilateral constraints, the large deformation model captures the impact of $\frac{h}{L}$ on the buckling mode transition of the deformed beam. Figs. 4-6 and 4-7 show the normalized deflected beam shape configurations calculated by both the large and small deformation models. Two gaps are investigated, namely 20 mm and 100 mm. With the gap of 20 mm, both the large and small deformation models predict that the beam snaps into higher buckling modes when the axial force is gradually increased, rather than staying only to the first mode, as shown in Figure 4-6.

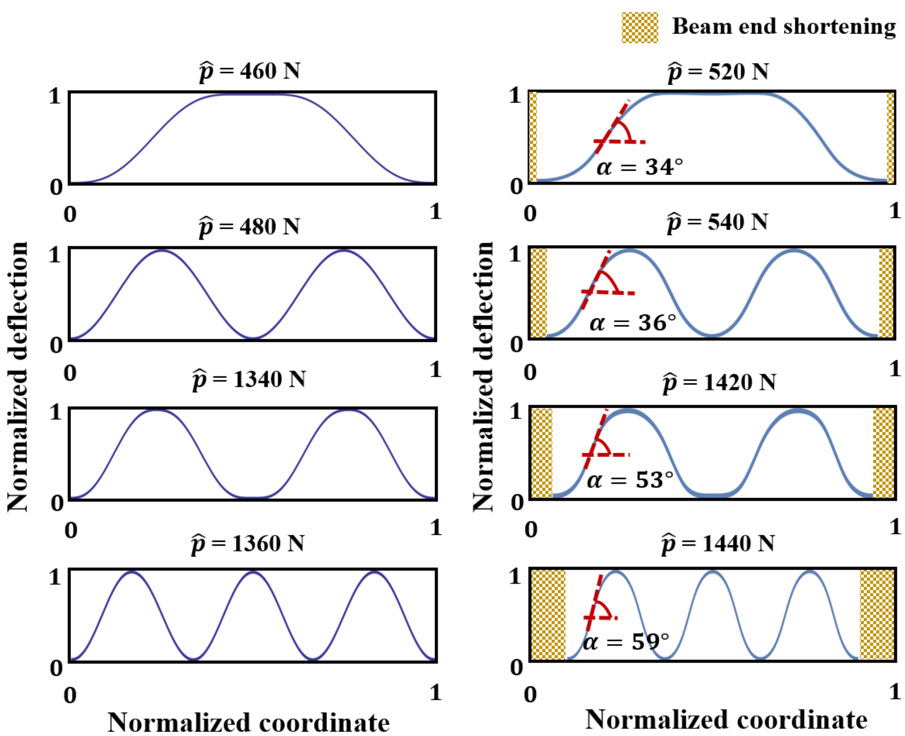

(a) (b)

Figure 4-6. Deflected shape configurations of a slender beam with a gap of 20 mm that determined by (a) the small deformation model and (b) the large deformation model.

Figure 4-6(a) displays the deformed shapes of the beam captured by the small deformation model. When the axial force, $\hat{p}$, is increased to 460 N, the beam flattens, and then snaps into the third mode with an force of $\hat{p} = 480$ N. Flattening regions are also found in the third mode when the axial force is $\hat{p} = 1340$ N, and then the shape snaps to the fifth mode ($\hat{p} = 1360$ N). Figure 4-6(b) indicates the results based on the presented large deformation model. When the axial force is $\hat{p} = 520$ N, the beam reaches the flattening limit, and then snaps into the third mode with an axial force of $\hat{p} = 540$ N. The maximum deformation angles, α, are $34°$ and $36°$ before and after the buckling mode transitions, respectively. Flattening limit is also found in the third mode when the axial force is $\hat{p} = 1420$ N, with a deformation angle of $\alpha = 53°$. The beam jumps into the fifth mode when the axial force is $\hat{\mathrm{p}} = 1440$ N and the deformation angle is $\alpha = 59°$. The beam end-shortenings in x direction are also highlighted in Figure 4-6(b). Comparing the results presented in Figure 4-6, measured by the large and small deformation models, it can be seen that the buckling mode transition of the slender beam under certain axial force can be sufficiently predicted by both the large and small deformation models. The large deformation model also satisfactorily captures the beam end-shortening and deformation angle, which, however, are lack of consideration in the small deformation model due to its fundamental assumptions. According to the large deformation model, when the beam snaps into higher buckling modes, the end-shortening is increased significantly, but the deformation angle does not perform critically extension. The beam shape configurations with a 100 mm gap are displayed in Figure 4-7. Since the gap is up to 40% of the beam length, the beam does not behave mode transitions, instead it stays in the first buckling mode. Figure 4-7(a) refers to the results from the small deformation model. It can be seen that when the axial force is 100 N, the beam buckles and touches the opposite constraints at a single point. The point contact is significantly increased when gradually increase the axial force. The results based on the large deformation model, as shown in Figure 4-7(b), indicate the same behavior. However, dramatically increasing of beam end-shortening and deformation angle are also achieved based on the presented model. In particular, the deformed beam behaves point contact when the axial force is 100 N and the deformation angle is $\alpha = 47°$. Increasing the axial force to 200 N, the touching point is widened to a flattening line contact, and the deformation angle is also enlarged to $\alpha = 61°$. The angle meets 90° when the axial force is increased to 250 N. Keep increasing the axial force to 310 N, the beam is crucially deflected with a deformation angle of $\alpha = 141°$.

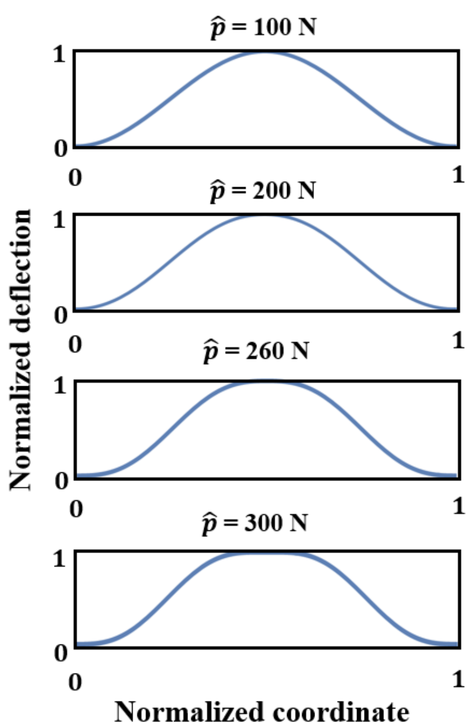

(a)

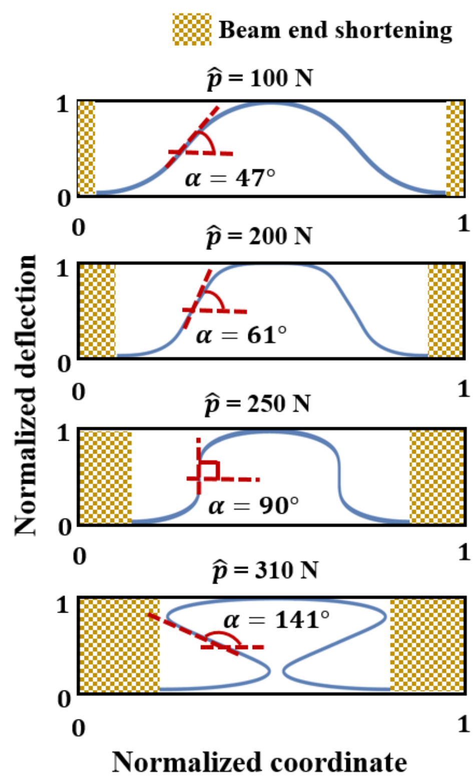

(b)

Figure 4-7. Deflected shape configurations of a slender beam with a gap of 100 mm that determined by (a) the small deformation model and (b) the large deformation model.

According to Figs. 4-6 and 4-7, we conclude that,

- The presented large deformation model sufficiently captures the buckling mode transition of a slender beam under a gradually increased axial force;
- The proposed model also accurately measures the end-shortening and deformation angle of the deflected beam, which are lack of consideration in the existing small deformation model; and
- The post-buckling response of the bilaterally constrained beam primarily depends on the gap between the constraints. In particular, when $\frac{h}{L}$ is small, the deflected beam snaps to higher buckling modes. However, the mode transition can be reduced to null when $\frac{h}{L}$ is increased.

4.6.1.2. Validation with Experiment

Experiment was conducted for a polycarbonate beam to validate the proposed large deformation model. The experimental setup and procedures followed the work presented in Lajnef et al. (2014). The beam with fixed-fixed end supports was placed between two rigid aluminum constraining walls. In particular, the testing sample was placed next to one wall, as shown in Figure 4-8. The gap separating the lateral constraints was fixed at 20 mm. The loading protocol consisted in applying a gradually increasing compressive force to the top of the beam using a universal mechanical testing frame. In order to highlight the deflected shapes of the tested specimens, the front edge of the specimen was painted in a fluorescent color. A black light was used to separate the beam from the ambience. The beam thickness was selected as 1 mm, and the beam length, width and Young's modulus were the same as the properties presented in Table 4-1.

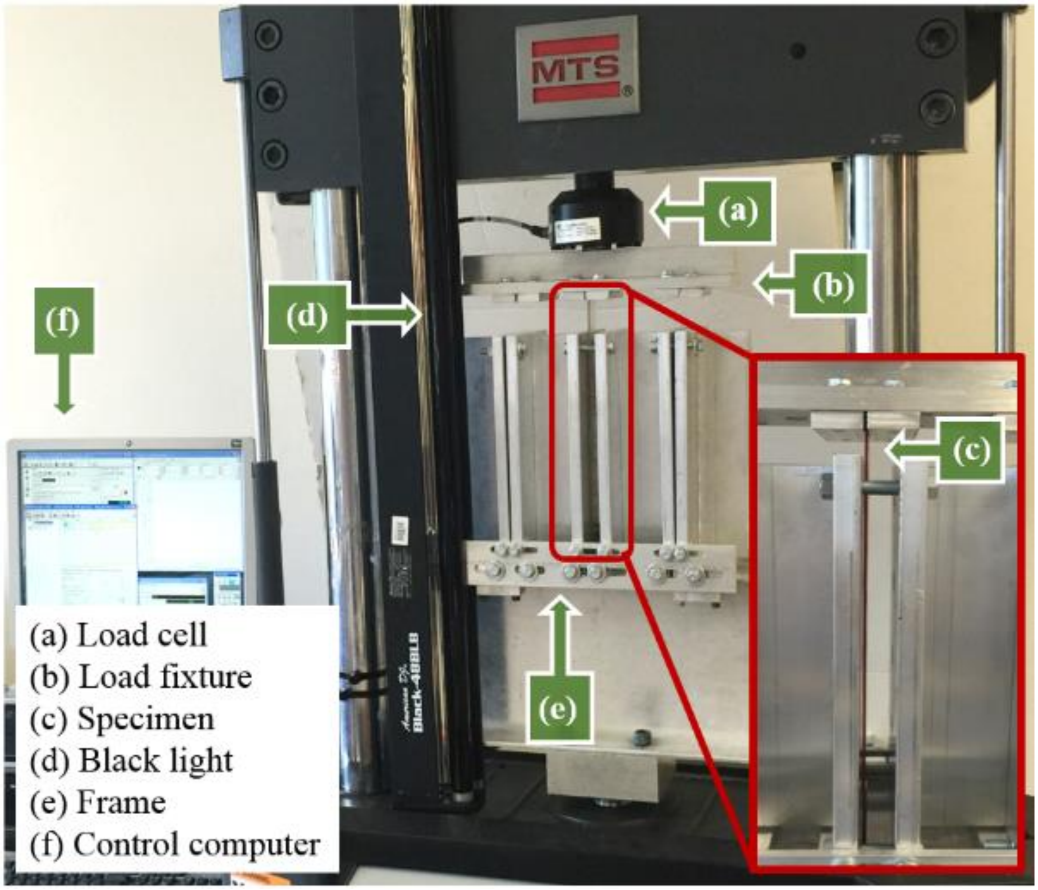

Figure 4-8. Experimental setup.

Figure 4-9 shows the deflected shapes of the beam that snapped from buckling mode Φ1 to Φ3 based on both the experimental and theoretical results. Different statuses of the deformed beam are experimentally investigated, as presented in Figure 4-9(a). Figure 4-9(b) displays the beam shape deformation obtained by the proposed theoretical model. It can be seen that the large deformation model accurately captures the deformed shapes of the slender beam at different buckling modes.

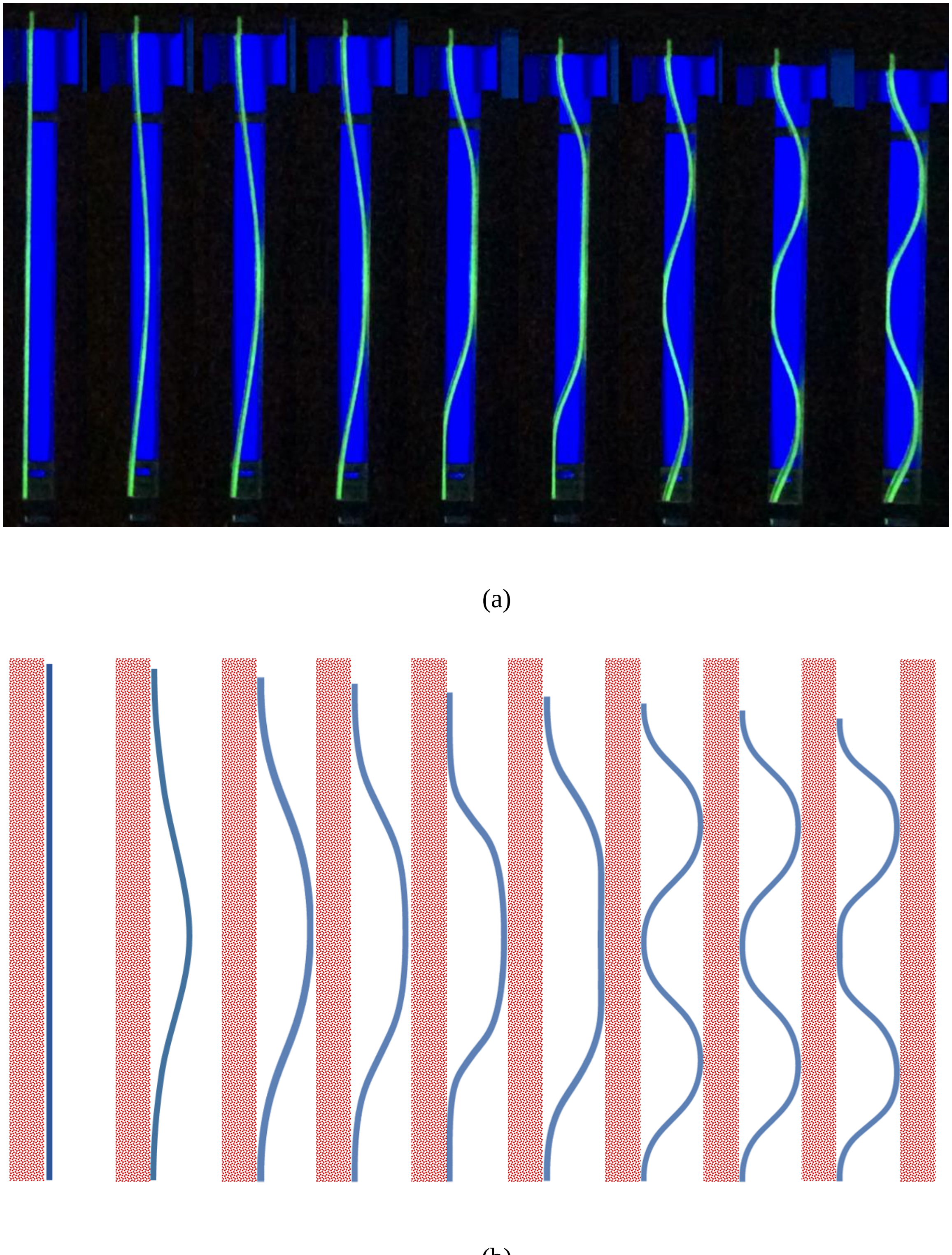

(a)

(b)

Figure 4-9. Deflected beam shape configurations from Φ1 to Φ3 based on (a) experimental and (b) theoretical results.

4.6.2. Validation of Simply Supported, Large Deformation Model

4.6.2.1. Validation with Theoretical Models

The presented large deformation model forms a nonlinear eigenvalue problem that takes into account the shape deflections with respect to both longitudinal and transverse displacements. Note that the theoretical model can be reduced and simplified to a linear eigenvalue problem by hypothesizing the longitudinal displacement, $X(S)$, is null. The normalized governing equations described in Eq. (4-2) can be reduced to a so-called "Sturm-Liouville problem" as,

$$\frac{d^2\theta(S)}{dS^2} + N^2\,\theta(S) = 0 \tag{4-34a}$$

$$\begin{cases} Y(0) = Y(1) = X(0) = X(1) = 0 \\ \left.\dfrac{d\theta(S)}{dS}\right|_{S=0} = \left.\dfrac{d\theta(S)}{dS}\right|_{S=1} = 0 \end{cases} \tag{4-34b}$$

Based on the orthogonal principle applied to Eq. (4-22), the general solutions of Eq. (4-34) can be written as,

$$\theta(S) = \sum_{m=1}^{\infty} A_m \cos[m\pi S] \tag{4-35a}$$

$$Y(S) = \sum_{m=1}^{\infty} A_m \frac{L}{hm\pi} \sin[m\pi S] \tag{4-35b}$$

Note that the total potential energy given by Eq. (4-25) is valid for all the deflected configurations that defined based on a normalized rotation angle $\theta(S)$, $S \in [0 - 1]$. Substituting

Eq. (4-35) into Eq. (4-25), the total potential energy can be calculated, with respect to the coefficients, A_m, as,

$$\Pi_{\mathrm{norm}} = \frac{\pi^2}{4}\sum_{m=1}^{\infty} {A_m}^2 m^2 - \frac{P}{8}\sum_{m=1}^{\infty} {A_m}^2 \tag{4-36}$$

Substituting Eq. (4-36) into the constrained minimization defined by Eq. (4-29), the coefficients, A_m, can be solved. Substituting the obtained coefficients into Eq. (4-35b), the deformed shape configurations of the beam can be determined.

In order to validate the presented model, the small deformation model developed in Section 3.2 is changed to simply supported boundary conditions as,

$$\frac{d^2W(X)}{dX^2} + N^2W(X) = 0 \tag{4-37a}$$

$$\begin{cases} W(0) = W(1) = 0 \\ \left.\dfrac{d^2W(X)}{dX^2}\right|_{X=0} = \left.\dfrac{d^2W(X)}{dX^2}\right|_{X=1} = 0 \end{cases} \tag{4-37b}$$

where

$$\begin{cases} X = \dfrac{x}{L} \\ W(X) = \dfrac{w(XL)}{h} \\ N = \sqrt{\dfrac{\hat{p}}{EI}} \end{cases} \tag{4-38}$$

In the orthogonal basis, the general solution of Eq. (4-37) is,

$$W(X) = \sum_{m=1}^{\infty} A_m \sin[N_m \pi X] \tag{4-39}$$

The normalized energies due to bending, compression, and external force, V_b, V_c, and V_p, respectively, are calculated as,

$$V_b = \frac{1}{2} \sum_{m=1}^{\infty} A_m{}^2 \int_0^1 \left[\frac{d^2 W_m(X)}{dX^2} \right]^2 dX \tag{4-40a}$$

$$V_c = -\frac{P^2 t^2}{24h^2} - \frac{P}{4} \sum_{m=1}^{\infty} A_m{}^2 \int_0^1 \left[\frac{dW_m(X)}{dX} \right]^2 dX \tag{4-40b}$$

$$V_p = \frac{P^2 t^2}{24h^2} \tag{4-40c}$$

The total potential energy of the system is written as the summation of the bending and compression energies, as well as external work, which yields,

$$\Pi_{\text{norm}} = V_b + V_c + V_p \tag{4-41}$$

Taking Eq. (4-34) into the constrained minimization in Eq. (4-29), the coefficients, A_m, can be calculated, which are substituted into Eq. (4-32) to determine the beam's deflected beam shapes.

Similar to Section 4.6.1.1, the linear large deformation and small deformation models are used to validate the force-displacement response of the presented nonlinear large deformation model. Same geometry properties are used as summarized in Table 4-1.

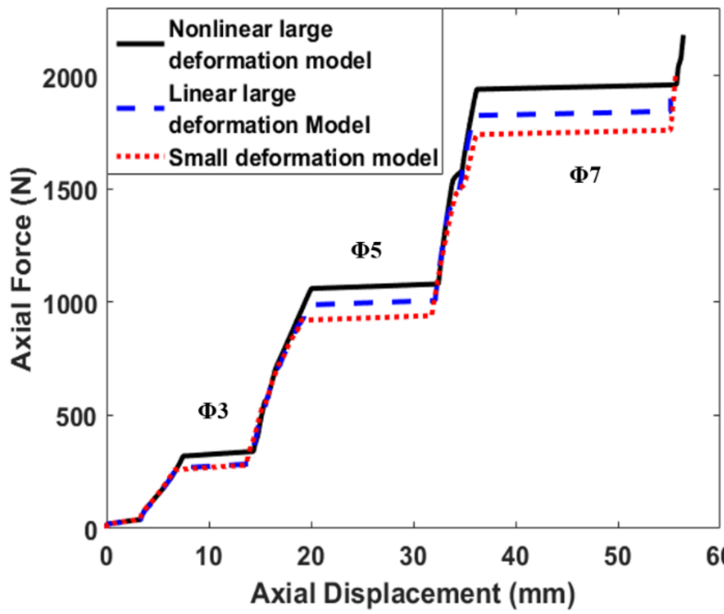

Figure 4-10. Comparison of the axial force and displacement relationship between the presented nonlinear large deformation model and existing models.

Figure 4-10 displays that the post-buckling response that predicted by the three theoretical models have satisfactory agreements. The maximum differences of 3.08%%, 5.45%, and 8.08%, in terms of axial forces, are measured at mode transitions Φ3, Φ5, and Φ7, respectively. Therefore, the presented nonlinear large deformation model can be used to investigate the post-buckling behavior of bilaterally constrained slender beams.

Figure 4-11 shows the normalized deflected beam shape configurations calculated by the presented large deformation model. Two gaps are investigated, namely 20 mm and 100 mm. The geometry and material properties of the system is summarized in Table 4-1. It can be seen that when the axial force is increased, the beam with a 20 mm gap snaps into higher buckling modes, rather than stays to the first mode, as shown in Figure 4-11(a). In particular, when the axial force is $\hat{p} = 320$ N, the beam reaches the flattening limit, and then snaps into the third mode with an axial force of $\hat{p} = 340$ N. The deformed angles, α, are $42°$ and $47°$ before and after the buckling mode transitions, respectively. Flattening limit is found in the third mode when the axial force is $\hat{p} = 1060$ N, with a deformed angle $\alpha = 56°$. The beam snaps to the fifth mode when $\hat{p} = 1080$ N and $\alpha = 61°$. In addition, the beam end shortenings in x direction are highlighted. It can be seen that when the beam snaps into higher buckling modes, the end shortening increases significantly. However, the deformed angle, α, does not perform critically extension. The beam shape configurations with a 100 mm gap are displayed in Figure 4-11(b). Since the gap is 80% of the beam's half-length, the beam does not behave mode transitions. Instead, it stays in the first buckling mode with dramatically increased deformed angles. In particular, when the axial force is 40 N, the beam buckles and touches the opposite constraints at a single point with a deformed angle of $\alpha = 46°$. Increasing the axial force to 100 N, the touching point is widened to a flattening line contact, and the deformed angle is also enlarged to $\alpha = 65°$. The angle meets 90° when the axial force is increased to 140 N, while the flattening zone is extended as well. Keep increasing the axial force to 160 N, the beam is crucially deflected with a deformed angle of $\alpha = 142°$. Comparing Figure 4-11(a) and (b), it can be seen that when increases the gap of the bilateral constraint, the buckling mode transition tends to be attenuated, but the end shortening of the deformed beam becomes more significant.

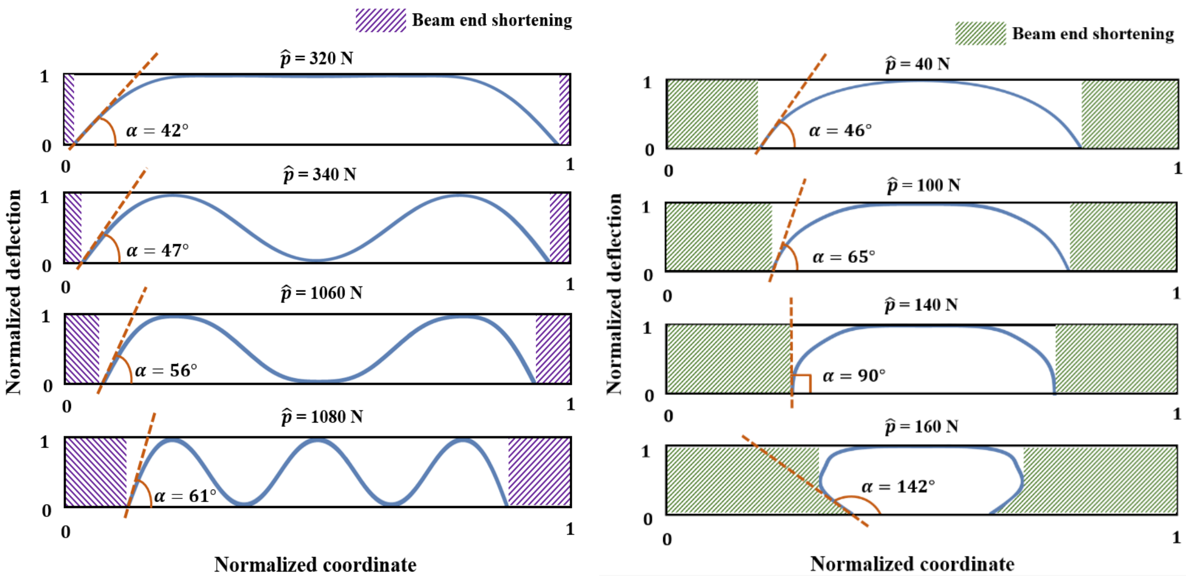

(a) (b)

Figure 4-11. Deflected shapes of a slender beam determined by the linear eigenvalue model with a gap of 20 mm

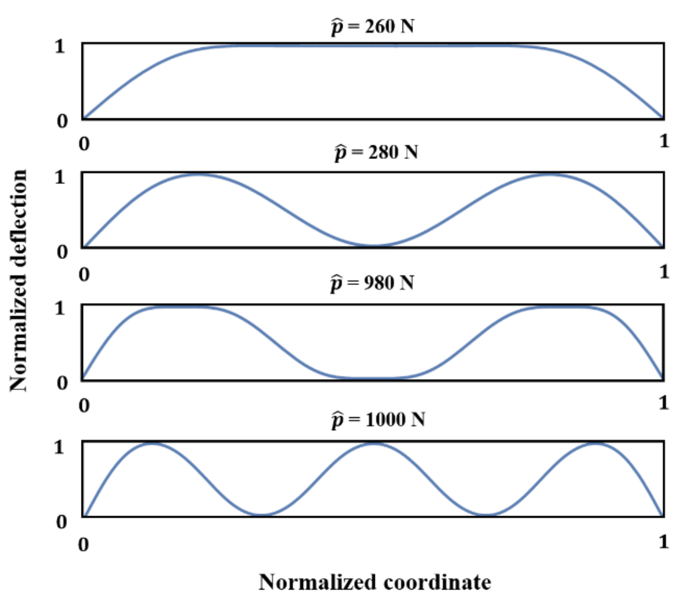

Figure 4-12. Deflected shapes of a slender beam determined by the linear eigenvalue model with a gap of 20 mm.

Figure 4-12 presents the deflected shapes of a slender beam determined by the linear eigenvalue model with a gap of 20 mm. It can be seen that when increases the axial force, $\hat{p}$, to 260 N, the beam flattens and then snaps into the third mode with an force of $\hat{p} = 280$ N. Flattening regions are found in the third buckling mode when the axial force is $\hat{p} = 980$ N, and then the beam snaps into the fifth mode when the axial force is $\hat{p} = 1000$ N. Since the beam end shortening is negligible in this model, the change of the deformed angle, α, is not as obvious as it is in the nonlinear large deformation model. Figure 4-13 displays the deformed shape configurations of the beam based on the small deformation model. Increasing the axial force, $\hat{p}$, to 260 N, the beam flattens and then snaps into the third mode when the force is $\hat{p} = 280$ N. Keep increasing the axial force, the touching points transform to line contacts. Flattening limit is observed in the third buckling mode when the axial force is $\hat{p} = 940$ N, and then the beam snaps into the fifth mode with a force of $\hat{p} = 940$ N.

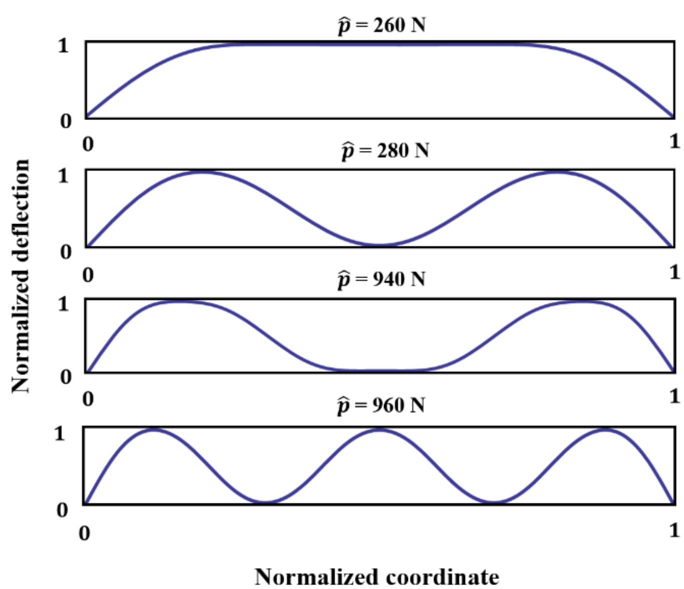

Figure 4-13. Deflected shapes of the slender beam determined by the small deformation model with a gap of 20 mm.

Similarly to the results from the linear large deformation model, the beam end shortening in this small deformation model is overlooked, and therefore the change of the deformed angle is ignorable.

Comparing the beam shape deformations obtained in Figs. 4-11(a), 4-12, and 4-13, it is demonstrated that the nonlinear large deformation model accurately measures the beam shape deformations with respect to different buckling mode transitions, i.e., point touching, flattening, or snap-through. More importantly, the presented model sufficiently takes into account the beam end shortening that is ignored in both the linear large deformation and small deformation models.

4.6.2.2. Validation with Experiment

In order to experimentally validate the presented nonlinear theoretical model, a polycarbonate beam was investigated. The experimental setup is demonstrated in Figure 4-14. It can be seen the beam was placed between the aluminum frameworks, adjacent to one rigid wall. The testing procedures consisted of applying a gradually increasing compressive load through a loading block to the beam. The gap separating the lateral constraints was fixed at 20 mm. The beam had simply supported end supports. The geometry and material properties of the testing specimen is displayed in Table 4-2.

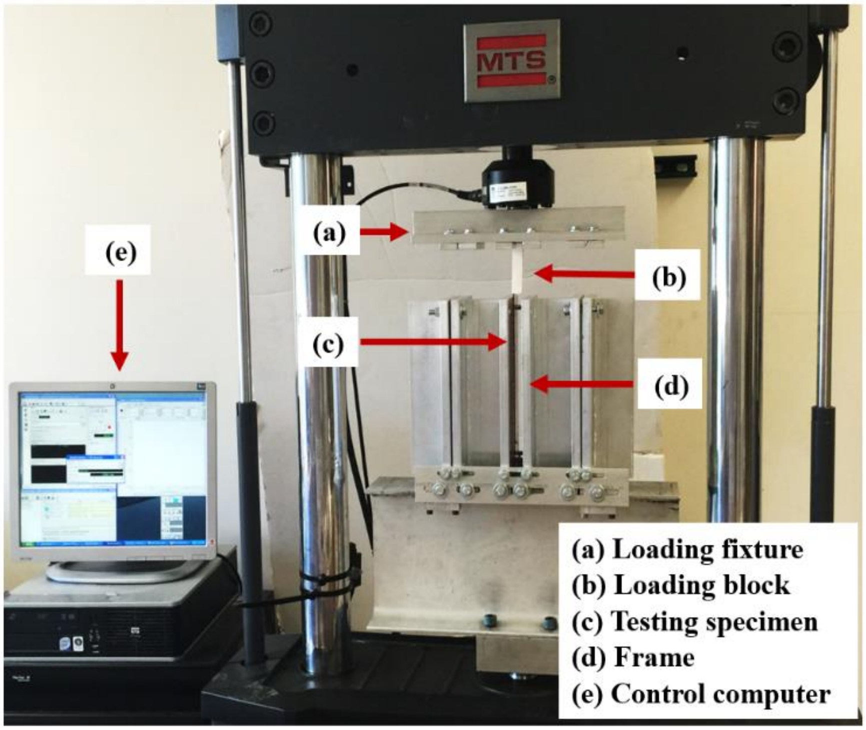

Figure 4-14. Experimental setup.

Table 4-2. Geometry and material properties of the testing setup.

Beam length (mm)	250
Beam thickness (mm)	1.00
Beam width (mm)	30
Young’s modulus (GPa)	2.3

Figure 4-15 presents the experiment conducted in this section to validate the axial force-displacement relationship of the nonlinear large deformation model. It can be seen that the theoretical and experimental results had sufficient agreement. However, a slight force reduction was measured in the experiment at mode transition Φ3. This phenomenon was due to the quasi-static loading procedure that applied to the slender beam. Since the compressive load was gradually placed on the sample, the snap-through of the buckling mode from Φ1 to Φ3 behaved a particular process that consists of certain unstable temporary statuses.

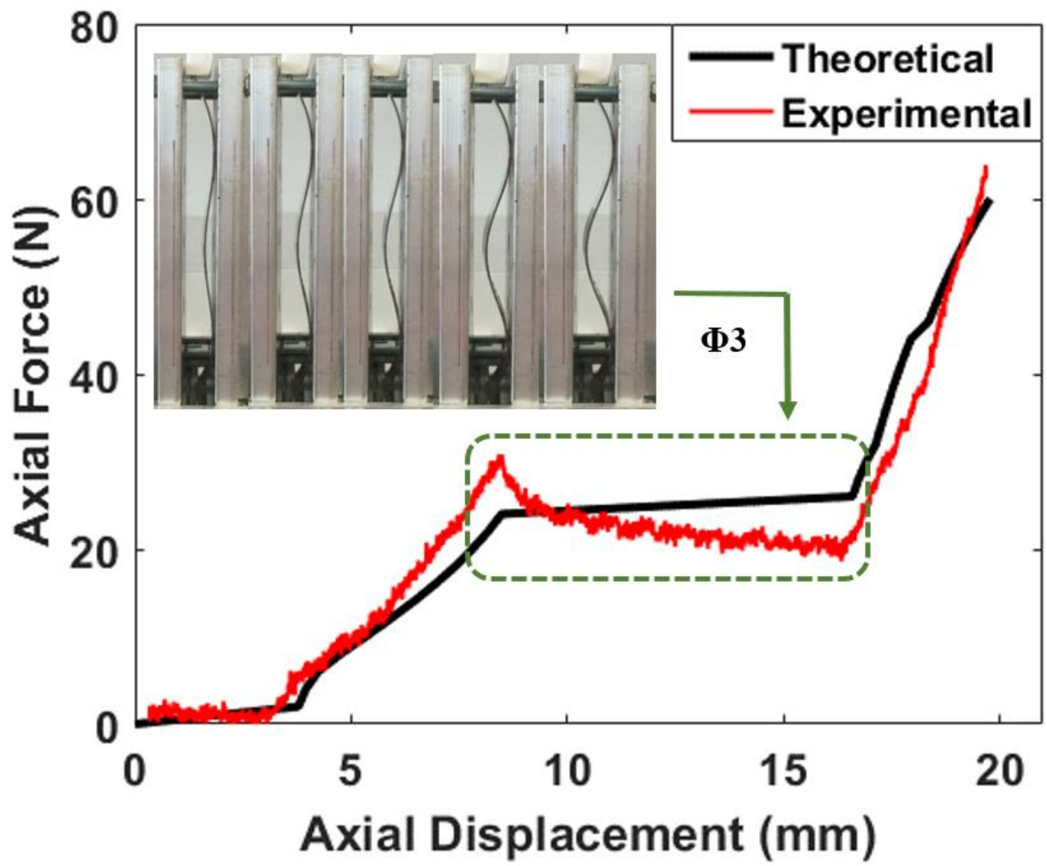

Figure 4-15. Comparison of the axial force and displacement relationship between the presented nonlinear large deformation model and experimental results.

Figure 4-16 shows the deflected shape configurations of the beam in terms of different buckling modes. Figure 4-16(a) displays the shape of the initial straight beam. Figs. 4-16(b) and (c) indicate the point touching and flattening of the beam deformed shapes in the first buckling mode, respectively. Figs. 4-16(d) and (e) demonstrate the shape deflections in the third mode at the point touching and flattening stages, respectively. Note that the red markers highlighted on the aluminum walls represented the end shortenings under different loading states. Since loading fixture was placed on top of the aluminum frameworks, end shortening was observed only on top of the specimen.

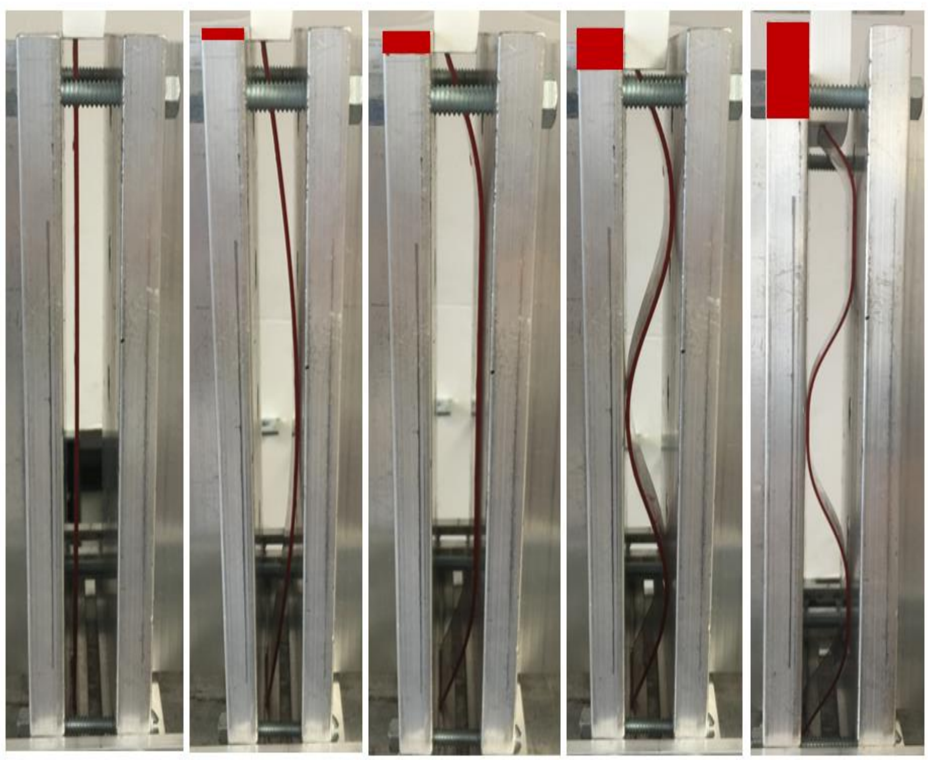

(a) (b) (c) (d) (e)

Figure 4-16. Beam configurations: (a) initial straight shape, (b) point touching (Φ1), (c) flattening (Φ1), (d) point touching (Φ3), and (e) flattening (Φ3).

4.7. Fatigue, Cyclic Loading and Recoverability

The material investigated in the presented theoretical study is linear elastic and, therefore, the Young's modulus is constant, i.e., 2.3 GPa. This is mainly because of the research objective in this study is to implement the buckling-based mechanism for applications in civil infrastructures, e.g., energy harvesting or damage sensing. It is of necessity to retain the linear elastic response of the beams such that the post-buckling behavior, especially buckling mode transitions, is repeatable. In experiments, polycarbonate was used to manufacture the testing samples. Previous experimental studies carried out by our group have demonstrated the recoverability of the material under cyclic loading (Lajnef et al. 2012). In particular, the same post-buckling response is retained invariant under cyclic loading. Figure 4-17 displays the experimental post-buckling response of bilaterally constrained beams subjected to cyclic loading at 0.16 Hz, 0.05 Hz, 0.025 Hz, and 0.006 Hz (Lajnef et al. 2012).

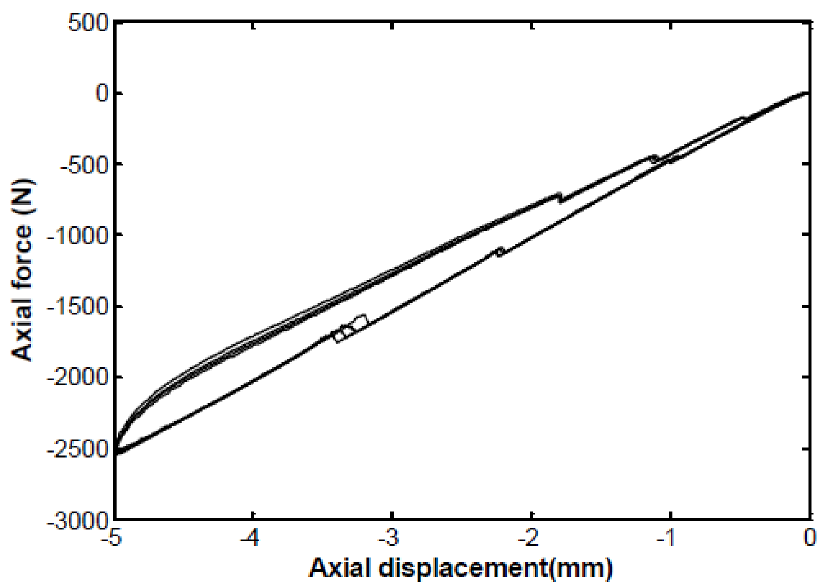

Figure 4-17. Experimental post-buckling response of bilaterally constrained beams subjected to cyclic loading (Lajnef et al. 2012).

4.8. Summary

Simply supported and clamped-clamped, large deformation models were developed in this chapter to investigate the post-buckling response of slender beams under bilateral constraints. The equilibrium equations in the presented models were solved using an energy method that minimized the total energy of the system with respect to the weight coefficients of different buckling modes. The theoretical results, i.e., force-displacement relationship and deflected beam shape, were validated with a small deformation model presented in a previous study as well as experiments. Good agreements were achieved in both of the comparisons.

The theoretical models presented in this study accurately measure the post-buckling response of bilaterally constrained beams, especially the beam end shortening and deformation angle under different buckling modes. It is indicated that the presented large deformation model is effective in understanding and predicting the post-buckling response of bilaterally confined beams.

CHAPTER 5

IRREGULARLY BILATERAL CONSTRAINTS AND COMPARISON BETWEEN THE SMALL AND LARGE DEFORMATION MODELS

5.1. Overview

In recent years, post-buckling has been implemented into extensive mechanisms. As one of the primary applications, the buckling response of slender beams under lateral confinements is of research emphasis as low-rate and low-frequency excitations can be transformed into high-rate motions. To achieve the conversion, efficient control over post-buckling response is of necessity in the process. However, inadequate studies have been carried out to examine the effect of geometry property on beams' post-buckling performance. This chapter aims at investigating the buckling behavior of bilaterally constrained beams with respect to different shape configurations of bilateral constraints and geometry parameters. The studies of the proposed models indicate that the small deformation model sufficiently captures higher buckling mode transitions, but is insufficient for beam end-shortening since longitudinal displacement is negligible. The large deformation model effectively predicts severe deflection of the beams in terms of end-shortening and rotation. Parametric studies are conducted to examine the limitations of the small and large deformation models. In the end, a polynomial function is provided to define the relationship between the ratio of the net gap and beam length (η) and buckling mode (Φ). The presented models are effective in understanding and predicting the post-buckling responses of laterally confined beams under the small and large deformation theories.

5.2. Introduction

Over centuries, buckling and post-buckling of slender members have caused various instability issues to structures, especially for the members made of the materials with low shear stiffness and high resilience. Recently, however, research focuses have been shifted from preventing buckling to employing it in different types of “smart applications”. The implementations of post-buckling response are extensively found in monostable, bistable and multi-stable mechanisms, e.g., actuation, sensing, and energy harvesting (Camescasse et al., 2013; Harne & Wang 2013; Blarigan et al., 2015). Based on post-buckling of bilaterally confined beams, for example, an energy harvesting solution has lately been developed to transform ambient energies into electrical power (Lajnef et al., 2014). Sufficiently converting energies, this buckling-based energy harvester is used to power remote wireless sensor (Lajnef et al., 2015). The limitations of wiring harness and battery lifetime are solved by the energy harvesting mechanism and, therefore, the wireless sensor is able to generate monitoring data into many applications, i.e., structural health monitoring and damage detection (Guo et al., 2012; Salehi et al., 2015; Alavi et al., 2016; Alavi et al., 2017). In order to optimize the energy conversion of the harvester, it is of research interests to control the buckling response of the system. In particular, the buckling performance of the laterally constrained beams is significantly affected by the gap between the bilateral walls. If the constraints gap is adequately large, namely comparable to beam length, the system is under the large deformation assumptions. If the gap is small, on the other hand, the post-buckling response is governed by small deformation theory. However, lack of studies have been conducted to indicate the influence of walls gap on the buckling performance of constrained beams. Nor have adequate studies identified the applicability of the small and large deformation theories with respect to the prediction of post-buckling performance.

Literature review demonstrates that research efforts have been devoted to the buckling analysis of slender elements without lateral constraints. In order to strengthen slender structures, an I-beam element with sinusoidal web geometry was theoretically and experimentally studied by Jiao et al. (2012) and Chen et al. (2013). The critical buckling capacity of the proposed element was improved. Using the first order shear deformation theory, Ovesy et al. (2015) have developed a layerwise approach to study the delamination of composite plates due to post-buckling. Milazzo and Oliveri (2015) have studied the delamination of composite plates caused by post-buckling using the Rayleigh-Ritz method. Alijani et al. (2016) and Amabili et al. (2016) have theoretically and experimentally investigated the vibrations of thin rectangular and curved plates subjected to out-of-plane harmonic excitations. Based on the Donnell's non-linear shell theory, the authors used a unified energy approach to obtain the discretized non-linear equations using the linear natural modes of vibration. On the other hand, many studies have been conducted based on the large deformation theory. Wang et al. (2008) theoretically solved the deflection of cantilevered beams under tip loads. The authors used a homotopy analysis to obtain the displacements of the beams in the horizontal and vertical directions. Sofiyev and Kuruoglu (2013) have studied the buckling response of orthotropic conical shells under compression using large deformation-based von Krman-Donnell kinematic nonlinearity. Santos and Gao (2012) have presented a canonical dual mixed finite element method to examine the post-buckling behavior of largely deformed planar beams. The total potential energy of the elements is used to determine the deflection of the beams. Zhang et al. (2016) have developed a wavelet method based on the large deformation assumptions to carry out a post-buckling analysis on nonlinearly elastic rods. A modified wavelet approximation of an interval bounded L^2 –function is then used to capture the buckling response of the cantilevered rods. However, since lack of consideration has been devoted to constraints long element length, only the critical load of the first buckling mode (Φ1) is obtained in these studies.

Motivated by identifying and exploiting post-buckling response, various types of lateral controls have been taken into account. Chai (1998) has developed a model to measure the buckling behavior of bilaterally constrained beams subjected to axial compressions. Liu and Chen (2013) have theoretically examined the post-buckling behavior of an elastica in straight channel with clearance. The Coulomb friction between the elastica and channel is effectively addressed. Ro et al. (2010) have proposed a method to capture largely deformed beams under lateral controls. By adjusting boundary conditions and location of the beam between the rigid walls, different types of buckling equilibrium configurations are obtained. Katz and Givil (2015) have carried out a buckling analysis on beams between springily supported rigid walls. The governing equations in those studies are solved based on equilibrium conditions and geometric compatibilities and, thus, the analyses are limited in lower buckling modes, e.g., Φ1 and Φ3. In order to address the challenge of determining higher buckling modes, an energy method has been developed. The lowest total energy of a buckling system is maintained at every equilibrium status and, therefore, beam shape configurations can be predicted by minimizing the total energy between bilateral constraints. Doraiswamy et al. (2012) have studied the Viterbi algorithm to determine the minimum energy-based configurations of constrained beams under axial forces. More recently, Borchani et al. (2015) have minimized the total potential energy of buckling systems based on the Nelder–Mead algorithm. Satisfactory agreements are achieved between the theoretical and experimental results, especially in higher buckling modes (Φ5 or Φ7). An optimal design has been carried out by Jiao et al. (2016) to effectively control the mode transitions of confined buckling elements by adjusting the cross-section geometry of slender beams. However, more research is of necessity to indicate the applicability of the large and small deformation theories with respect to geometry property of buckling systems. In order to address the research gap, two theoretical models are developed in this study based on the small and large deformation assumptions, respectively. This chapter aims at theoretically investigating the impact of geometry property and boundary conditions on the post-buckling behavior of slender beams, and identifying the relationship between the small and large deformation models.

5.3. Irregularly Bilateral Constraints

5.3.1. Problem Statement

The problem under consideration consists of a clamped-clamped prismatic homogeneous straight beam subjected to an axial load, $\hat{p}$. The beam has a length (L), thickness (t), width (b), cross-section area (A), moment of inertia (I) and modulus of elasticity (E). The slender beam is confined between two frictionless rigid walls spaced a distance h_0. The net gap between the lateral constraint and the beam is defined by $h = h_0 - t$. In order to investigate the impact of bilateral walls on the post-buckling response of the beam, irregular constraints are taken into account in this study. It is worth noticing that the bilateral constraints are defined such that the beam can be deformed only within the gap between them. Therefore, the influence of the bilateral constraints can be measured with respect to the variation of the gap. Figure 5-1 presents the beam that is under randomly bilateral constraints. Figure 5-1(a) schemtically shows the deformation of the slender beam. It can be seen that the wall that is adjacent the beam is fixed as flat, while the one away from the beam is randomly changed. The net gap between the constraints can be expressed as $h(x)$. In order to investigate the post-buckling response of the deformed beam under the influence of irrgularly regid walls, a discretization algorithm is introduced in this study. Figure 5-1(b) indicates the constraints after discretization. It can be seen that the random constraint is discretized into n segments, i.e., ΔL_1, ΔL_2,…, ΔL_n. Each segment has a constant net gap that is normalized with respect to the gap of the first segment, namely $\alpha_i = \frac{\mathrm{Gap}_{\Delta L_i}}{\mathrm{Gap}_{\Delta L_1}}$ $(i = 1, \dots, n)$. To represent the net gap variation of the irregularly bilateral constraints, a normalized $1 \times n$ net gap vector is generated, accordingly, as,

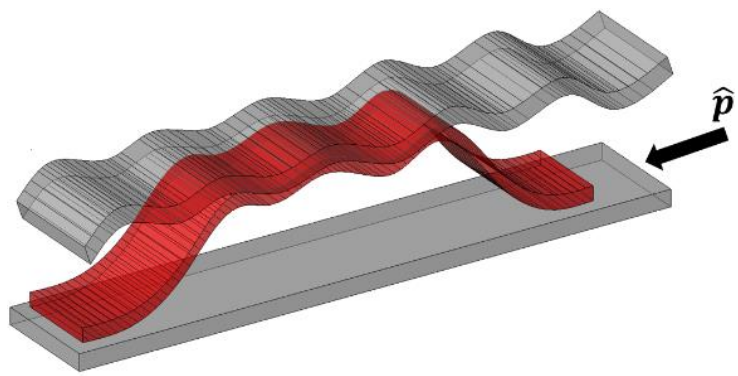

(a)

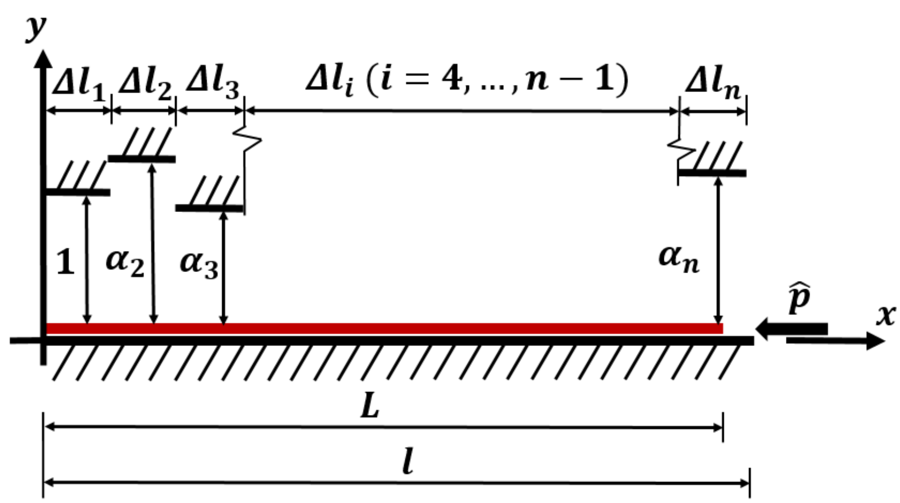

(b)

Figure 5-1. Illustration of a beam under irregularly bilateral constraints. (a) Schematic of the beam's deformation in the first buckling mode, and (b) discretization of the irregularly bilateral constraints.

$$G = (1, \alpha_2, \alpha_3, \dots, \alpha_n) \tag{5-1}$$

5.3.2. Results and Discussion

The theoretical models, i.e., the small and large deformation models, presented in Chapters III and IV are used to investigate the effect of bilateral confinements on the post-buckling response of the system. According to the presented theoretical models, two types of bilateral constraints are specifically studied, namely, linear and sinusoidal constraints, as shown in Figure 5-2. Figure 5-2(a) displays the linearly bilateral constraints that the normalized net gap is given as

$$h_{Lnr} = 1 + \frac{1}{2L}x \tag{5-2}$$

Increasing the external force, $\hat{p}$, the deformed beam is longitudinally enforced into the region with smaller gap. Therefore, the flattening region will be leaned based on the shape of the constraints. Figure 5-2(b) presents the beam that is deformed under the sinuoidal walls. The normalized net gap is defined as,

$$h_{Sine} = 1 + \frac{1}{2}\sin\left(\frac{2\pi x}{L}\right) \tag{5-3}$$

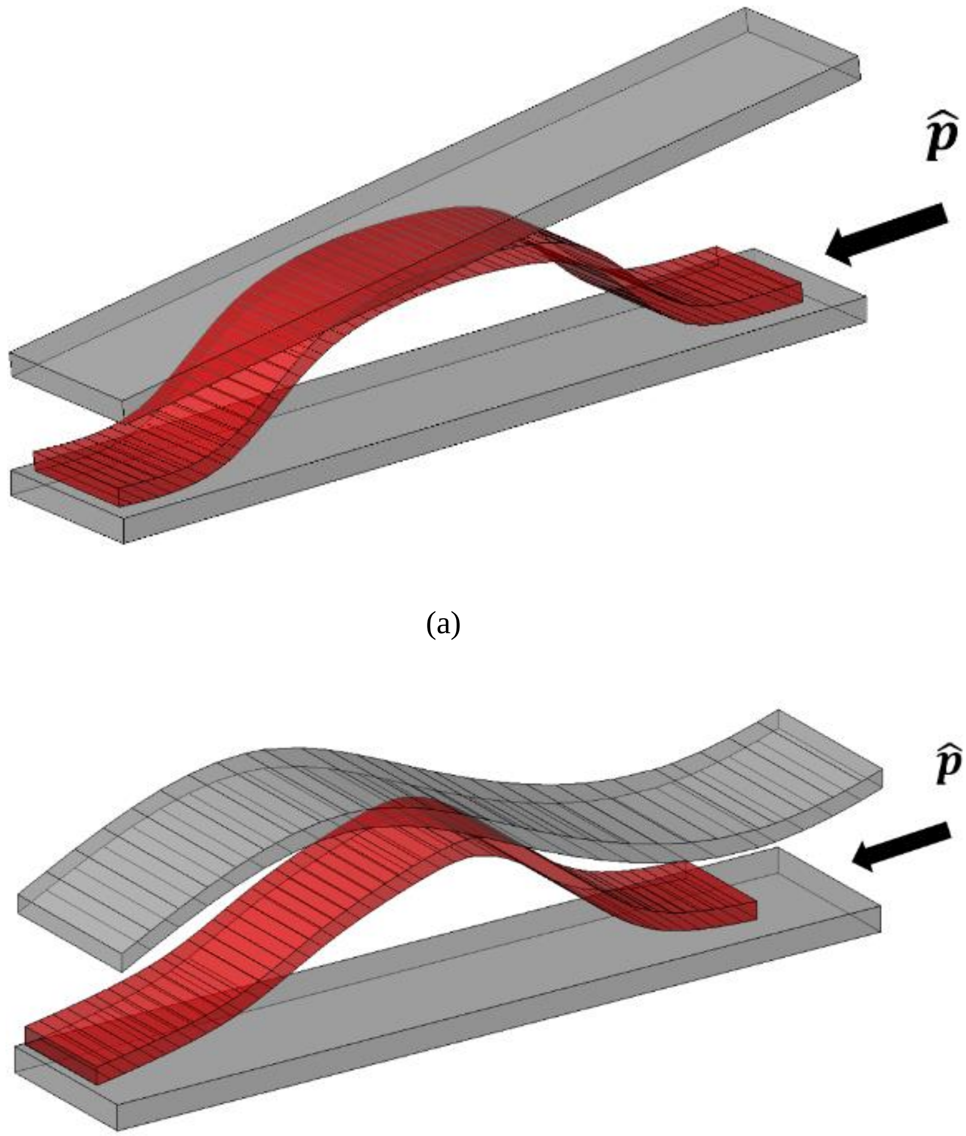

(a)

(b)

Figure 5-2. Beam deformation in the first buckling mode under (a) linearly and (b) sinusoidally bilateral constraints.

Table 5-1. Loading conditions of the system.

	Small Deformation Model		Large Deformation Model	
	Static	Dynamic	Static	Dynamic
Initial Net Gap h_{xc} (mm)	4	4	20	20
Loading Period T (s)	--	10	--	10
Max. Applied Load $\hat{p}_{max}$ (N)	--	2000[a]	--	1200

[a] From Borchani et al. (2015).

Similarly, the deflection of the beam will be shaped due to the irregular constraints. Table 5-1 summarizes the loading conditions that are used in the presented models. The maximum applied load of the small deformation model is selected based on a reference study, and the load for the large deformation model is decided by the experiments carried out in this study. In the dynamic, small and large deformation models, a linearly increasing load, $\hat{p}$, is defined in terms of loading time, $\hat{t}$, as,

$$\hat{p} = \hat{p}_{max} \frac{\hat{t}}{T} \tag{5-4}$$

where $\hat{t} = [0, T]$.

5.3.2.1. Small Deformation Model

Figure 5-3 shows the buckling mode transitions of the beam based on the static, small deformation model. The static model is obtained by neglecting the kinetic energy (**K**) and assuming the total energy is equal to the total potential energy ($\mathbf{\Omega} = \mathbf{\Pi}$). Both the linear and sinusoidal constraints are taken into account. The beam deformation is presented with respect to the normalized beam length, width, and net gap. Figure 5-3(a) displays the post-buckling response of the beam under linear constraints. It can be seen that the deformations of the beam follow the configuration of the linear walls. Due to the boundaries, the point and line contact regions in buckling modes Φ1, Φ3 and Φ5 are shaped linearly. Figure 5-3(b) presents the beam shapes under the sinusoidal constraints. The contacts between the deformed beam and boundaries coincide with the pattern of the constraints. Note that Φ1, Φ3 and Φ5 represent the final deformed shape configurations of the constrained beam under compression. In this chapter, only the first 20 mode shapes are considered mainly due to the following two reasons,

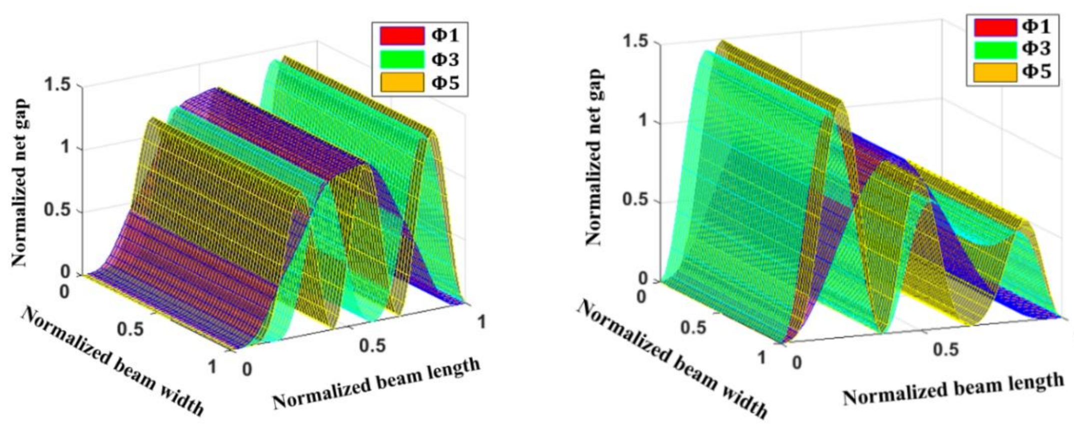

(a) (b)

Figure 5-3. Beam shape deformations by the static, small deformation model under (a) linear and (b) sinusoidal constraints.

- Taking into account more buckling mode shapes, for example $m = 30$, in the linearly combined shape functions would significantly increase the computational cost; and
- More mode shapes also result in more severe numerical errors when numerically minimizing the total energy for the weight coefficients, C_m. Therefore, the accuracy of the final results would be impacted.

Figure 5-4 displays the beam shape deformations corresponding to the same results presented in Figure 5-3. In Figure 5-4(a), the deflected beam is constrained by Eq. (5-2) such that the post-buckling responses in modes Φ1, Φ3 and Φ5 are observed only within the linearly bilateral boundaries. Figure 5-4(b) indicates the influence of the sinusoidal constraints on the beam deformation. It can be seen that the beam is buckled within the net gap between the linear and sinusoidal boundaries.

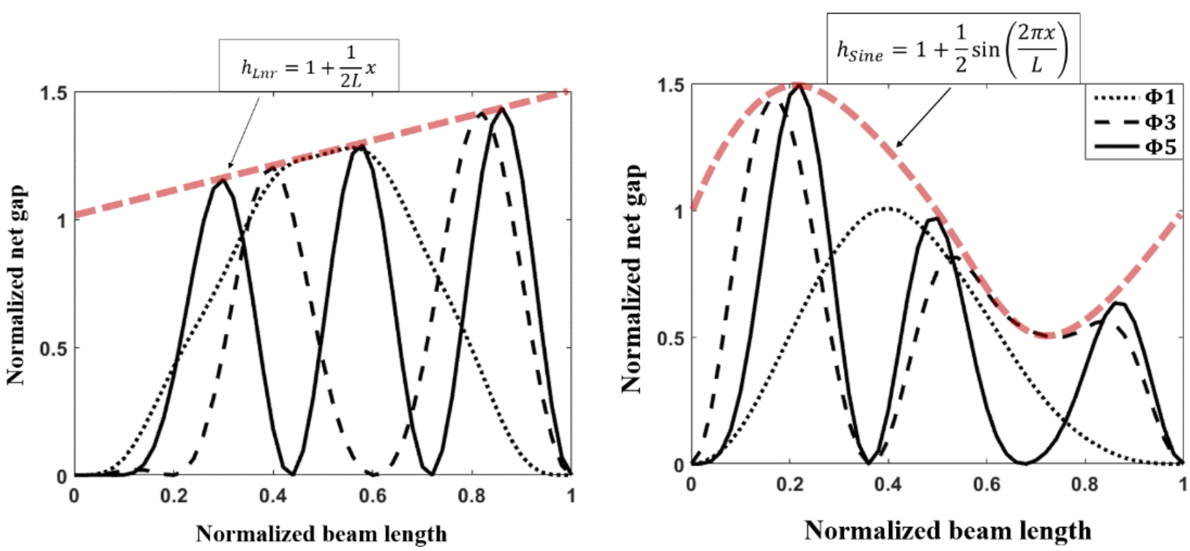

(a) (b)

Figure 5-4. Post-buckling response by the static, small deformation model under (a) linear and (b) sinusoidal constraints.

5.3.2.2. *Large Deformation Model*

Figure 5-5 shows the post-buckling response of the deformed beam basded on the static, large deformation model. The linearly bilateral constraints are taken into account in Figure 5-5(a) and the sinusoidal constraints are used in Figure 5-5(b). The deformed configurations of the beam in the figure match the patterns of the constraints. More interestingly, the end-shortenings are achieved from all the buckling modes. The linearly and sinusoidally shaped deformations are satisfactorily predicted by the theoretical model. Consequently, the presented models are able to sufficiently capture the static post-buckling response of the linearly and sinusoidally constrained beams based on both small and large deformation assumptions.

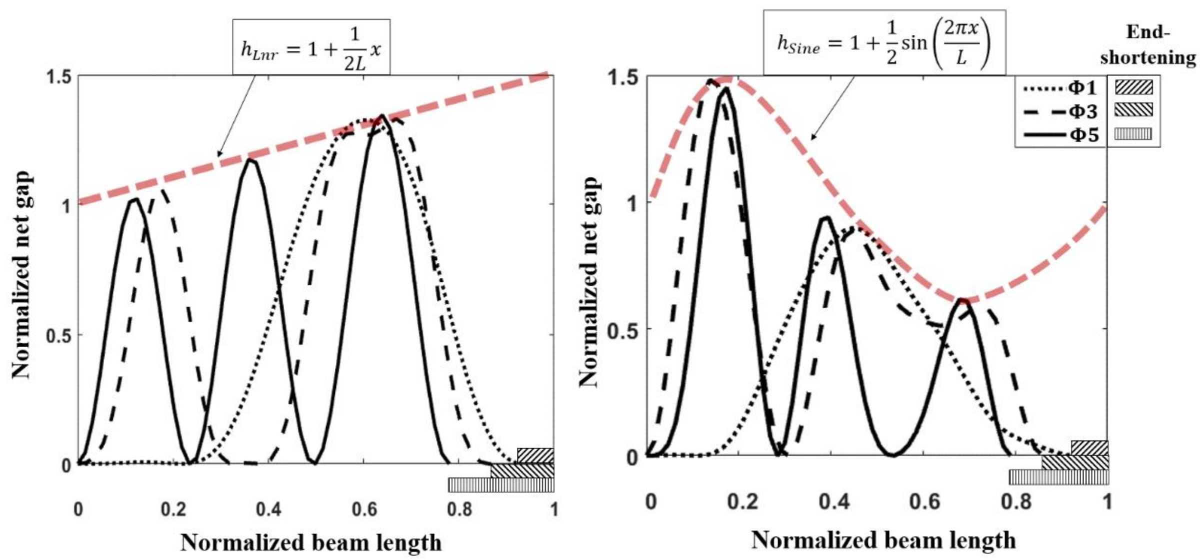

(a) (b)

Figure 5-5. Post-buckling response by the static, large deformation model under (a) linear and (b) sinusoidal constraints.

5.3.2.3. Model Comparison

Figure 5-6 presents the comparison between the static, small and large deformation models. The results are obtained under the sinusoidal constraints. It can be seen that the post-buckling responses predicted by the small and large deformation models are comparable in terms of different buckling modes (Φ1, Φ3 and Φ5). As summarized in Table 5-1, the only difference between the two systems is the net gap, i.e., 4 mm and 20 mm for the small and large deformation models, respectively. Therefore, similar post-buckling behaviors are achieved. However, the results based on the large deformation model are longitudinally "compacted", due to the end-shortenings (Δ_{Φ_1}, Δ_{Φ_3}, and Δ_{Φ_5}).

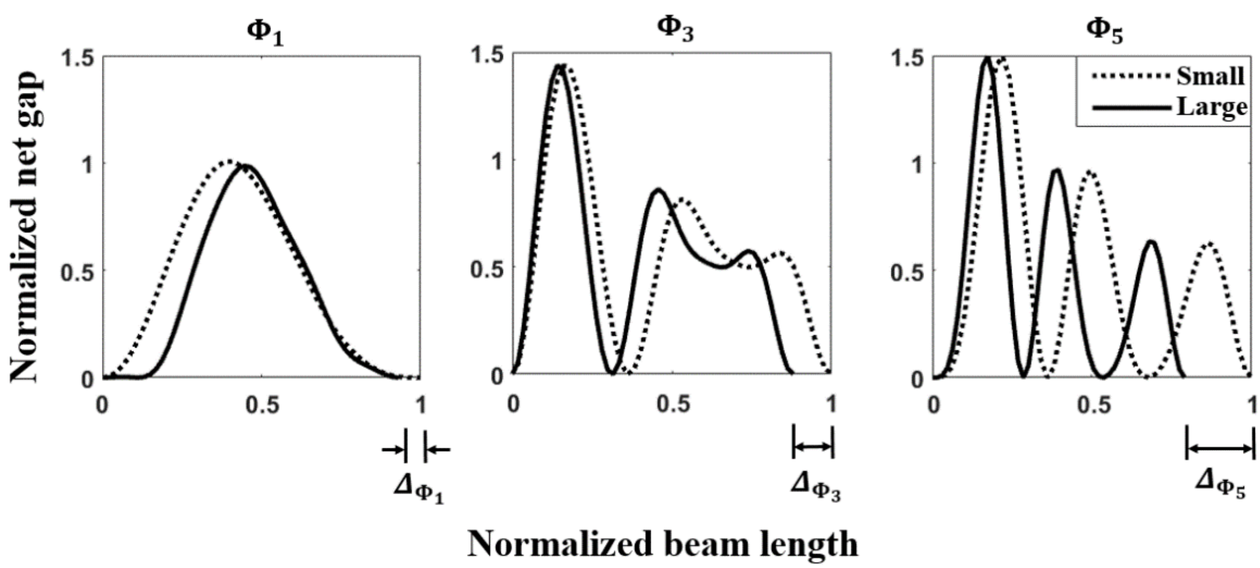

Figure 5-6. Comparison between the static, small and large deformation models under the sinusoidally bilateral constraints

5.4. Comparison between Small and Large Deformation Models

5.4.1. Problem Statement

The problem under consideration consists of a clamped-clamped prismatic homogeneous straight beam subjected to an axial load, $\hat{p}$. The slender beam is placed between two frictionless rigid walls, next to one constraint and apart from the other. The beam has a length (L), thickness (t), width (b), cross-section area A, moment of inertia (I) and modulus of elasticity (E). The gap between the bilateral constraints is h_0 and the net gap between the lateral wall and beam is $h = h_0 - t$, as shown in Figure 5-7(a). Figure 5-7(b) presents the beam deformation under the assumptions of small deformation. Since the net gap, h, is assumed to be much smaller than the

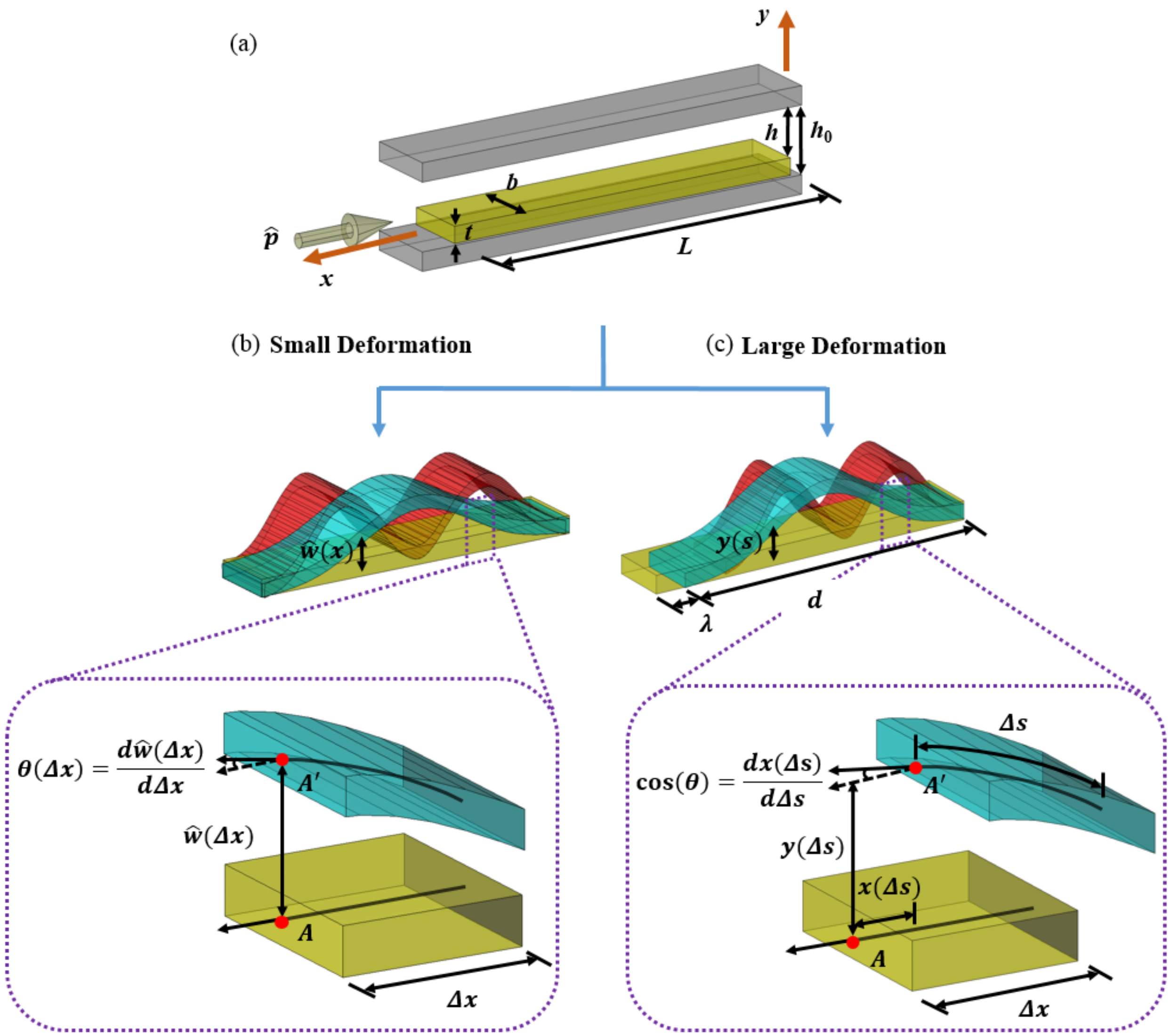

Figure 5-7. (a) Geometry of an initially straight beam and the deformation analysis of a segment under (b) the small and (c) the large deformation theories.

beam length, L, i.e., $\frac{h}{L} \ll 1$, the rotation of the deformed beam's neutral axis, θ, is small. Therefore, the relationship $\theta(\Delta x) = \sin\big(\theta(\Delta x)\big) = \frac{d\hat{w}(\Delta x)}{d\Delta x}$ is held throughout the entire beam. It can be seen in the segment that the initial point in the initially straight beam A is vertically deflected to A' where the horizontal displacement is neglected. Only the transverse deflection, $\hat{w}(x)$, is taken into account in this small deformation model. Figure 5-7(c) shows the deformed beam based on the large deformation theory. The net gap, h, is assumed to be comparable to the beam length and, thus, the beam is significantly buckled under compression. The horizontal displacement of the beam, $\lambda(s)$, will not be negligible, and the length projection of the deflected beam is no longer equal to the beam length, namely $d \neq L$. In addition, the relationship on the rotation angle found in the small deformation is invalid, e.g., $\theta(\Delta x) \neq \sin\big(\theta(\Delta x)\big)$. Hence, it is of necessity to take into account both the longitudinal and vertical deformations, x and y.

5.4.2. Findings and Discussion

5.4.2.1. Small Deformation Model

Since the post-buckling response is significantly impacted by the geometry properties of the system, this section aims at identifying the comparability and dissimilarity of the small and large deformation models with respect to the net gap (h) and beam length (L). The geometry and material properties in Table 5-2 are used. The net gaps are specifically selected as (a) 4 mm and (b) 10 mm. The buckling mode transitions are displayed in the 3D view with respect to the normalized beam length, width, and net gap. The corresponding 2D results are shown in terms of normalized length and net gap.

Table 5-2. Geometry and material properties of the system.

Length (mm)	Width (mm)	Thickness (mm)	Young's modulus (GPa)
250	30	1	2.3

Figure 5-8 presents the buckled shape configurations of the beam based on the small deformation model. Figure 5-8(a) displays the post-buckling response of the beam in the net gap of 4 mm. Under the axial force, the initially straight beam begins to buckle. Due to the bilateral confinements, the first mode beam deformation is restricted within the constraints. After touches the lateral walls, the point contact between the deformed beam and walls grows to a line contact ($\Phi1$). Increasing the force, the line contact reaches the critical condition and then snaps into the third buckling mode ($\Phi3$). The beam buckles to $\Phi5$ and $\Phi7$ when the axial force meets the next critical conditions. Figure 5-8(b) presents the post-buckling behavior of the beam in the net gap of 10 mm. The contacts between the deformed beam and boundaries are captured coincide with the pattern of Figure 5-8(a), namely, line contact and buckling snap-through. Since the net gap is increased from 4 mm to 10 mm, "more material" is requested for the deflected beam to buckle into higher modes. Therefore, Figure 5-8(b) measures the fifth buckling mode ($\Phi5$) while Figure 5-8(a) reaches up to the seventh ($\Phi7$). However, neither Figure 5-8(a) nor (b) has obtained end-shortenings since the longitudinal displacement in the small deformation model is negligible. Increasing the net gap, the rotation angle of the deformed beam will be significantly increased and the displacement in the longitudinal direction will be dramatically enlarged. Therefore, the assumptions of small deformation are no longer applicable. In order to sufficiently predict the post-buckling response of the deflected beam with critical rotation and end-shortening, large deformation theory needs to be applied.

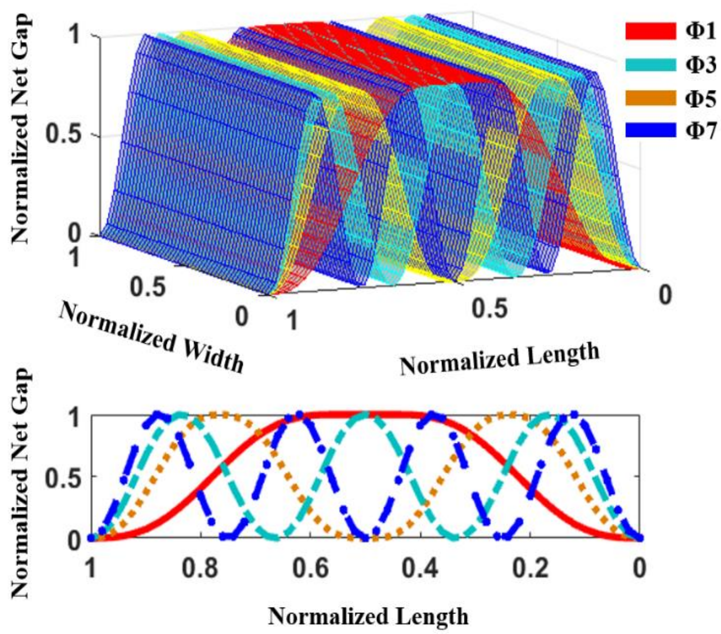

(a)

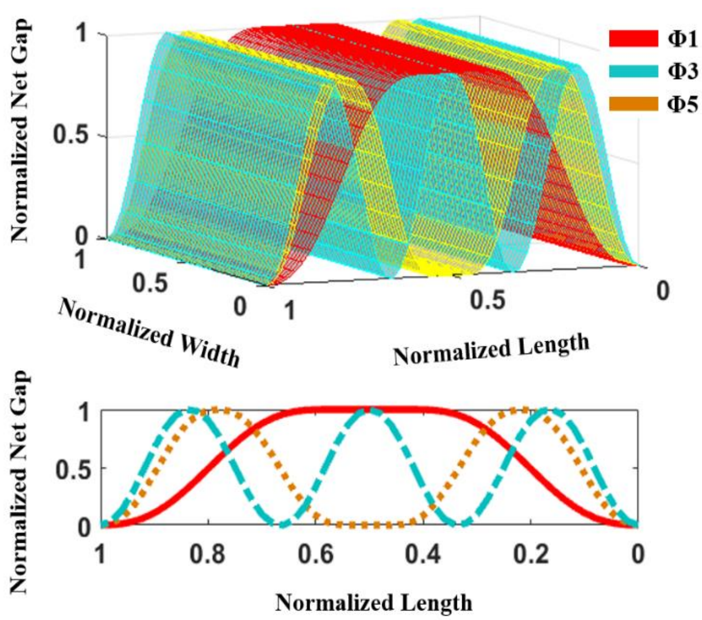

(b)

Figure 5-8. Small deformation-based beam shape deformations under the net gaps of (a) 4 mm and (b) 10 mm.

5.4.2.2. Large Deformation Model

Figure 5-9 shows the deflected beam shapes based on the large deformation model. The geometry and materials summarized in Table 5-2 are used. The net gap are chose as (a) 20 mm and (b) 100 mm. Similar to Figure 5-8, the post-buckling response of the beam is presented with respect to the normalized beam length, width and net gap. In order to indicate the end-shortening and rotation angle (θ), corresponding 2D beam shape deformations are presented. It can be seen that the end-shortening and rotation angle are sufficiently measured by the large deformation model.

Figure 5-9(a) displays the deflected beam shapes under the net gap of 20 mm. Comparable to the small deformation-based results, the buckling characteristics of the bilaterally constrained beam are observed as line contact (Φ1), and buckling snap-through (Φ3 and Φ5) as well. Since the net gap is relative insignificant comparing to the beam length, the rotation angle and end-shortening are not critically changed between different buckling modes. Figure 5-9(b) indicates the buckling performance of the beam under the net gap of 100 mm. The net gap-to-beam length ratio is up to 0.4 and, thus, the buckling shape of the beam severely deforms in the first mode, rather than snaps into higher modes. With the increasing of the rotation angle, it can be seen that the beam is severely deflected, which led to the dramatic enlargement of the beam end-shortening. The results are presented with respect to particular rotation angles, i.e., θ_1, θ_2 and θ_3 are $60°$, $90°$ and $120°$, respectively. The rotation angle and normalized end-shortening with respect to the 20 mm and 100 mm net gaps are presented in Table 5-3.

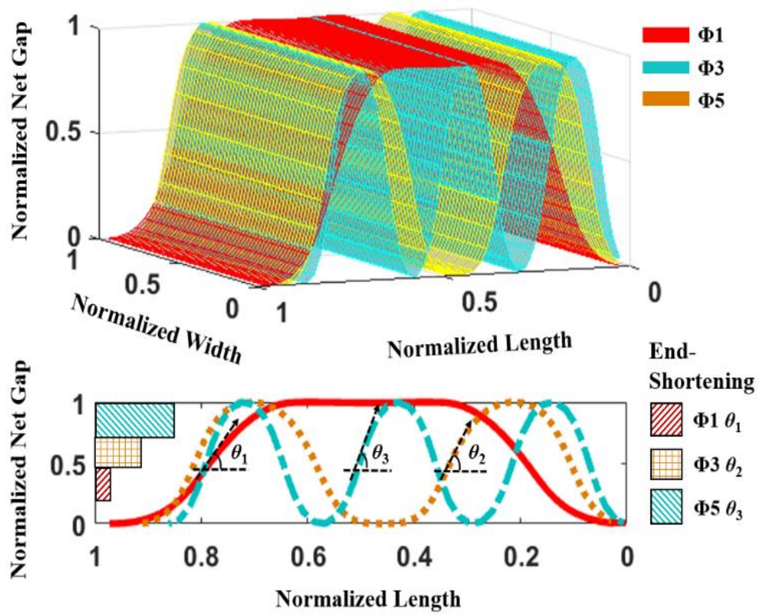

(a)

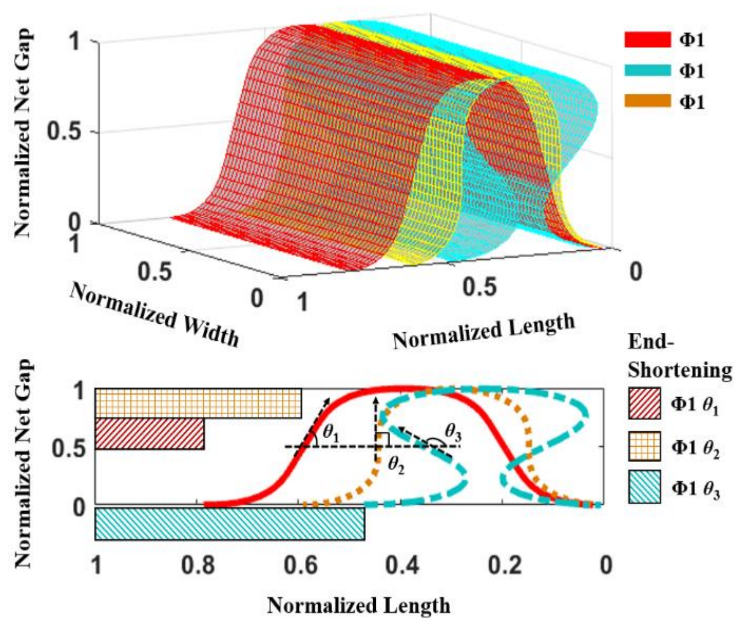

(b)

Figure 5-9. Large deformation-based beam shape deformations in the net gap of (a) 20 mm and (b) 100 mm.

Table 5-3. Rotation angle and normalized end-shortening of the system.

Net Gap (mm)		20 mm	100 mm
Rotation angle (°)	θ_1	37.03	60
	θ_2	41.26	90
	θ_3	48.54	135
Normalized end-shortening	Δ_1	0.048	0.231
	Δ_2	0.107	0.408
	Δ_3	0.159	0.497

5.4.2.3. Parametric Studies

In order to identify the limitations and suitable applications of the small and large deformation models, it is necessary to conduct parametric studies on the geometry property of the post-buckling system. The influences of the beam length (L) and net gap (h) are first investigated. In this section, the beam width and thickness are fixed as 30 mm and 2.3 mm, respectively.

Figure 5-10 presents the post-buckling response of the bilaterally constrained beam with respect to the beam length and net gap. It can be seen that when the ratio of net gap and beam length η is close to 0.1, the axial displacements determined by the small and large deformation models at different buckling mode transitions are coincided. The small deformation model is more accurate when η is smaller than 0.1, while the large deformation model predicts the buckling performance when η is larger than 0.1.

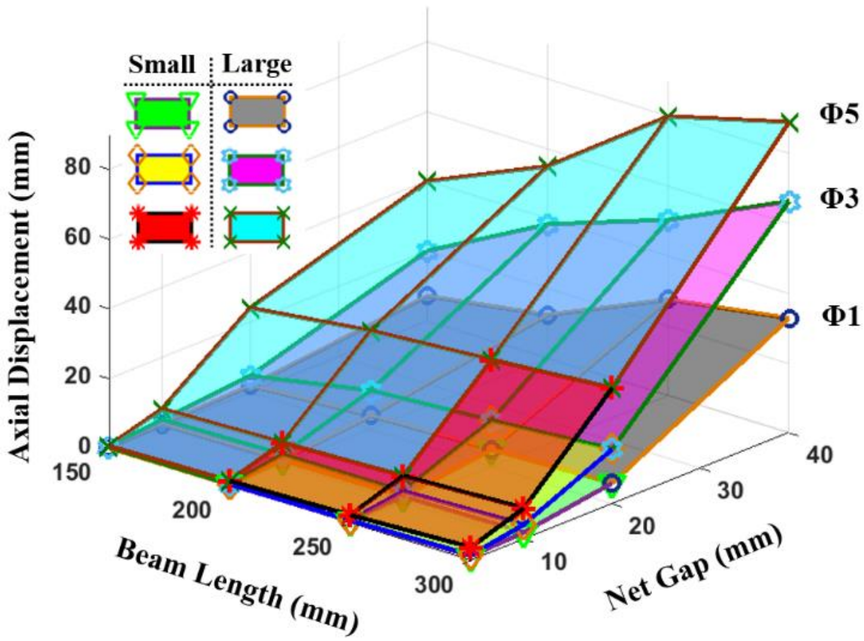

Figure 5-10. Post-buckling response of the bilaterally constrained element with respect to the beam length, net gap and axial displacement.

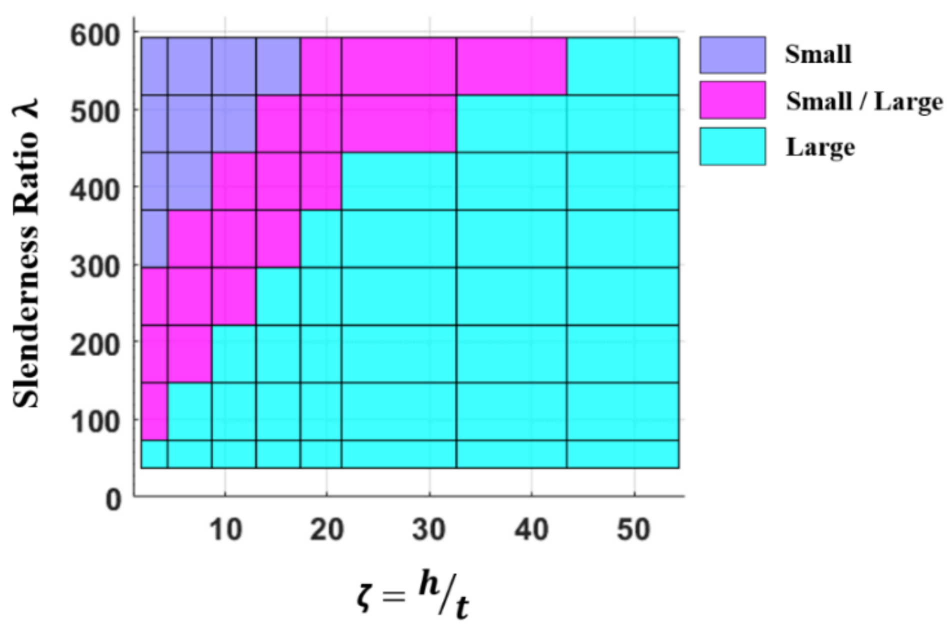

Figure 5-11. Applicability of the small and large deformation models in terms of the ratio of the net gap and beam thickness (ζ), and the beam's slenderness ratio.

Figure 5-11 displays the applicability of the small and large deformation models with respect to the ratio of the net gap and beam thickness (ζ) and slenderness ratio of the beam (λ). It can be seen that an overlapping zone with high comparability of the post-buckling response is captured between the two models.

Figure 5-12 presents the post-buckling snap-through events in terms of the ratio η and buckling mode transition Φ. The small deformation model is more accurate when $\eta < 0.12$, while the large model is suitable when $\eta > 0.08$. The overlapping zone between the small and large models is caught between $\eta \in [0.08 - 0.12]$. Meanwhile, it is observed that with the incline of η, the highest achievable buckling mode is decreased to Φ1. In particular, when $\eta \geq 0.5$, the deformed beam cannot touch the bilateral walls and, therefore, the buckling system is reduced to the slender beam without lateral constraints. The method of least squares is used to generate a polynomial function in the regression analysis to define the relationship between the highest achievable buckling mode and ratio η. According to the edge of the buckling snap-through events, a decline highest buckling mode is predicted with the increasing of η.

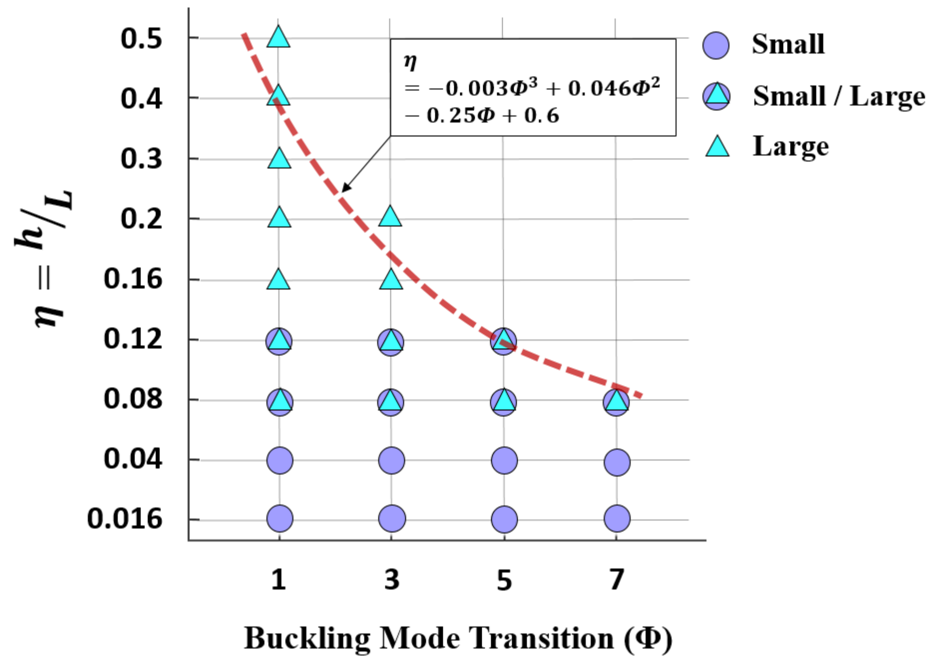

Figure 5-12. Post-buckling snap-through events in terms of the ratio of the net gap and beam length (η) and buckling mode transition.

5.5. Summary

The post-buckling response of bilaterally constrained beams was predicted with respect to different geometry properties and boundary conditions, using the theoretical models presented in Chapters 3 and 4.

- Firstly, the post-buckling response of slender beams under irregularly bilateral constraints was theoretically investigated. An algorithm was introduced to sufficiently discretize the constraints into a gap vector that represented the variation of the gap between the regid walls. The total energy of the system was minimized within the gap vector in terms of the weight coefficient (C_m) of different buckling modes. Experiments were carried out to validate the theoretical results. Satisfactory agreements were obtained. The buckling mode transitions of the beams were particularly investigated under the linearly and sinusoidally varied bilateral constraints. The deformed shapes of the beams accurately met the patterns of the constraints. The large deformation-based models were able to measure the end-shortenings.

- Secondly, parametric studies were conducted to determine the impacts of the net gap (h) and beam length (L) on the post-buckling response of the system. A pattern was gained with respect to the net gap-to-beam length ratio (η) and buckling mode transition (Φ). When $\eta < 0.12$, the small deformation model satisfactorily predicted the buckling snap-through events of the beam, and the large deformation model was sufficient when $\eta > 0.08$. In particular, an overlapping zone was observed when $0.08 < \eta < 0.12$ since the post-buckling behaviors obtained by the small and large deformation models overlapped in the region. A polynomial function was then obtained to effectively define the decline of the highest achievable buckling mode with respect to the increasing of η. According to the presented models, the small deformation model accurately captures the snap-through events in high buckling modes, i.e., Φ5 and Φ7, and the large deformation model sufficiently measures the end-shortening that resulted in severe rotation of the beams' neutral axis.

The presented theoretical models successfully predict the post-buckling behavior of the bilaterally constrained beams with respect to the confinements shape, net gap and beam length and, therefore, are effective in understanding and predicting the applicability of the small and large deformation models.

CHAPTER 6

CONCLUSIONS AND FUTURE WORK

6.1. Research Contributions

This study theoretically and experimentally investigated the post-buckling response of bilaterally constrained beam systems for energy harvesting and damage sensing. In order to achieve the objective, the main research contributions of the work can be deployed as follows,

6.1.1. Post-Buckling Analysis of Non-Uniform Beams under Bilateral Constraints Using Small Deformation Assumptions

A theoretical model based on uniform cross-section beams had been developed using small deformation assumptions in previous studies. To maximize the generated electrical power and detect potential damage, it is of necessity to accurately control the post-buckling behavior of the laterally confined systems. However, uniform beams do not permit to adequately control the mechanical response. Hence, neither the energy conversion efficiency nor damage detection accuracy of the system can be optimized. This study developed a theoretical model to measure the post-buckling response of non-prismatic beams. Based on the proposed model, the outputs of the mechanism, i.e., electrical power for energy harvesting and electrical signal for damage sensing, were sufficiently optimized.

6.1.2. Post-Buckling Analysis of Bilaterally Confined Beams Using Large Deformation Assumptions

This study presented a theoretical model using large deformation assumptions to investigate the post-buckling response of a bilaterally constrained beam subjected to a quasi-static axial force. The rotation-based equilibrium equations were formulated based on the nonlinear Euler-Bernoulli beam theory. An energy method was used to solve the equations by minimizing the total potential energy under the constraints of bilateral boundaries. The presented large deformation model satisfactorily measured the post-buckling behavior of the bilaterally constrained beam in terms of both shape deformation and force-displacement relationship.

6.1.3. Irregularly Bilateral Constraints Analysis and Parametric Studies

This study investigated the buckling behavior of bilaterally constrained beams with respect to different shape configurations of bilateral constraints, i.e., irregular constraints, and geometry parameters. It indicated that the small deformation model sufficiently captured higher buckling mode transitions, but was insufficient in determining beam end-shortening since longitudinal displacement is negligible. The large deformation model effectively predicted severe deflection of the beams in terms of end-shortening and rotation. Parametric studies were conducted to examine the limitations of the small and large deformation models. In addition, a polynomial function was provided to define the relationship between the ratio of the net gap and beam length (η) and buckling mode (Φ).

6.2. Future Work

6.2.1. Optimization of Piezoelectric Energy Scavenger

It has been proved and investigated that the levels of harvestable energy and energy conversion efficiency are relevant to input frequency. The electro-mechanical properties and natural frequency of scavenger, however, are also of significance. In particular, the piezoelectric transducer used in this study is made of polymer polyvinylidene fluoride (PVDF) due to its relatively low cost and high flexibility. However, PVDF materials have low mechanical-to-electrical conversion coefficients. Other piezoelectric materials, e.g., Lead Zirconate Titanate (PZT), Microfiber Composites, etc., have also been extensively used for energy harvesting in different applications. In addition, the dimensions of piezoelectric energy scavenger and attached lumped mass should be optimized in order to maximize the energy harvested during snap-through events.

6.2.2. Optimization of the Parameters of the Mechanism for Different Strain Ranges

The parametric study carried out in this work provides confidence that the mechanism can be scalable for embedment within structures. Strains present the input to the mechanical energy concentrators and triggers. Therefore, dimensions and material properties of the bilaterally constrained beam as well as the gap between the lateral rigid walls should be tuned such that transitions occur under the applied level of strain. A design manual or chart can be developed to determine the optimized values of the parameters for different strain ranges. It would be of interest if the mechanism is installed in a pre-compressed configuration such that it transitions between a higher and lower buckling mode as the global input strain alternates between compression and traction.

6.2.3. Optimization of the Algorithm to Include Friction Effect

The theoretical results shown in this work do not include the effect of friction on the post-buckling dynamic response of the bilaterally constrained beam. It would be of interest to investigate the effect of friction on the post-buckling behavior as well as the levels of the released energy and generated accelerations. A simplification or approximation of the dissipated energy would alleviate the minimization problem resolution.

REFERENCES

REFERENCES

Abadi, M.M. and Daneshmehr, A.R., An investigation of modified couple stress theory in buckling analysis of micro composite laminated Euler-Bernoulli and Timoshenko beams, International Journal of Engineering Sciences, 2014, 75: 40-53.

Abdel-Rahman, E.M., Younis, M.I. and Nayfeh,A.H., Characterization of the mechanical behavior of an electrically actuated microbeam, Journal of Micromechanics and Microengineering, 2002, 12: 759-766.

Akgoz, B. and Civalek, O., A size-dependent shear deformation beam model based on the strain gradient elasticity theory, International Journal of Engineering Science, 2013, 70: 1-14.

Akgoz, B. and Civalek, O., Analysis of micro-sized beams for various boundary conditions based on the strain gradient elasticity theory, Achieve of Applied Mechanics, 2012, 82: 423-443.

Aladwani, A., Aldraihem, O. and Baz, A., Piezoelectric vibration energy harvesting from a two-dimensional coupled acoustic-structure system with a dynamic magnifier, Journal Vibration and Acoustics, 2015, 137: 031002.

Alavi, A. H., Hasni, H., Jiao, P., Borchani, W. and Lajnef, N., Fatigue cracking detection in steel bridge girders through a self-powered sensing concept. Journal of Construction and Steel Research, 2017, 128: 19-38.

Alavi, A. H., Hasni, H., Lajnef, N. and Chatti, K., Continuous health monitoring of pavement systems using smart sensing technology. Constructions and Building Materials, 2016, 114: 719-736.

Alavi, A.H., Hasni, H., Jiao, P., Borchani, W. and Lajnef, N., Fatigue cracking detection in steel bridge girders through a self-powered sensing concept, Journal Construction Steel Research, 2017, 128: 19-38.

Alavi, A.H., Hasni, H., Lajnef, N. and Chatti, K., An intelligent structural damage detection approach based on self-powered wireless sensor data, Automatic Constructions, 2015, 62: 24-44.

Alavi, A.H., Hasni, H., Lajnef, N. and Chatti, K., Continuous health monitoring of pavement systems using smart sensing technology, Constructions and Building Materials, 2016, 114: 719-736.

Al-Basyouni, K.S. and Tounsi, A., Mahmoud S.R., Size dependent bending and vibration analysis of functionally graded micro beams based on modified couple stress theory and neutral surface position, Composite Structures, 2015, 125: 621-630.

Alijani, F., Amabili, M., Balasubramanian, P., Carra, S., Ferrari, G. and Garziera, R., Damping for large-amplitude vibrations of plates and curved panels, part 1: Modeling and experiments. International Journal of Non-Linear Mechanics, 2016, 85: 23-40.

Amabili, M., Alijani, F. and Delannoy, J., Damping for large-amplitude vibrations of plates and curved panels, part 2: Identification and comparisons. International Journal of Non-Linear Mechanics, 2016, 85: 226-240.

Amirbayat, J. and Hearle, J.W.S., The complex buckling of flexible sheet materials – Part I theoretical approach, International Journal of Mechanical Sciences, 1986, 28(6): 339-358.

Anthoine, A., Effect of couple-stresses on the elastic bending of beams, International Journal Solids and Structures, 2000, 37: 1003–1018.

Asghari, M., Mahrobaiyan, M.H., Nikfar, M. and Ahmadian, M.T., A size-dependent nonlinear Timoshenko microbeam model based on the strain gradient theory, Acta Mechanica, 2012, 223: 1233-1249. DOI: 10.1115/1.4002787.

Aydogdu, M., A general nonlocal beam theory: Its application to nanobeam bending, buckling, and vibration, Physics E, 2009, 41: 1651-1655.

Banerjee, A., Bhattacharya, B. and Mallik, A.K., Large deflection of cantilever beams with geometric non-linearity: Analytical and numerical approaches, International Journal of Non-Linear Mechanics, 2008, 43: 366-376.

Bigoni, D., Nonlinear solid mechanics: Bifurcation theory and material instability, Cambridge University Press, 2012.

Blarigan, L.V., Moehlis, J. and McMeeking, R., Low dimensional modeling of a non-uniform buckled piezoelectric beam for vibrational energy harvesting, Smart Materials and Structures, 2015, 24: 065012.

Bodaghi, M. and Saidi, A.R., Levy-type solution for buckling analysis of thick functionally graded rectangular plates based on the higher-order shear deformation plate theory, Applied Mathematical Modelling, 2010, 34: 3659-3673.

Borchani, W., Energy harvesting from localized dynamic transitions in post-buckled elastic beams under quasi-static loading, 2014, PhD dissertation. Michigan State University.

Borchani, W., Lajnef, N. and Burgeuno, R., Energy method solution for the postbuckling response of an axially loaded bilaterally constrained beam, Mechanics Research Communications, 2015, 70: 114-119.

Borchani, W., Lajnef, N. and Burgueño, R., Model development for Dynamic Energy Conversion in post-buckled multi-stable slender columns, ASME Conference on Smart Materials, Adaptive Structures and Intelligent Systems, Newport, Rhode Island, September 2014.

Bosi, F., Misseroni, D., Corso, F.D. and Bigoni, D., Development of configurational forces during the injection of an elastic rod, Extreme Mechanics Letters, 2015, 4: 83-88.

Byklum, E. and Amdahl, J., A simplified method for elastic large deflection analysis of plates and stiffened panels due to local buckling, Thin-Walled Structures, 2002, 40: 925-953.

Camescasse, B., Fernandes, A. and Pouget, J., Bistable buckled beam: Elastica modeling and analysis of static actuation. International Journal Solids and Structures, 2013, 50: 2881-2893.

Chai, G.B., Large deflections of laminated composite plates, Composites Science and Technology, 1991, 42: 349-360.

Chai, H., The post-buckling response of a bi-laterally constrained column, Journal of Mechanical Physics and Solids, 1998, 46(7): 1155-1181.

Chang, T.Y. and Sawamiphakdi, K., Large deflection and post-buckling analysis of shell structures, Computer Methods in Applied Mechanics and Engineering, 1982, 32: 311-326.

Chen, A., Davalos, J.F., Jiao, P. and McGraw, B., Buckling behavior of sine web for composite wood I-joist with elastically restrained loaded edges under compression, Journal Engineering Mechanics, 2013,139(8): 1065-1072.

Chen, C., Tao, W., Liu, Z.J., Zhang, Y.W. and Song, J., Controlled buckling of thin film on elastomeric substrate in large deformation, Theoretical Applied Mechanics Letters, 2011, 2: 021001.

Chen, J.S., Pan, C., Wu, C.T. and Liu, W.K., Reproducing kernel particle methods for large deformation analysis of nonlinear structures, Computer Methods in Applied Mechanics and Engineering, 1996, 139: 195-227.

Cook-Chennault, K.A., Thambi, N. and Sastry, A.M., Powering MEMS portable devices—a review of non-regenerative and regenerative power supply systems with special emphasis on piezoelectric energy harvesting systems, Smart Materials and Structures, 2008, 17: 043001.

Croll, J.G.A., A simplified model of upheaval thermal buckling of subsea pipelines, Thin-Walled Structures, 1997, 29(1-4): 59-78.

Davidson, B.D., Delamination buckling: Theory and experiment, Journal of Composite Materials, 1991, 25: 1351-1378.

Dong, F., Li, H., Gong, X., Liu, Q. and Wang J., Energy-efficient transmissions for remote wireless sensor networks: an integrated HAP/satellite architecture for emergency scenarios. Sensors, 2015, 15: 22266-22290. DOI:10.3390/s150922266.

Doraiswamy, S., Narayanan, K.R. and Srinivasa, A.R., Finding minimum energy configurations for constrained beam buckling problems using the Viterbi algorithm, International Journal of Solids and Structures, 2012, 49: 289-297.

Dung, D.V. and Hoa, L.K., Research on nonlinear torsional buckling and post-buckling of eccentrically stiffened functionally graded thin circular cylindrical shells, Composites: Part B, 2013, 51: 300-309.

Elishakoff, I. and Candan, S., Apparently first closed-form solution for vibrating: Inhomogeneous beams, International of Journal Solids and Structures, 2001, 38: 3411-3441.

Eltaher, M.A., Khater, M.E. and Emam, S.A., A review on nonlocal elastic models for bending, buckling, vibrations, and wave propagation of nanoscale beams, Applied Mathematical Modelling, 2016, 40: 4109-4128.

Erigen,A.C. and Edelen,D.G.B., On nonlocal elasticity, International Journal of Engineering Sciences, 1972, 10: 233-248.

Eringen, A.C., On differential equations of nonlocal elasticity and solutions of screw dislocation and surface waves, Journal of Applied Physics, 1983, 54: 4703.

Erturk, A. and Inman, D.J., A distributed parameter electromechanical model for cantilever piezoelectric energy harvesters, Journal of Vibrations and Acoustics, 2008, 130(4): 041002.

Erturk, A., Vieira, W.G.R., Marqui, C.D. and Inman, D.J., On the energy harvesting potential of piezoaeroelastic systems, Applied Physics Letters, 2010, 96: 184103.

Farokhi, H. and Ghayesh, M.H., Thermo-mechanical dynamics of perfect and imperfect Timoshenko microbeams, International Journal of Engineering Science, 2015, 91: 12-33.

Fleck, N.A., Muller, G.M., Ashby, M.F. and Huchinson, J.W., Strain gradient plasticity: theory and experiment, Acta Metallurgica et Materialia, 1994, 42: 475-487.

Gao, X.L. and Park, S.K., Variational formulation of a simplified strain gradient elasticity theory and its application to a pressurized thick-walled cylinder problem, International Journal of Solids and Structures, 2007, 44: 7486-7499.

Gaudezi, P., Perugini, P. and Riccio, A., Post-buckling behavior of composite panels in the presence of unstable delaminations, Composite Structures, 2001, 51: 301-309.

Ghannadpour, S.A.M., Mohammadi, B. and Fazilati, J., Bending, buckling and vibration problems of nonlocal Euler beams using Ritz method, Composite Structures, 2013, 96: 584-589.

Giannakopoulos, A.E. and Stamoulis, K., Structural analysis of gradient elastic components, International Journal of Solids and Structures, 2007, 44: (3440-3451.

Giannakopoulos, A.E. and Stamoulis, K., Structural analysis of gradient elastic components, International Journal of Solids and Structures, 2007, 44: 3440-3451.

Green, P.L., Papatheou, E. and Sims, N.D., Energy harvesting from human motion and bridge vibrations: an evaluation of current nonlinear energy harvesting solutions, Journal of Intelligent Materials, Systems and Structures, 2013, 24:1494–505.

Guo, J., Lee, K. M., Zhu, D., Yi, X. and Wang, Y., Large-deformation analysis and experimental validation of a flexure-based mobile sensor node. IEEE/ASME Transaction on Mechanics, 2012, 17(4): 606-616.

Hajati, A. and Kim, S.G., Untra-wide bandwidth piezoelectric energy harvesting, Applied Physics Letters, 2011, 99: 083105.

Harne, R.L. and Wang, K.W., A review of the recent research on vibration energy harvesting via bistable systems, Smart Materials and Structures., 2013, 22: 023001.

Hasni, H., Alavi, A.H., Jiao, P. and Lajnef, N., Detection of fatigue cracking in steel bridge girders: A support vector machine approach, Archive of Civil and Mechanical Engineering, 2017, in press.

Hosseini-Hashemi, S., Fadaee, M. and Taher, H.R.D., Exact solutions for free flexural vibration of Levy-type rectangular thick plates via third-order shear deformation plate theory, Applied Mathematical Modelling, 2011, 35: 708-727.

Howell, L.L. and Midha, A., Parametric deflection approximations for end-loaded large deflection beams in compliant mechanisms, Journal of Mechanical Design, 1995, 117: 156-165.

Hu, N. and Burgueno, R., Buckling-induced smart applications: Recent advances and trends, Smart Materials and Structures, 2015, 24: 063001.

Huang, Y. and Li, X.F., A new approach for free vibration of axially functionally graded beams with non-uniform cross-section, Journal of Sound and Vibration, 2010, 329: 2291-2303.

Jiang, H., Khang, D.Y., Fei, H., Kim, H., Huang, Y., Xiao, J. and Rogers, J.A., Finite width effect of thin-films buckling on compliant substrate: Experimental and theoretical studies, Journal of Mechanical Physics and Solids, 2008, 56: 2585-2598.

Jiang, H., Sun, Y., Rogers, J.A. and Huang, Y., Post-buckling analysis for the precisely controlled buckling of thin film encapsulated by elastomeric substrates, International Journal of Solids and Structures, 2008, 45: 3858-3867.

Jiao, P., Analytical evaluations of buckling behavior of wood composite I-joist with sinusoidal web, Master of Science, West Virginia University, 2012.

Jiao, P., Borchani, W., Alavi, A.H., Hasni, H. and Lajnef, N., An energy harvesting and damage sensing solution based on post-buckling response of non-uniform cross-section beams, Structural Control and Health Monitoring, 2017, in press.

Jiao, P., Borchani, W., Hasni, H., Alavi, A.H. and Lajnef, N., Post-buckling response of non-uniform cross-section bilaterally constrained beams, Mechanics Research Communications, 2016, 78: 42-50.

Jiao, P., McGraw, B., Chen, A., Davalos, J.F. and Ray, I., Flexural-torsional buckling of cantilever composite wood I-beams with sinusoidal web geometry, Earth and Space, 2012: 684-693 doi: 10.1061/9780784412190.074.

Kahrobaiyan, M.H., Asghari, M., Hoore, M. and Ahmadian, M.T., Nonlinear size-dependent forced vibrational behavior of microbeams based on a non-classical continuum theory, Journal of Vibration Control, 2011, 18(5): 696-711.

Karampour, H., Albermani, F. and Veidt, M., Buckle interaction in deep subsea pipelines, Thin-Walled Structures, 2013, 72: 113-120.

Katz, S. and Givli, S., The post-buckling behavior of a beam constrained by springy walls, Journal of Mechanical Physics and Solids, 2015, 78: 443-466.

Kim, I., Jung, H., Lee, B.M. and Jang, S., Broadband energy-harvesting using a two degree-of-freedom vibration body, Applied Physics Letters, 2011 98: 214102.

Kong, S., Zhou, S., Nie, Z. and Wang, K., Static and dynamic analysis of micro beams based on strain gradient elasticity theory, International Journal of Engineering Science, 2009, 47: 487-498.

Lajnef, N., Burgueño, R., Borchani, W. and Sun, Y., A concept for energy harvesting from quasi-static structural deformations through axially loaded bilaterally constrained columns with multiple bifurcation points. Smart Material and Structure, 2014, 23(5): 055005.

Lajnef, N., Borchani, W., Burgueño, R. and Chakrabartty, S., Self-powered Piezo-Floating-Gate smart-gauges based on quasi-static mechanical energy concentrators and triggers, IEEE Sensors Journal, 2015, 15(2): 676-683.

Lajnef, N., Burgueno, R., Borchani, W. and Sun, Y., A concept for energy harvesting from quasi-static structural deformations through axially loaded bilaterally constrained columns with multiple bifurcation points, Smart Materials and Structures, 2014, 23(5): 055005.

Lajnef, N., Burgueño, R., Borchani, W., Sun, Y. and Heeringa, A., Characterization of mechanically-equivalent amplifiers and frequency modulating concepts for energy harvesting devices, ASME Conference Smart Mater, Adaptive Structures and Intelligent Systems, Stone Mountain, GA, September 2012.

Lam, D.C.C., Yang, F., Chong, A.C.M., Wang, J. and Tong, P., Experiments and theory in strain gradient elasticity, Journal of the Mechanics and Physics of Solids, 2003, 51: 1477-1508.

Lee, K., Large deflections of cantilever beams of non-linear elastic material under a combined loading, International Journal of Non-Linear Mechanics, 2002, 37: 439-443.

Lei, Z.X., Liew, K.M. and Yu, J.L., Buckling analysis of functionally graded carbon nanotube-reinforced composite plates using the element-free kp-Ritz method, Composite Structures, 2013, 98: 160-168.

Li, Q.S., Buckling of multi-step non-uniform beams with elastically restrained boundary conditions, Journal of Construction Steel Research, 2001, 57: 753-777.

Li, Q.S., Cao, H. and Li, G., Stability analysis of bars with multi-segments of varying cross-section, Computers and Structures, 1994, 53(5): 1085-1089.

Li, S.R., Zhang, J.H. and Zhao, Y.G., Nonlinear thermomechanical post-buckling of circular FGM plate with geometric imperfection, Thin-Walled Structures, 2007, 45: 528-536.

Librescu, L., Khdeir, A.A. and Frederick, D., A shear deformable theory of laminated composite shallow shell-type panels and their response analysis I: free vibration and buckling, Acta Mechanica, 1989, 76: 1-33.

Liu, C.W. and Chen, J.S., Effect of coulomb friction on the deformation of an elastic constrained in a straight channel with clearance, European Journal of Mechanics A/Solids, 2013, 39: 50-59.

Liu, J., Fang, H., Xu, Z., Mao, X., Shen, X., Chen, D., Liao, H. and Cai, B., A MEMS-based piezoelectric power generator array for vibration energy harvesting, Microelectronics Journal, 2008, 39: 802-806.

Liu, S. and Burgueno, R., Controlled elastic postbuckling of bilaterally constrained non-prismatic columns: Application to enhanced quasi-static energy harvesters, Smart Materials and Structures, 2016, 25: 125010.

Lynch, J.P. and Loh, K.J., A summary review of wireless sensors and sensor networks for structural health monitoring, The Shock and Vibration Digest, 2008, 38(2): 91-128.

Ma, L.S. and Wang, T.J., Nonlinear bending and post-buckling of functionally graded circular plate under mechanical and thermal loadings, International Journal of Solids and Structures, 2003, 40: 3311-3330.

Ma, L.S. and Wang, T.J., Relationships between axisymmetric bending and buckling solutions of FGM circular plates based on third-order plate theory and classical plate theory, International Journal of Solids and Structures, 2004, 41: 85-101.

Malekzadeh, P. and Shojaee, M., Surface and nonlocal effects on the nonlinear free vibration of non-uniform nanobeams, Composites: Part B, 2013, 52: 84-92.

Marinkovic, B. and Koser, H., Smart sand—a wide bandwidth vibration energy harvesting platform, Applied Physics Letters, 2009, 94: 103505.

Matsunaga, H., Thermal buckling of functionally graded plates according to a 2D higher-order deformation theory, Composite Structures, 2009, 90: 76-86.

Mehner, J.E., Gabbay, L.D. and Senturia, S.D., Computer-aided generation of nonlinear reduced-order dynamic macromodels—II. Non-stress-stiffness case, Journal of Microelectromechanical Systems, 2000, 9: 270-278.

Meiche, N.E., Tounsi, A., Ziane, N., Mechab, I. and Bedia, E.A.A., A new hyperbolic shear deformation theory for buckling and vibration of functionally graded sandwich plate, International Journal of Mechanical Sciences, 2011, 53: 237-247.

Milazzo, A. and Oliveri, V., Post-buckling analysis of cracked multilayered composite plates by pb-2 Rayleigh-Ritz method. Composite Structures, 2015, 132: 75-86.

Murmu, T. and Pradhan, S.C., Buckling analysis of a single-walled carbon nanotube embedded in an elastic medium based on nonlocal elasticity and Timoshenko beam theory and using DQM, Physics E, 2009, 41: 1232-1239.

Murmu, T. and Pradhan, S.C., Buckling of bi-axially compressed orthotropic plates at small scale, Mechanics Research Communications, 2009, 36: 933-938.

Naderi, A. and Saidi, A.R., On pre-buckling configuration of functionally graded Mindlin rectangular plates, Mechanics Research Communications, 2010, 37: 535-538.

Najafi, k., Galchev, T., Aktakka, E.E., Person, R.L. and McCullagh, J., Microsystems for energy harvesting, IEEE Transducers, 2011, Beijing, China.

Najafizadeh, M.M. and Eslami, M.R., Buckling analysis of circular plates of functionally graded materials under uniform radial compression, International Journal of Mechanical Sciences, 2002, 44: 2479-2493.

Najafizadeh, M.M. and Heydari, H.R., An exact solution for buckling of functionally graded circular plates based on higher order shear deformation plate theory under uniform radial compression, International Journal of Mechanical Sciences, 2008, 50: 603-612.

Najafizadeh, M.M. and Heydari, H.R., Thermal buckling of functionally graded circular plates based on higher order shear deformation plate theory, European Journal of Mechanics A/Solids, 2004, 23: 1085-1100.

Nayfeh, A.H. and Emam, S.A., Exact solution and stability of postbuckling configurations of beams, Nonlinear Dynamics, 2008, 54: 395-408.

Neves, A.M.A., Ferreira, A.J.M., Carrera, E., Cinefra, M., Roque, C.M.C., Jorge, R.M.N. and Soares, C.M.M., Static, free vibration and buckling analysis of isotropic and sandwich functionally graded plates using a quasi-3D higher-order shear deformation theory and a meshless technique, Composites: Part B, 2013, 44: 657-674.

Nilsson, K.F., Asp, L.E., Alpman, J.E. and Nystedt, L., Delamination buckling and growth for delamination at different depths in a slender composite panel, International Journal of Solids and Structures, 2001, 38: 3039-3071.

Nilsson, K.F., Thesken, J.C., Sindelar, P., Giannakopoulos, A.E. and Storakers, B., A theoretical and experimental investigation of buckling induced delamination growth, Journal of Mechanical Physics and Solids, 1993, 41(4): 749-782.

Ovesy, H. R., Mooneghi, M. A., and Kharazi, M., Post-buckling analysis of delaminated composite laminates with multiple through-the-width delaminations using a novel layerwise theory. Thin-Walled Structures, 2015, 94: 98-106.

Papargyri-Beskou, S., Tsepoura, K.G., Polyzos, D. and Beskos, D.E., Bending and stability analysis of gradient elastic beams, International Journal of Solids and Structures, 2003, 40: 385–400.

Park, G., Rosing, T., Todd, M.D., Farrar, C.R. and Hodgkiss, W., Energy harvesting for structural health monitoring sensor networks, Journal Infrastructures and Systems, 2008, 14(1): 64-79.

Park, S.K. and Gao, X.L., Bernoulli-Euler beam model based on a modified couple stress theory, Journal of Micromechanics and Microengineering, 2006, 16: 2355-2359.

Peddieson, J., Buchanan, G.R. and McNitt, R.P., Application of nonlocal continuum models to nanotechnology, International Journal of Engineering Sciences, 2003, 41: 305-312.

Pircher, M. and Bridge, Q., Buckling of thin-walled silos and tanks under axial load—some new aspects, Journal Structural Engineering, 2001, 1127(10): 1129-1136.

Pradhan, S.C. and Murmu, T., Small scale effect on the buckling analysis of single-layered graphene sheet embedded in an elastic medium based on nonlocal plate theory, Physics E, 2010, 42: 1293-1301.

Pradhan,S.C. and Murmu,T., Small scale effect on the buckling of single-layered graphene sheets under biaxial compression via nonlocal continuum mechanics, Computational Materials Science, 2009, 47: 268-274.

Quinn, D.D., Triplett, A.L., Vakakis, A.F. and Bergman, L.A., Energy harvesting from impulsive loads using intentional essential nonlinearities, Journal Vibration and Acoustics, 2011, 133: 011004.

Rafiee, M., He, X.Q., Mareishi, S. and Liew, K.M., Nonlinear response of piezoelectric nanocomposite plates: large deflection, post-buckling and large amplitude vibration, International Journal of Applied Mechanics, 2015, 7(5). 10.1142/S175882511550074X.

Ram, Y.M., Matrix iteration method for nonlinear eigenvalue problems with applications, Mechanical Systems and Signal Proceeding, 2016, 81: 1-18.

Reddy, J.N., Nonlocal theories for bending, buckling and vibration of beams, International Journal of Engineering Sciences, 2007, 45: 288-307.

Ro, W.C., Chen, J.S. and Hong, S.Y., Vibration and stability of a constrained elastica with variable length. International Journal of Solids and Structures, 2010, 47: 2143-2154.

Safa, Y. and Hocker, T., A validated energy approach for the post-buckling design of micro-fabricated thin film devices, Applied Mathematical Modelling, 2015, 39: 483-499.

Sahhaee-Pour, A., Elastic buckling of single-layered graphene sheet, Computational Materials Science, 2009, 45: 266-270.

Saidi, A.R. and Baferani, A.H., Thermal buckling analysis of moderately thick functionally graded annular sector plates, Composite Structures, 2010, 92: 1744-1752.

Salehi, H. and Burgurno, R., Structural health monitoring from discrete binary data through pattern recognition, 6th International Conference Structures and Engineering Mechanics Computation, 2016.

Salehi, H., Das, S., Chakrabartty, S., Biswas, S. and Burgurno, R., Structural assessment and damage identification algorithms using binary data, ASME 2015 Conference on Smart Materials, Adaptive Structures and Intelligent Systems, 2015.

Santos, H.A.F.A. and Gao, D.Y., Canonical dual finite element method for solving post-buckling problems of a large deformation elastic beam, International Journal of Non-Linear Mechanics, 2012, 47: 240-247.

Sciuva, M.D., Bending, vibration and buckling of simply supported thick multilayered orthotropic plates: an evaluation of a new displacement model, Journal of Sound and Vibration, 1986, 105(3): 425-442.

Shariat, B.A.S. and Eslami, M.R., Bucking of thick functionally graded plates under mechanical and thermal loads, Composite Structures, 2007, 78: 433-439.

Shariat, B.A.S., Javaheri, R. and Eslami, M.R., Buckling of imperfect functionally graded plates under in-plane compressive loading, Thin-Walled Structures, 2005, 43: 1020-1036.

Shen, H.S., Large deflection of composite laminated plates under transverse and in-plane loads and resting on elastic foundations, Composite Structures, 1999, 45: 115-123.

Shi, R., Wang, L., Guo, Z. and Yuan, F., Upheaval buckling of a pipeline with prop imperfection on a plastic soft seabed, Thin-Walled Structures, 2013, 65: 1-6.

Shvartsman, B.S., Large deflections of a cantilever beam subjected to a follower force, Journal of Sound and Vibration, 2007, 304: 969-973.

Simsek, M. and Yurtcu, H.H., Analytical solutions for bending and buckling of functionally graded nanobeams based on the nonlocal Timoshenko beam theory, Composite Structures, 2013, 97: 378-386.

Sofiyev, A. H. and Kuruoglu, N., Buckling analysis of nonhomogeneous orthotropic thin-walled truncated conical shells in large deformation. Thin-Walled Structures, 2013, 62: 131-141.

Sofiyev, A.H., On the dynamic buckling of truncated conical shells with functionally graded coatings subject to a time dependent axial load in the large deformation, Compos B: Engineering, 2014, 58: 524-533.

Solano-Carrillo, E., Semi-exact solutions for large deflections of cantilever beams of non-linear elastic behavior, International Journal Non-Linear Mechanics, 2009, 44: 253-256.

Soliman, M.S.M., Abdel-Rahman, E.M., El-Saadany, E.F. and Mansour, R.R., A wideband vibration-based energy harvester. Journal of Micromechanics and Microengineering, 2008, 18: 115021.

Song, J., Jiang, H., Liu, Z.J., Khang, D.Y., Huang, Y., Rogers, J.A., Lu, C. and Koh, C.G., Buckling of a stiff thin film on a compliant substrate in large deformation, International Journal of Solids and Structures, 2008, 45: 3107-3121.

Soong, T.C. and Choi, I., An elastica that involves continuous and multiple discrete contact with a boundary, International Journal of Mechanical Sciences, 1986, 28(1): 1-10.

Srivastava, A. and Hui, C.Y. Large deformation contact mechanics of long rectangular membranes. I. Adhesionless contact. Proceedings of the Royal Society. 2013. http://dx.doi.org/10.1098/rspa.2013.0424.

Srivastava, A. and Hui, C.Y. Large deformation contact mechanics of long rectangular membranes. II. Adhesive contact. Proceedings of the Royal Society. 2013. http://dx.doi.org/10.1098/rspa.2013.0425.

Srivastava, A. and Hui, C.Y., Large deformation contact mechanics of long rectangular membranes I: Adhesionless contact, Proceedings of Royal Society A, 2013, 469: 20130424.

Srivastava, A. and Hui, C.Y., Large deformation contact mechanics of long rectangular membranes II: Adhesion contact, Proceedings of Royal Society A, 2013, 469: 20130425.

Tang, L., Yang, Y. and Soh, C.K., Toward broadband vibration-based energy harvesting, Journal of Intelligent Materials, systems and Structures, 2010, 21: 1867-1897.

Taylor, N. and Tran, V., Experimental and theoretical studies in subsea pipeline buckling, Marine Structures, 1996, 9: 211-257.

Thai, H.T. and Kim, S.E., Levy-type solution for buckling analysis of orthotropic plates based on two variable refined plate theory, Composite Structures, 2011, 93: 1738-1746.

Thai, H.T. and Vo, T.P., A new sinusoidal shear deformation theory for bending, buckling, and vibration of functionally graded plates, Applied Mathematical Modelling, 2013, 37: 3269-3281.

Thai, H.T., A nonlocal beam theory for bending, buckling and vibration of nanobeams, International Journal of Engineering Science, 2012, 52: 56-64.

Thai, H.T., Vo, T.P., A nonlocal sinusoidal shear deformation beam theory with application to bending, buckling, and vibration of nanobeams, International Journal of Engineering Science, 2012, 54: 58-66.

Thai, H.T., Vo, T.P., Nguyen, T.K. and Lee, J., Size-dependent behavior of functionally graded sandwich microbeams based on the modified couple stress theory, Composite Structures, 2015, 123: 337-349.

Wang, C.M., Zhang, Y.Y., Ramesh, S.S. and Kitipornchai, S., Buckling analysis of micro and nano-rods/tubes based on nonlocal Timoshenko beam theory, Journal of Physics D: Applied Physics, 2006, 39: 3904-3909.

Wang, J., Chen, J.K. and Liao, S., An explicit solution of the large deformation of a cantilever beam under point load at the free tip, Journal of Computational Applied Mathematics, 2008, 212: 320-330.

Wang, L., Dynamical behaviors of double-walled carbon nanotubes conveying fluid accounting for the role of small length scale, Computational Materials Science, 2009, 45: 584-588.

Wang, L., Sui, R., Yuan, F., Guo, Z. and Yu, L., Global buckling of pipelines in the vertical plane with a soft seabed, Applied Ocean Research, 2011, 33: 130-136.

Wang, L., Wave propagation of fluid-conveying single-walled carbon nanotubes via gradient elasticity theory, Computational Materials Science, 2010, 49: 761-766.

Wang, Q., Wave propagation in carbon nanotubes via nonlocal continuum mechanics, Journal of Applied Physics, 2005, 98: 124301.

Wu, T.L., Shuka, K.K. and Huang, J.H., Post-buckling analysis of functionally graded rectangular plates, Composite Structures, 2007, 81: 1-10.

Xia, W., Wang, L. and Yin, L., Nonlinear non-classical microscale beams: Static bending, postbuckling and free vibration, International Journal Engineering Sciences, 2010, 48: 2044-2053.

Xu, Q., Lv, Y., Dong, C., Sreeprased, T.S., Tian, A., Zhang, H., Tang, Y., Yu, Z. and Li, N., Three-dimensional micro/nanoscale architectures: fabrication and applications, Nanoscale, 2015, 7: 10883-10895.

Xu, Q., Yao, Y., Ma, Z. and Xia, Z., Measurement of interfacial energy and friction between carbon nanotubes and polymer matrix by a micro-pullout test, Science of Advanced Materials, 2012, 4(8): 888-892.

Yang, F., Chong, A.C.M., Lam, D.C.C. and Tong, P., Couple stress based strain gradient theory for elasticity. International Journal of Solids and Structures, 2002, 39: 2731-2743.

Yang, S., Liu, Y., Wang, X., Gunasekaran, D., Karki, U. and Peng, F.Z., Modulation and control of transformerless UPFC, IEEE Transaction on Power Electrics, 2016, 31(2): 1050-1063.

Zenkour, A.M., A comprehensive analysis of functionally graded sandwich plate II buckling and free vibration, International Journal of Solids and Structures, 2005, 42: 5243-5258.

Zhang, L., Wang, J. and Zhou, Y.H. Large deflection and post-buckling analysis of non-linearly elastic rods by wavelet method. International Journal Non-Linear Mechanics, 2016, 78: 45-52.

Zhao, X., Lee, Y.Y. and Liew, K.M., Mechanical and thermal buckling analysis of functionally graded plates, Composite Structures, 2009, 90: 161-171.

Zhao, Y., Zhang, J., Jiao, P. and Sun, G., Analytical equations on polynomial curved beam, Journal of Shenyang Jianzhu University (Natural Science), 2008, 2: 5-15.